Sea Ice Remote Sensing Using Spaceborne Global Navigation Satellite System Reflectometry

by

© Qingyun Yan, B.Eng., M.Eng.

A thesis submitted to the

School of Graduate Studies

in partial fulfilment of the

requirements for the degree of

Doctor of Philosophy

Department of Electrical and Computer Engineering

Faculty of Engineering and Applied Science

Memorial University of Newfoundland

December, 2019

St. John's Newfoundland

Abstract

In this research, the application of spaceborne Global Navigation Satellite System-Reflectometry (GNSS-R) delay-Doppler maps (DDMs) for sea ice remote sensing is investigated.

Firstly, a scheme is presented for detecting sea ice from TechDemoSat-1 (TDS-1) DDMs. Less spreading along delay and Doppler axes is observed in the DDMs of sea ice relative to those of seawater. This enables us to distinguish sea ice from seawater through studying the values of various DDM observables, which describe the extent of DDM spreading.

Secondly, three machine learning-based methods, specifically neural networks (NNs), convolutional neural networks (CNNs) and support vector machine (SVM), are developed for detecting sea ice and retrieving sea ice concentration (SIC) from TDS-1 data. For these three methods, the architectures with different outputs (i.e. category labels and SIC values) are separately devised for sea ice detection (classification problem) and SIC retrieval (regression problem) purposes. In the training phase, different designs of input that include the cropped DDM (40-by-20), the full-size DDM (128-by-20), and the feature selection (FS) (1-by-20) are tested. The SIC data obtained by Nimbus-7 SMMR and DMSP SSM/I-SSMIS sensors are used as the target data, which are also regarded as ground-truth data in this work. In the experimental stage, CNN output resulted from inputting full-size DDM data shows better accuracy than that of the NN-based method. Besides, performance of both CNNs and NNs is enhanced with the cropped DDMs. It is found that when DDM data are adequately preprocessed CNNs and NNs share similar accuracy. Further comparison is made be-

tween NN and SVM with FS. The SVM algorithm demonstrates improved accuracy compared with the NN method. In addition, the designed FS is proven to be effective for both SVM- and NN-based approaches.

Lastly, a reflectivity (Γ)-based method for sea ice thickness (SIT) retrieval is proposed. SIT is calculated from TDS-1 Γ data, and verified with two sets of reference SIT data; one is from University of Hamburg and obtained by the Soil Moisture Ocean Salinity (SMOS) satellite, and the other is the combined SMOS/Soil Moisture Active Passive (SMAP) measurements from University of Bremen. This analysis is performed on the data with sea ice thickness less than 1 m. Through comparison, a good consistency between the derived TDS-1 SIT and the reference SIT was obtained, with a correlation coefficient (r) of 0.84 and a root-mean-square difference (RMSD) of 9.39 cm with SMOS, and an r of 0.67 and an RMSD of 9.49 cm with SMOS/SMAP, which demonstrates the applicability of the developed model and the utility of TDS-1 data for SIT estimation. In addition, this method is shown to be useful for improving proposed sea ice detection methods.

Acknowledgements

I wish to thank the Faculty of Engineering and Applied Science for offering me the opportunity of conducting this work. Particularly, the supervision of Dr. Weimin Huang and his help through this are greatly appreciated. In addition, I would like to show my gratitudes to my supervisory committee members, Dr. Cecilia Moloney and Dr. Octavia A. Dobre, for giving me many valuable suggestions and comments on my research.

I am grateful for financial support in the form of the Natural Sciences and Engineering Research Council of Canada Discovery Grants (NSERC RGPIN-2017-04508 and RGPAS-2017-507962), and the Canadian Space Agency CubeSat Grant (17CCP-NFL11) to Dr. Huang. In addition, this research was undertaken thanks in part to funding from the Canada First Research Excellence Fund, through the Ocean Frontier Institute.

I would like to thank all my friends in St. John's for their help during daily life and members of radar remote sensing group for their advice in improving my research.

Finally, I deeply appreciate the patience and understanding of my parents, Mrs. Suqiong Jiang and Mr. Jianchun Yan. This work could not be completed without their support.

Contents

List of Tables

List of Figures

Table of Acronyms

The page numbers here indicate the place of first significant reference.

GNSS-R:	Global Navigation Satellite System-Reflectometry (p. 1)
SAR:	Synthetic aperture radar (p. 2)
Tx:	Transmitter (p. 2)
Rx:	Receiver (p. 2)
GPS:	Global Positioning System (p. 2)
CYGNSS:	Cyclone Global Navigation Satellite System (p. 3)
DDM:	Delay-Doppler map (p. 3)
SP:	Specular point (p. 3)
UK-DMC:	UK Disaster Monitoring Constellation (p. 4)
SIC:	Sea ice concentration (p. 6)
TDS-1:	TechDemoSat-1 (p. 7)
TSVD:	Truncated singular value decomposition (p. 7)
SIA:	Spatial integration approach (p. 7)
FYI:	First-year ice (p. 7)
MYI:	Multi-year ice (p. 7)

CART: Classification and regression tree (p. 8)

ZV: Zavorotny-Voronovich (p. 11)

C/A: Coarse/acquisition (p. 11)

RHCP: Right-handed circular polarization (p. 11)

LHCP: Left-handed circular polarization (p. 11)

SNR: Signal-to-noise ratio (p. 11)

SIT: Sea ice thickness (p. 12)

NN: Neural network (p. 13)

CNN: Convolutional neural network (p. 13)

SVM: Support vector machine (p. 13)

CM: Center-of-mass (p. 19)

GC: Geometrical center (p. 19)

MLP: Multilayer perceptron (p. 31)

LM: Levenberg-Marquardt (p. 33)

ReLU: Rectified linear unit (p. 39)

SGDM: Stochastic gradient descendant with momentum (p. 40)

SVR: Support vector regression (p. 43)

FS: Feature selection (p. 44)

RBF: radial basis function (p. 47)

SMMR: Scanning Multichannel Microwave Radiometer (p. 53)

SMM/Is: Special Sensor Microwave/Imagers (p. 53)

DMSP: Defense Meteorological Satellite Program (p. 53)

SSMIS: Special Sensor Microwave Imager/Sounder (p. 53)

PDF: Probability density functions (p. 56)

WAF: Woodward Ambiguity Function (p. 56)

SWH: Significant wave height (p. 69)

WS: Wind speed (p. 69)

NDBC: National Data Buoy Center (p. 69)

RMSD: Root-mean-square difference (p. 80)

ERS: European Remote Sensing (p. 80)

SMOS: Soil Moisture Ocean Salinity (p. 82)

SMAP: Soil Moisture Active Passive (p. 82)

Table of Symbols

The page numbers here indicate the place of first significant reference. Although not all symbols are explicitly referenced below, their definitions are obvious from the context.

σ^0 : Scattering coefficient (p. 7)

δSNR : The high-frequency part of the SNR data (p. 11).

C_1 : The amplitude term 1 (p. 11).

C_2 : The amplitude term 2 (p. 11).

λ : The signal wavelength (p. 11).

h : The height of receiver above the reflecting surface (p. 11).

θ : The incidence angle (p. 11).

ζ : The damping parameter (p. 11).

ρ : The ratio between direct and reflected signals (p. 12).

$\overline{DDM}$: The normalized DDM (p. 18).

DDM_{thres} : The DDM threshold (p. 18).

τ : Delay shift (p. 18).

f : Doppler shift (p. 18).

τ_δ : The resolutions of delay shift (p. 18).

f_δ : The resolutions of Doppler shift (p. 18).

I_0 : Power Summation (p. 18).

CM_τ : The coordinate of CM in the delay axis (p. 19).

CM_f : The coordinate of CM in the Doppler axis (p. 19).

MAX_τ : The coordinate of peak power point in the delay axis (p. 19).

MAX_f : The coordinate of peak power point in the Doppler axis (p. 19).

GC_τ : The coordinate of GC in the delay axis (p. 19).

GC_f : The coordinate of GC in the Doppler axis (p. 19).

τ_1 : The lower pixel limit of noise box in the signal-free DDM area in the delay axis (p. 20).

τ_2 : The upper pixel limit of noise box in the signal-free DDM area in the delay axis (p. 20).

f_1 : The lower pixel limit of noise box in the signal-free DDM area in the Doppler axis (p. 20).

f_2 : The upper pixel limit of noise box in the signal-free DDM area in the Doppler axis (p. 20).

N : The number of pixels within the noise box (p. 20).

L : The adaptive incoherent summation length (p. 23).

M : The layer index (p. 31).

S_M : The number of units in layer M (p. 31).

$n_j^{(k+1)}$: The net input to neuron j in layer $k+1$ (p. 32).

$a_j^{(k+1)}$: The output corresponding to $n_j^{(k+1)}$ (p. 32).

$w_{ji}^{(k+1)}$: The synaptic weights connecting neuron j in layer $k+1$ and neuron i in layer k (p. 32).

$\varphi^{(k+1)}(\cdot)$: The activation function for neuron j in layer $k+1$ (p. 32).

$b_j^{(k+1)}$: The bias for neuron j in layer $k+1$ (p. 32).

$\mathbf{p}$: The input DDM pixels vector (p. 32).

$\mathbf{a}$: The input vector (p. 32).

$\mathbf{W}$: The weight matrix (p. 32).

$\mathbf{b}$: The bias vector (p. 32).

ε : The sum of squared error (p. 33).

$\mathbf{e}$: The error vector (p. 33).

$\mathbf{t}$: The desired output (p. 33).

Q : The number of input patterns (p. 33).

$\mathbf{m}$: The weight vector (p. 33).

$\mathbf{J}$: The Jacobian matrix (p. 33).

$\mathbf{I}$: The identity matrix (p. 33).

μ : The combination coefficient (p. 33).

β : The multiplication factor (p. 34).

$\mathbf{h}_{ij}^{k}$: The convolved image resulted from the kth ($k = 1, ..., 5$) filter $\mathbf{W^k}$ (p. 39).

$\mathbf{X}$: The input image (p. 39).

p_r : The probability of occurrence of sea ice or seawater (p. 40).

a_1 : The unit 1 in the output layer (p. 40).

a_2 : The unit 2 in the output layer (p. 40).

F : The forward propagation (p. 40).

$\mathbf{y}$: The output matrix (p. 41).

$\mathbf{V}$: The momentum variable (p. 41).

m : The momentum (p. 41).

η : The learning rate (p. 41).

$\mathbf{w}$: The weights of mapping function (p. 47).

C : The penalty parameter (p. 47).

ξ_j : The slack variable (p. 47).

$\boldsymbol{\alpha}$: The Lagrange multipliers (p. 47).

K : The kernel function (p. 47).

ξ_j^* : The slack variable for SVR (p. 48).

$\boldsymbol{\alpha}^*$: The Lagrange multipliers for SVR (p. 48).

ϵ : The allowance for errors (p. 48).

γ : The kernel width (p. 49).

r : Correlation coefficient (p. 61).

SIC_{nn} : The NN-based SIC results (p. 64).

SIC_{ref} : The reference SIC data (p. 64).

E_{av} : The mean error (p. 64).

E_{abs} : The mean absolute error (p. 64).

E_{std} : The standard deviation error (p. 64).

Γ : The surface reflectivity (p. 82).

P_t : The transmitted power (p. 86).

P_r : The received power (p. 86).

G_t : The antenna gain of Tx (p. 86).

G_r : The antenna gain of Rx (p. 86).

R_t : The distance from Tx to SP (p. 86).

R_r : The distance from Rx to SP (p. 86).

R_d : The distance from Tx to Rx (p. 86).

P_d : The direct power (p. 86).

G_d : The zenith antenna gain (p. 86).

σ_{rms} : The surface RMS height (p. 87).

R : The Fresnel reflection coefficient (p. 87).

R_1 : The reflection coefficients at the upper interface (p. 87).

R_2 : The reflection coefficients at the lower interface (p. 87).

d : Sea ice thickness (p. 87).

k_{zi} : The z-component of the signal propagation vector in the sea ice (p. 87).

β : The phase constant (p. 87).

α : The attenuation coefficient (p. 87).

ε_i : The relative permittivity of sea ice (p. 88).

V_b : The relative brine volume (p. 89).

S : Sea ice salinity (p. 89).

T : Sea ice temperature (p. 89).

R_{hh} : The horizontally polarized reflection coefficient (p. 89).

R_{vv} : The vertically polarized reflection coefficient (p. 89).

ε_w : The relative permittivity of seawater (p. 89).

θ_i : The incidence angle in the sea ice (p. 89).

ε_r : The ratio between ε_w and ε_i (p. 89).

Chapter 1

Introduction

In this chapter, the significance of sea ice remote sensing using Global Navigation Satellite System Reflectometry (GNSS-R) signals is demonstrated first. Then, the literature relevant to GNSS-R sea ice sensing applications is summarized. Lastly, the scope of this thesis is outlined.

1.1 Research Rationale

A strong decline of Arctic sea ice has been reported during the last decades [1]–[3], and this phenomenon is coincident with global warming [4]. Sea ice plays an important role in maintaining the high surface albedo, limiting air-sea interaction [5], and modulating the distribution of freshwater and seawater [6]. Furthermore, sea ice conditions have direct impacts on managing and securing human activities, such as offshore oil and gas development and global shipping industries [7]. Due to its significant influence on the global climate and human activities, a good knowledge of sea ice information is critical. However, *in situ* sea ice measurement is cumbersome

and limited in spatial coverage. Instead, remote sensing techniques present a more efficient and cost effective alternative for acquiring sea ice data.

Large-scale sea ice remote sensing data from satellites have been used intensively [8]. Sea ice conditions, such as extent, drift, growth stage, concentration and thickness can be estimated from passive microwave sensors [9], [10], scatterometer [11], radar altimeter [3], [12], and synthetic aperture radar (SAR) [13], [14] data. However, passive microwave and scatterometer data are generally characterized by coarse resolutions (typically 25-50 km). On the other hand, SAR and radar altimeter are able to provide finer resolutions, but their demands in instruments (high power requirement and complex circuit designs) as well as the expenses of deployment result in high cost. In addition, interpretations of SAR images are typically time-consuming and subjective [15] and the use of empirical retracking has no physical model for altimeters [16].

Since Hall and Cordey proposed the concept of GNSS-R in [17], it has been successfully applied to various remote sensing tasks, e.g., sea surface wind and roughness monitoring [18]–[25], sea surface height observation [26]–[29], snow depth estimation [30]–[35] as well as soil moisture and vegetation sensing [36]–[40]. GNSS-R works in a bistatic configuration, in which the transmitter (Tx) and the receiver (Rx) are at different locations. Compared with monostatic radars, the bistatic technique has its advantages in terms of increased resilience to electronic countermeasures and enhanced radar cross section of the target. Theoretically, the Tx can be any GNSS satellites such as the Global Positioning System (GPS), GLONASS, Galileo, and Beidou/COMPASS [41]–[43]. After the transmitted signals have been reflected by the Earth's surface, e.g., ocean, land, and ice (thus carrying information about the surface conditions), they will be captured by one or more GNSS-R Rxs. In addition, a

GNSS-R Rx is capable of collecting data from several different tracks simultaneously. Furthermore, as a passive instrument, a GNSS-R Rx is typically low-cost, low-mass, and low-power, which allows easy and flexible deployment. According to the platform of Rxs, GNSS-R can be divided into three categories, i.e., spaceborne, airborne, and ground-based. The first type mainly aims at large-scale or global monitoring while the latter two are usually for regional and local observations [44]. Therefore, with multiple GNSS-R Rxs deployed on various platforms, a temporally and spatially intensive coverage at both global- and regional-scales can be achieved. Examples using different platforms can be found in e.g., [45]–[49] for spaceborne, [21], [28], [38], [50] for airborne, and [31], [51]–[54] for ground-based applications, respectively. A schematic of spaceborne GNSS-R is shown in Fig. 1.1. For compactness, the transmitter is not shown here. At present, the mostly used signals are from GPS Txs, which are of L-band wavelength (19 cm). In terms of temporal and spatial resolutions, taking the Cyclone GNSS (CYGNSS) system as an illustration, the achieved average revisit time is 4 hours [55] and the spatial resolution can be about 10 km for cases of incoherent scattering and about 500 m for coherent cases [56]. The spatial resolution of spaceborne GNSS-R is comparable to or better than that of radar altimeters (with a nominal circular footprint of 2–10 km in diameter for Envisat or an along-track footprint of 1.65 km $\times$ 0.30 km for CryoSat-2 [57]).

In the GNSS-R research area, the delay-Doppler map (DDM) is a well-known tool, from which information about the observed surface (e.g. roughness) can be interpreted. A GNSS-R DDM depicts the scattered power off an observed surface. In forward scattering, the main contribution comes from the specular point (SP) and the area around it, which is called the glistening zone. The received signal

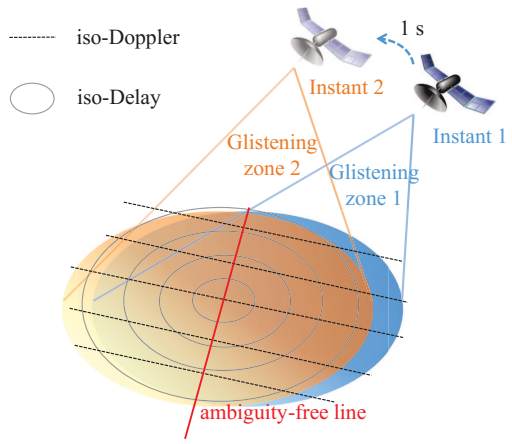

Figure 1.1: A schematic of spaceborne GNSS-R.

can be considered as a superposition of scattering components from different points on the observed surface. Each component has its corresponding delay and Doppler shifts (which are caused by different path lengths and the relative motions of the transmitter, the receiver and the scattering point). Accordingly, each DDM pixel is associated with the scattering strength off corresponding clusters in the spatial domain and the relationship is shown in a concise form, as Fig. 1.2. In this thesis, GNSS-R DDM data is employed for realizing sea ice remote sensing.

1.2 Literature Review

Sea ice remote sensing using GNSS-R was first demonstrated with an airborne GPS Rx in [58]. Since then, several ground-based and airborne experiments have been

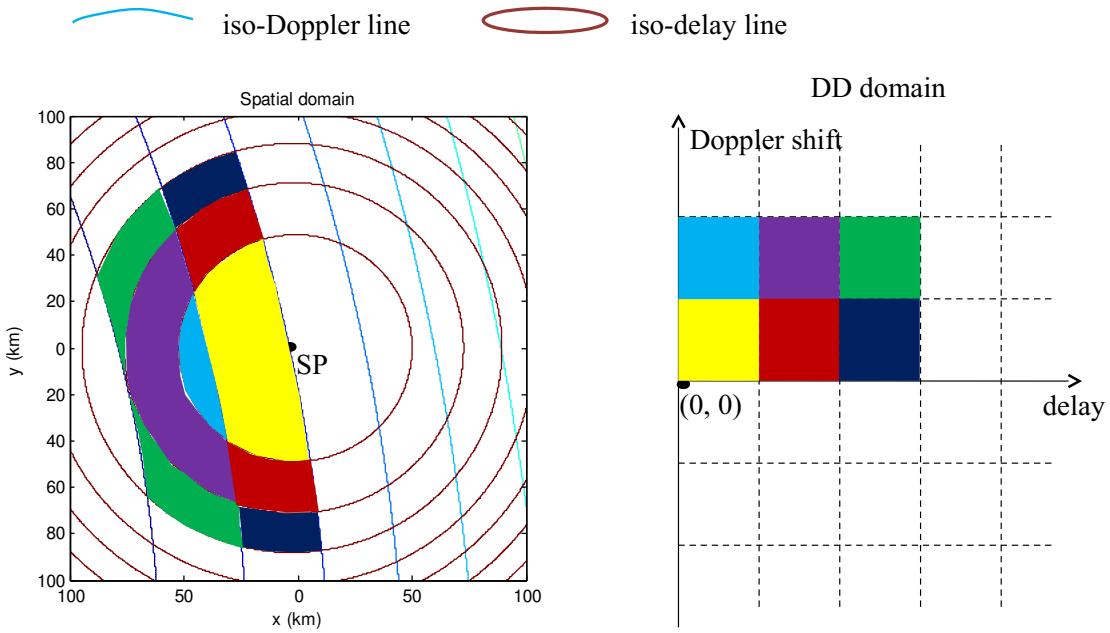

Figure 1.2: Relationship between spatial clusters and DDM pixel. The same color indicates the association between the spatial clusters and DDM pixel. For conciseness, only selected pairs have been demonstrated.

accomplished with promising results [53], [54], [59]–[61]. The first spaceborne GNSS-R measurement was carried out during the UK Disaster Monitoring Constellation (UK-DMC) mission in 2004 showing its capability for use in sea ice remote sensing. In this section, the techniques of sea ice remote sensing using GNSS-R are reviewed, being divided into three categories based on the platform types, i.e., spaceborne, airborne and ground-based.

1.2.1 Spaceborne Results in Sea Ice Sensing

The first acquisition of GNSS-R signal from space was performed by the UK-DMC satellite, and its application for sea ice sensing was demonstrated in [62]–[64]. Two sets of measurements were acquired, one on February 4, 2005 off the coast of Alaska with a total of 7 s of data, and the other on June 23, 2005 near Antarctica in the Southern Ocean with an additional 9 s of data. Referred to *in situ* sea ice validation data, the first measurement was obtained from a region with 90% area covered by first-year sea ice of 30 to 70 cm thickness. For the second collection, the *in situ* sea ice concentration (SIC) was between 70% and 90%. Compared to the acquired GNSS-R signals from June 23, the data collected on February 4 showed stronger peak and less spreading in the DDM. The comparison illustrated that the rough seawater surface could decrease the overall coherent specular reflection and lead to a larger glistening zone, which corresponds to a DDM with more spreading along delay and Doppler axes. Although the available GNSS-R data were limited, the analysis indicated the viability of observing ice-covered regions using spaceborne GNSS-R. In addition, the varying signal power and extent of spreading in delay and Doppler associated with

different SIC values demonstrated the potential of GNSS-R for SIC estimation. It was also mentioned in [63] that for a coherent signal off the ice surface, the carrier phase information can be recovered for accurate altimetry measurement, indicating the altimetric application of GNSS-R.

The analyses of space-detected GNSS-R signals reflected off sea ice in [63] were promising, although, up to the publication time of [63] in 2006, their use had yet to be explored due to lack of data. This situation was remedied with the launch of TechDemoSat-1 (TDS-1) in 2014, which made millions of DDMs available.

Except the work accomplished by this research, which has been published in e.g. [65]–[72], sea ice remote sensing using TDS-1 GNSS-R data has also been investigated by other researchers at almost the same time. In [66], the first application of TDS-1 data for sea ice detection was performed through evaluating the proposed observables extracted from DDMs. Later, [73]–[75] also investigated sea ice detection application with different observables and achieved similar accuracy. As an extension of the work done by Yan and Huang [66], Zhu *et al.* [76] derived a DDM observable, specifically Pixel Number and Power Summation, based on the difference of two normalized DDMs acquired consecutively. Through evaluating the value of obtained observables, the method is able to determine the type of surface transition. By retrieving the scattering coefficient (σ^0) in the spatial domain from TDS-1 DDMs, [77], [78] offered a new perspective on observing water/ice transitions and detecting sea ice. The method in [77] is based on the 2-D truncated singular value decomposition (TSVD), while that in [78] involves the spatial integration approach (SIA) [79] and multi-scan technique.

A strong sensitivity of the GNSS-R signals to the surface roughness of several

primary ice types, i.e., first-year ice (FYI), multi-year ice (MYI), and young ice was investigated in [80]. The difference in the shape of DDMs for various ice types was observed. Accordingly, several DDM observables were developed for sea ice type classification. Firstly, only the DDMs of sea ice are selected by evaluating these observables similar to those will be described in Chapter 2. Next, data of each sea ice type are randomly and equally divided into two groups for training and validation, respectively. Since the classification of ice type cannot be accomplished by inspecting these observables alone, the standard classification and regression tree (CART) method (see [81]) is adopted for training. In [80], the CART was built with 181 nodes, and the derived observables are the inputs to the CART. Each node can contain conditional control statements that are based on the evaluation of input observables and classification result. The complete algorithm in the form of pseudo-code can be found in [80]. This algorithm produces an accuracy 54.5%, 94%, and 69.7% for classifying FYI, MYI and Young Ice, respectively.

Another argument made in [63] was that the coherent reflection from ice surfaces allows accurate altimetry measurements, which was later verified in [82] through investigating delay waveforms and in [83] via processing phase measurements of raw data. The estimated precision is about 1 m with a spatial resolution of 3.8 km for phase-based method. The RMSD between the achieved GNSS-R altimetric results and mean sea surface is 4.7 cm with an along-track sampling distance of about 140 m for waveform-based approach.

A summary of sea ice sensing studies using TDS-1 GNSS-R is presented in Table 1.1. It can be noticed that the detection accuracy appear to be similar for both DDM observables-based methods and machine learning-based methods. The difference of

these two kinds of methods lies in that the latter methods perform classification through a learning process exclusively dependent on the data, while the former ones are based on interpretations by researchers. The difference between DDMs of sea ice and seawater is clear, which can be well represented by the derived observables, and thus the accuracy is plausible. However, it is challenging to deal with complex problems such as SIC estimation and sea ice type classification by solely using observables, and in such cases machine learning methods can be adopted. For sea ice altimetry, the phase-based method shows better performance than the waveform-based one, which is due to 1) an extra error mitigation processed by the former, 2) the restriction on delay resolution of waveform by the latter, and 3) shorter integration time adopted by the former that results in better spatial resolution.

1.2.2 Airborne Experiments

In addition to spaceborne applications, there have been several dedicated missions based on airborne and ground-based GNSS-R receivers capable of providing regional and local sea ice monitoring. However, these dedicated tests are of relatively limited generality and access compared with spaceborne applications. Nonetheless, their progress has been important for developing and validating new GNSS-R-based sea ice sensing practices. In this subsection, the contributions of recent airborne experiments are described and those for ground-based are reviewed in next subsection.

The first airborne sea ice measurement was performed in 1998 in the Beaufort Sea. The results showed the sensitivity of reflected GPS signals to the presence of sea ice and its conditions [58]. During the flight, the received signal shape had consistently

Table 1.1: Applications of Sea Ice Sensing Using TDS-1 GNSS-R Data

Application	Source	Technique	Accuracy
Detection	[66]	Observable-based	97.78%
Detection	[73]	Observable-based	
Detection	[76]	Observable-based	
Detection	[77]	TSVD-based σ^0 retrieval	
Detection	[78]	SIA-based σ^0 retrieval	
Detection	[75]	Observable-based	
Detection	[74]	Observable-based	
Detection	[70]	SVM	98.56%
Detection/SIC	[67]	NN	98.41%/0.93 (r)
Detection/SIC	[68]	CNN	98.73%/0.93 (r)
SIC	[71]	SVR	0.94 (r)
Type Classification	[80]	CART	
Altimetry	[82]	Waveform-based	4.4 m (RMSD)
Altimetry	[83]	Phase-based	4.7 cm (RMSD)

a sharp and narrow waveform, which indicates a trivial variation in the ice surface roughness observed. However, the peak power of the waveform changed significantly, which suggested the sensitivity to ice reflectivity. In addition, a correlation between the power of received signals and collocated RADARSAT backscatter was observed.

The potential of reflected GPS signals for the retrieval of sea ice information, specifically, permittivity and roughness, was further evaluated in [59]. These two derived parameters are retrieved from obtained waveforms using the Zavorotny-Voronovich (ZV) model [84]. It was shown in [59] that the received waveform can be modeled as the product of the reflection coefficient and the GPS coarse/acquisition (C/A) code autocorrelation function. For this reason, the power and shape of a waveform are decoupled to derive the permittivity and roughness, separately. The surface permittivity is mapped from the peak power via reflection coefficient, and the surface roughness (parameterized by surface mean square slope) is based on a least squares fitting between the modeled and measured waveforms.

1.2.3 Ground-based Tests

In addition to verifying the altimetric application, ground-based experiments conducted in Greenland in 2008 [51], [53] also provided polarimetric analysis from which a qualitative matching was found between the polarization ratio (a ratio between the received right-handed and left-handed circular polarization (RHCP and LHCP) signals) and SIC.

Signal-to-noise ratio (SNR) data of received reflected GNSS signals were collected at the Onsala Space Observatory, Sweden in 2012 [61], [85]. The high-frequency part

of the SNR data, referred to as δSNR, can be modeled as [85]

$$\delta\text{SNR} = \left[C_1 \cos\left(\frac{4\pi h}{\lambda}\sin\theta\right) + C_2 \cos\left(\frac{4\pi h}{\lambda}\cos\theta\right)\right] \times \exp\left(-4k^2\zeta\cos^2\theta\right) \quad (1.1)$$

where λ is the signal wavelength, h is the height of receiver above the reflecting surface, θ is the incidence angle, C_1 and C_2 are the amplitudes of each component, respectively, and ζ is referred to as the damping parameter i.e. the height variance of the reflecting surface. C_1, C_2, m, and ζ can be determined through nonlinear least squares fitting using Eq. (1.1). It was found in [61] that low values of ζ (significantly lower than 1) were coincident with the presence of ice, and thus ζ can be used for ice detection.

In 2013, tests were carried out at the Bohai Bay (China), and the ratio between direct and reflected signals (ρ) was found to be sensitive to SIC [54].

The ratio ρ was further investigated for sea ice thickness (SIT) retrieval, and an empirical relationship between these two parameters was obtained through a fitting process based on data collected at the field demonstration at Liaodong Bay (China) in 2016 [60]. Such an empirical formula was given as

$$\text{SIT} = 2.086\rho^{-0.021} - 2.697. \quad (1.2)$$

This was verified in [60] for sea ice with a thickness of 10 to 20 cm.

The above-mentioned ground-based investigations are summarized in Table 1.2.

1.3 The Scope of the Thesis

The representative GNSS-R satellites include UK-DMC (2003), TDS-1 (2014), and CYGNSS (2016), however, the first does not provide sufficient data and the last does

Table 1.2: List of Ground-based GNSS-R Techniques for Sea Ice Sensing.

Application	Source
Altimetry, SIC	[51], [53]
Detection	[61], [85]
SIC	[54]
SIT	[60]

not cover polar regions. Thus, this thesis research addresses sea ice remote sensing using TDS-1 data. The thesis is organized as follows:

In Chapter 2, a scheme is presented for detecting sea ice by investigating DDM observables. Furthermore, three machine learning-based methods, specifically, neural networks (NNs), convolutional neural networks (CNNs), and support vector machines (SVMs), for both sea ice detection and SIC estimation are described in Chapter 3, Chapter 4 and Chapter 5, respectively. Chapter 6 demonstrates and discusses experimental results for these different methods. Chapter 7 presents an approach for retrieving sea ice thickness from TDS-1 measurements. Chapter 8 concludes with an overview and future improvements on this research, as well as discussion on some related work.

The research presented in this thesis has been published or submitted for review in six refereed journal papers as listed below:

1. Q. Yan and W. Huang,"Sea ice remote sensing using GNSS-R: A review", *Remote Sens.*, vol. 11, no. 21, 2565, 2019.

   This paper provides a review of the sea ice remote sensing using GNSS-R data

(Chapter 1).

2. Q. Yan and W. Huang, "Spaceborne GNSS-R sea ice detection using delay-Doppler maps: First results from the U.K. TechDemoSat-1 mission," *IEEE J. Sel. Top. Appl. Earth Obs. Remote Sens.*, vol. 9, no. 10, pp. 4795–4801, Oct. 2016.

   This paper presents the DDM observable-based methods for sea ice detection (Chapter 2).

3. Q. Yan,W. Huang, and C.Moloney, "Neural networks based sea ice detection and concentration retrieval from GNSS-R delay-Doppler maps," *IEEE J. Sel. Top. Appl. Earth Obs. Remote Sens.*, vol. 10, no. 8, pp. 3789–3798, Aug. 2017.

   This paper presents the NN-based method for sea ice detection and SIC estimation using DDM data (Chapter 3).

4. Q. Yan and W. Huang, "Sea ice sensing from GNSS-R data using convolutional neural networks," *IEEE Geosci. Remote Sens. Lett.*, vol. 15, no. 10, pp. 1510–1514, Oct. 2018.

   This paper introduces CNN-based sea ice remote sensing from DDM data (Chapter 4) and compares its performance with NN's (Chapter 6).

5. Q. Yan and W. Huang, "Detecting sea ice from TechDemoSat-1 data using support vector machines with feature selection," *IEEE J. Sel. Top. Appl. Earth Obs. Remote Sens.*, vol. 12, no. 5, pp. 1409–1416, May 2019.

This paper proposes the SVM-based sea ice detection method (Chapter 5) and provides comparison of detection accuracy between the NN-, CNN-, and SVM-based algorithms (Chapter 6)

6. Q. Yan and W. Huang, "Sea ice thickness measurement using spaceborne GNSS-R: First results with TechDemoSat-1 data," *IEEE J. Sel. Top. Appl. Earth Obs. Remote Sens.*, vol. 13, pp. 577-587, 2020.

   This paper presents the reflectivity-based method for SIT retrieval from GNSS-R data (Chapter 7).

Chapter 2

Sea Ice Detection Using Delay-Doppler Map (DDM) Observables

In this chapter, for the first time, a scheme is developed for distinguishing the surface area covered by sea ice from that of seawater by evaluating the degree of spreading of a DDM which indicates the surface roughness.

Roughness of oceans can vary considerably, but can still be assumed to be rougher than ice. Therefore, non-specular regions of the ocean at delay-Doppler offsets are more likely to reflect a GNSS signal towards the receiver. Thus, typical DDMs of ocean surfaces exhibit a clear horseshoe shape [22], [23]. In 2005, the UK-DMC satellite collected two sets of reflected GNSS signals (16 s in total) off sea ice [63]. Through analysis, it was found that in contrast to signals scattered off the sea surface without ice, signals reflected from ice have a significant coherent reflection component

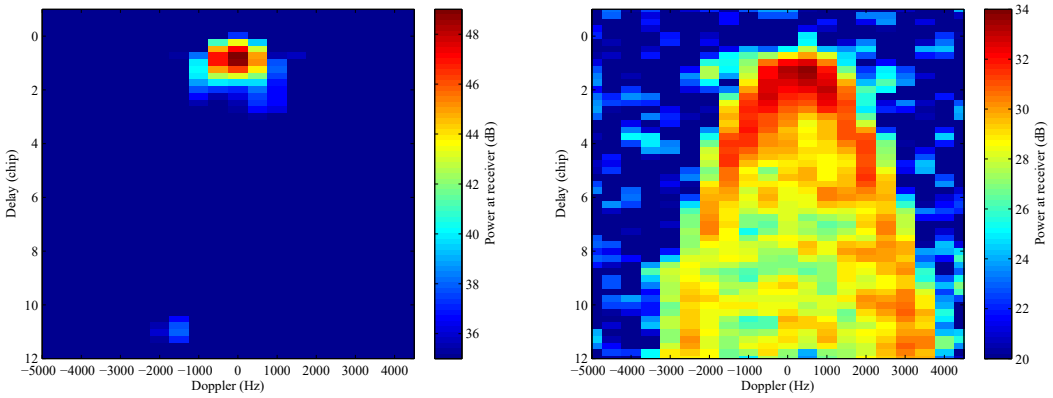

(a) (b)

Figure 2.1: GNSS-R DDMs collected by TDS-1 on Feb. 20, 2015 over: (a) sea ice and (b) seawater with 1-s incoherent summation.

[63]. Coincidentally, it has been reported in [86] that the vast majority of signal returns (or waveforms) acquired by satellite altimeters exhibit many more specular characteristics over sea ice than echoes from the open seawater, with higher peak power value and narrower waveform width. In the DDM of sea ice, less spreading along delay and Doppler axes and a higher maximum power value are observed compared with the horseshoe-shaped DDM of seawater (see Fig. 2.1), and these differences allow us to distinguish sea ice from seawater areas.

2.1 Descriptors for DDM Spreading

Several different descriptors that measure the DDM spreading caused by surface roughness have been proposed in [20] and [21]. Moreover, based on previous results in [63] and examples of Fig. 2.1, it is clear that the distinction between DDMs of sea ice and seawater lies in the less spreading in the former over the latter. Hence, these

DDM observables are employed (with slight modification) in this research to classify the corresponding area covered by sea ice or seawater through evaluating the observable values. These observables are derived from the normalized DDM ($\overline{DDM}(\tau, f)$) above a preset threshold (DDM_{thres}), where τ and f are delay and Doppler shift. The observables are presented in the following subsections.

2.1.1 Number of DDM Pixels

In [20] an observable is defined as the area of the $\overline{DDM}$ with power greater than a given DDM_{thres}, as

$$\text{Area} = \sum\sum_{\overline{DDM}(\tau,f)>DDM_{thres}} \tau_\delta \cdot f_\delta, \tag{2.1}$$

where τ_δ and f_δ represent the resolutions of delay and Doppler shift. By simply assuming the "area" of each DDM pixel is dimensionless and equal to one (i.e., $\tau_\delta \cdot f_\delta = 1$), this observable represents the number of DDM pixels with normalized power greater than the pre-set DDM_{thres} and, hereafter, is denoted as Pixel Number = Area.

2.1.2 Summation of DDM Powers

A similar observable, DDM volume, was proposed in [20] and modified as weighted area in [21], which is formulated as

$$\text{Weighted Area} = \sum\sum_{\overline{DDM}(\tau,f)>DDM_{thres}} \overline{DDM}(\tau, f) \cdot \tau_\delta \ f_\delta. \tag{2.2}$$

By setting $\tau_\delta \cdot f_\delta = 1$, this observable depicts the normalized power summation of $\overline{DDM}(\tau, f)$ with a value greater than the preset DDM_{thres} (hereafter, Power Summation, I_0 = Weighted Area).

2.1.3 Center-of-Mass Distance Observable

This observable is calculated as the distance from the center of mass [CM, with a coordinate of (CM_τ, CM_f)] to the peak power point [with a coordinate of (MAX_τ, MAX_f)] of each DDM (hereafter, CM Distance) as follows

$$\text{CM Distance} = \tau_\delta f_\delta \sqrt{\left(\frac{MAX_\tau - CM_\tau}{\tau_\delta}\right)^2 + \left(\frac{MAX_f - CM_f}{f_\delta}\right)^2}, \tag{2.3}$$

where CM_τ and CM_f are defined as [21]

$$CM_\tau = I_0^{-1} \sum_{\overline{DDM}(\tau,f) > DDM_{thres}} \sum \tau \cdot \overline{DDM}(\tau, f) \cdot \tau_\delta \; f_\delta \tag{2.4}$$

$$CM_f = I_0^{-1} \sum_{\overline{DDM}(\tau,f) > DDM_{thres}} \sum f \cdot \overline{DDM}(\tau, f) \cdot \tau_\delta \; f_\delta. \tag{2.5}$$

CM Distance and the subsequent two observables in subsection 2.1.4 and 2.1.5 were developed in [21].

2.1.4 Geometrical Center Distance Observable

This observable is determined as the distance from the geometrical center [GC, with a coordinate of (GC_τ, GC_f)] to (MAX_τ, MAX_f) of the corresponding DDM (hereafter, GC Distance), which is formulated as

$$\text{GC Distance} = \tau_\delta f_\delta \sqrt{\left(\frac{MAX_\tau - GC_\tau}{\tau_\delta}\right)^2 + \left(\frac{MAX_f - GC_f}{f_\delta}\right)^2}, \tag{2.6}$$

where GC_τ and GC_f are defined as [21]

$$GC_\tau = \left(\sum_{\overline{DDM}(\tau,f) > DDM_{thres}} \tau \cdot \tau_\delta \right) / \left(\sum_{\overline{DDM}(\tau,f) > DDM_{thres}} \tau_\delta \right) \tag{2.7}$$

$$GC_f = \left(\sum_{\overline{DDM}(\tau,f) > DDM_{thres}} f \cdot f_\delta \right) / \left(\sum_{\overline{DDM}(\tau,f) > DDM_{thres}} f_\delta \right). \tag{2.8}$$

2.1.5 Center-of-Mass Taxicab Distance Observable

This observable (hereafter, CM Taxicab Distance) is determined based on the taxicab distance from the CM to (MAX_τ, MAX_f) of a DDM (which is defined as $|MAX_\tau - CM_\tau| + |MAX_f - CM_f|$), as follows

$$\text{CM Taxicab Distance} = \tau_\delta f_\delta \left(\left| \frac{MAX_\tau - CM_\tau}{\tau_\delta} \right| + \left| \frac{MAX_f - CM_f}{f_\delta} \right| \right) \tag{2.9}$$

As mentioned above, DDMs of sea ice are less spread along delay and Doppler axes relative to the horseshoe-shaped DDMs of seawater. As a result, for sea ice, the number of pixels with intensity above a given DDM_{thres} in the DDMs is typically small and those pixels are near the peak power point, while those for seawater are mainly on the horseshoe-shape portion and are more spread. Consequently, the associated center of mass and geometrical center points in DDMs over seawater are usually farther from the peak power points. Thus, it is expected that the observables derived from DDM of sea ice will be lower than those obtained from DDM of seawater as demonstrated in Fig. 2.1.

2.2 DDM Data Processing

In order to obtain $\overline{DDM}(\tau, f)$ for observable computation, each measured DDM is processed with 1) noise floor subtraction, 2) incoherent summation, and 3) normalization. To reduce the effect of noise fluctuation due to antenna and instrument system noise variation, the noise floor is first subtracted from each DDM [21], [23], [63], which can be calculated using the following expression

$$\text{Noise} = \frac{1}{N} \sum_{\tau=\tau_1}^{\tau_2} \sum_{f=f_1}^{f_2} DDM(\tau, f), \tag{2.10}$$

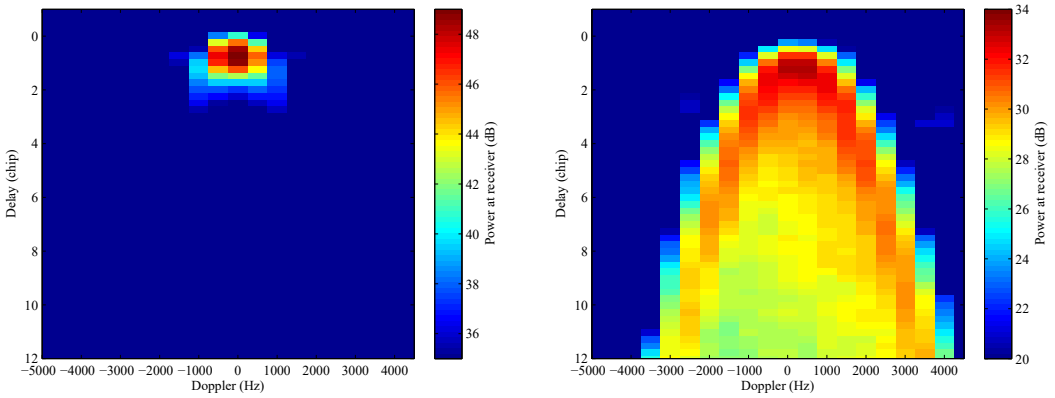

(a) (b)

Figure 2.2: GNSS-R DDMs collected by TDS-1 on Feb. 20, 2015 over: (a) sea ice and (b) seawater with 21-s incoherent summation.

where τ_1, τ_2, f_1 and f_2 are the pixel limits of a noise box in a signal-free DDM area, and N is the number of pixels within the noise box. By following the manner in [24], the noise box is chosen as the DDM area of the first four delay rows spanning all Doppler bins (twenty).

After the noise level subtraction, an incoherent summation can be applied to each DDM so that the speckle noise can be mitigated [23], [87]. For example, Fig. 2.2 illustrates DDMs of sea ice and seawater after a 21-s incoherent summation. Instead of using a fixed duration (e.g., 18 s utilized in [23]), an adaptive incoherent summation is applied here (see detailed description below), where the length of summation depends on surface types. As the GNSS-R SP ground track traverses oceans and continents, DDMs can be collected across transition areas with different surface types, such as land and ocean. For this reason, DDMs that were collected close to surface transitions will be assigned with relative shorter incoherent summation lengths to avoid

the averaging between those acquired over different surfaces. Therefore, an adaptive incoherent averaging interval is employed to ensure the incoherent summation is processed over consecutive coherent correlations. It should be noted that an ideal method would incoherently sum any number of consecutive coherent looks but there exists a lower limit of 1000 looks (or 1-s incoherent summation) due to the TDS-1 DDM generation parameters.

Specifically, for an ocean-land transition, the DDM with an SP near the intersection of ground track and coastline will be assigned with a short incoherent time that is based on the distance from its SP to the intersection. Coastline distribution can be obtained using geographic information. Details regarding the calculation of SP position can be found in [64].

Similar practices should also be operated for DDMs acquired over possible transitions between seawater and sea ice. As mentioned earlier, the maximum power value in a DDM (obtained after the noise subtraction) offers another indicator for the presence or absence of sea ice and, subsequently, abrupt changes in DDM peak powers along the track are assumed to be potential transitions between sea ice and seawater. In application, based on the distance from its SP to a potential transition area (land-ocean and sea ice-seawater), a DDM may be averaged with its adjacent DDMs (up to 20), and, correspondingly, the interval of adaptive incoherent summation ranges from 1 s to 21 s (each DDM from TDS-1 datasets has been processed 1-s incoherent integration). A 2017 study [88] showed that TDS-1 reflections over ice are mostly coherent, which makes the along-track resolution of approximately 1×7 km^2 (the motion of the footprint during an incoherent summation interval of 1 s is 7 km). Thus, for the case of purely coherent ice reflections, the method proposed here will

provide a resolution of up-to $1 \times 7L$ km^2, where L is the applied adaptive incoherent summation length (from 1 to 21 s).

After the incoherent summation, the averaged DDM is normalized with respect to its peak power and the normalized result has a range of [0,1]. Meanwhile, its peak power averaged by its associated incoherent summation length is recorded.

2.3 Sea Ice Detection Scheme

With $\overline{DDM}(\tau, f)$, the DDM observables presented in Section 2.1 can be obtained with a given DDM_{thres}. It has also been illustrated in Section 2.1 that these DDM observables represent the spreading in a DDM and the more spreading in a DDM the greater the observable values, and therefore, observables usually have higher values for DDMs of seawater than those for sea ice. Hence, sea ice detection can be accomplished through evaluating the value of the DDM observable and the area associated with a DDM that results in an observable below a pre-set threshold will be interpreted as covered by sea ice.

It is worth mentioning that by applying the adaptive incoherent summation, DDMs with a longer incoherent summation interval will gain a higher SNR that is proportional to the square of the number of incoherent summation [63]. Thus, it can be expected that the value of a DDM observable depends on the incoherent summation length applied to the corresponding $\overline{DDM}(\tau, f)$. Accordingly, an adaptive threshold is utilized for each observable to detect sea ice, which is based on the individual incoherent summation interval applied to each DDM. As is introduced in subsection 6.3.1, values of thresholds for detection can be determined from a training

dataset.

It should also be noted that it may not be appropriate to directly employ the value of DDM peak power as a descriptor for sea ice detection for universal purposes, since the value may vary significantly from each observation even over the same sea ice area due to variations in system noise levels and atmospheric conditions [24]. On the other hand, the analysis of the changing trend in the peak power may offer an opportunity to recognize sea ice surfaces [58]. Consequently, the detection results will be inspected with the variation tendency of the updated peak powers, and the anomaly in ice detection will be corrected if the associated DDM peak power has similar value (within 50% to 200%) of adjacent ones. Based on the above discussions, sea ice detection from DDMs has been investigated and the corresponding process flowchart is displayed in Fig. 2.3.

The accuracy of sea ice detection based on the above-mentioned DDM observables is assessed in Chapter 6.

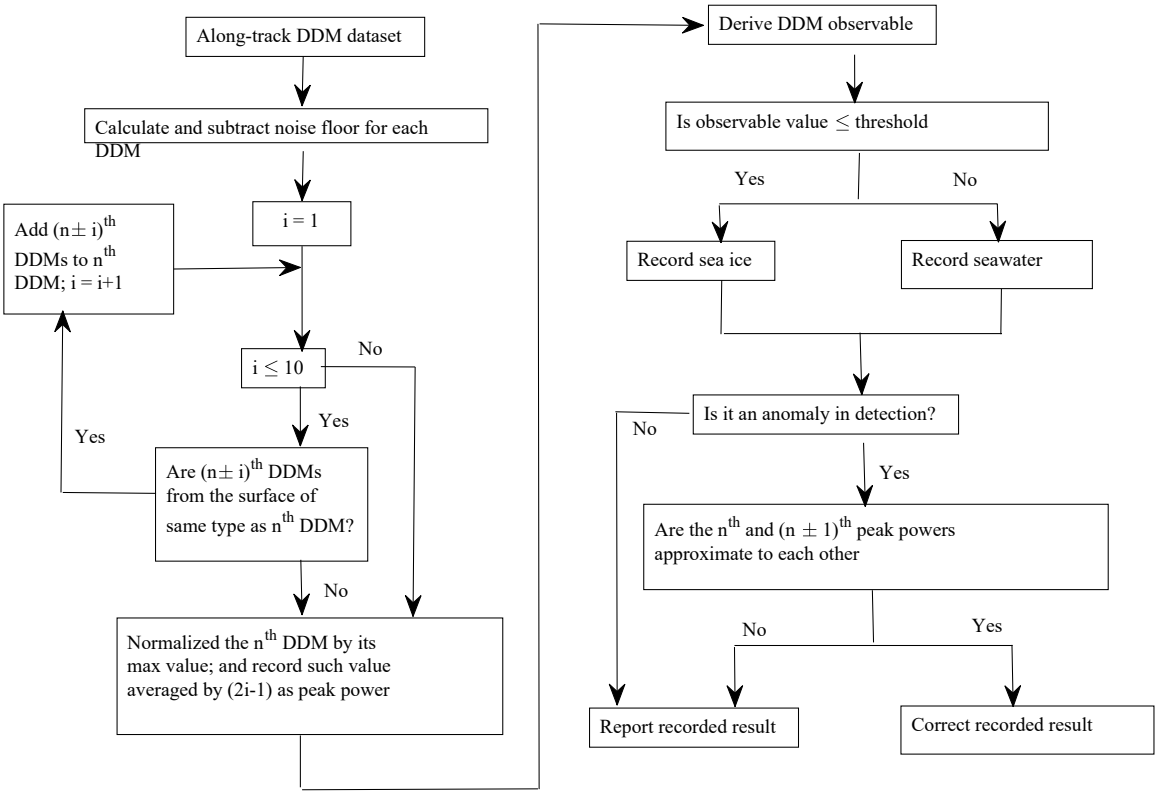

Figure 2.3: Flowchart of sea ice detection from GNSS-R DDMs.

Chapter 3

DDM-Based Sea Ice Sensing Using Neural Networks (NNs)

The technique of neural networks (NNs) has been identified as a robust candidate for improving existing sea ice remote sensing applications [89] because the NN is able to approximate large varieties of functions without *a prior* assumption about their distribution, and to develop decision surfaces of any configuration using a learning process [90]. The NN-based sea ice remote sensing has already shown great potential with many different types of data (e.g., SAR images [91] and passive microwave data [89]). However, to the author's knowledge, there is no previous research addressing NN-based sea ice remote sensing using GNSS-R DDMs. In this chapter, the technique of neural networks is applied to DDMs, for the first time, for the purposes of detecting sea ice and estimating sea ice concentration. The NN for sea ice detection is devised with a classification layer, whereas a regression layer is used for SIC estimation.

3.1 Association between NN and DDM

A neural network devises a structure for complex data processing using information-processing units, also known as neurons. Typically, a network consists of the input layer, one or more hidden layers and an output layer. The adjacent layers are connected by activation functions parameterized by weights. The activation functions are usually pre-defined and the weights are determined through a training process. Consequently, a trained network can be regarded as an input-output mapping [92].

As noted in Section 1.1, the surface scattering properties (for example, roughness) can be interpreted based on a DDM. In remote sensing area, it is well known that the scattering characteristics of sea ice and seawater differ from each other. Correspondingly, the DDMs of seawater and sea ice surfaces will be distinct. In addition, it is believed that the ratio of sea ice to seawater (i.e., SIC) within the region of interest will affect the DDMs (see Fig. 3.1). As such, the sea ice remote sensing from DDMs is feasible and investigated using the NN technique here. Sea ice detection using DDM observables (presented in Chapter 2) is based on empirical interpretation, instead, NNs proceeds sea ice sensing exclusively from the data.

The general NN procedure for the application here consists of three steps: preprocessing of the input (DDM, in this study) data, training of the NN, and estimation of ice information from another set of data using the trained NN. A corresponding flowchart is presented in Fig. 3.2.

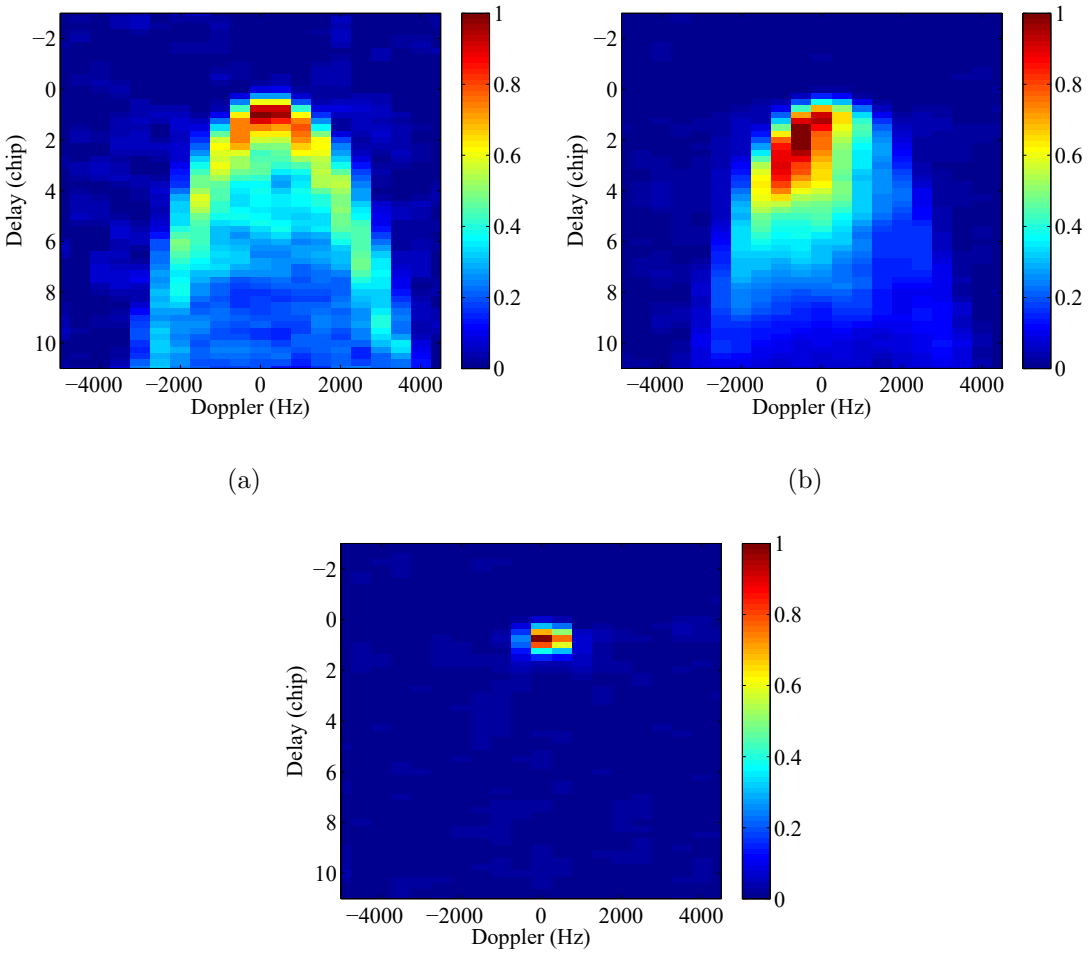

(a) (b)

(c)

Figure 3.1: GNSS-R DDMs collected by TDS-1 over regions with different SICs: (a) 0%, (b) 50%, and (c) 92%, respectively. The SIC values are obtained from collocated reference data, which are described in subsection 6.1.2. All DDMs have been normalized with power values from 0 to 1.

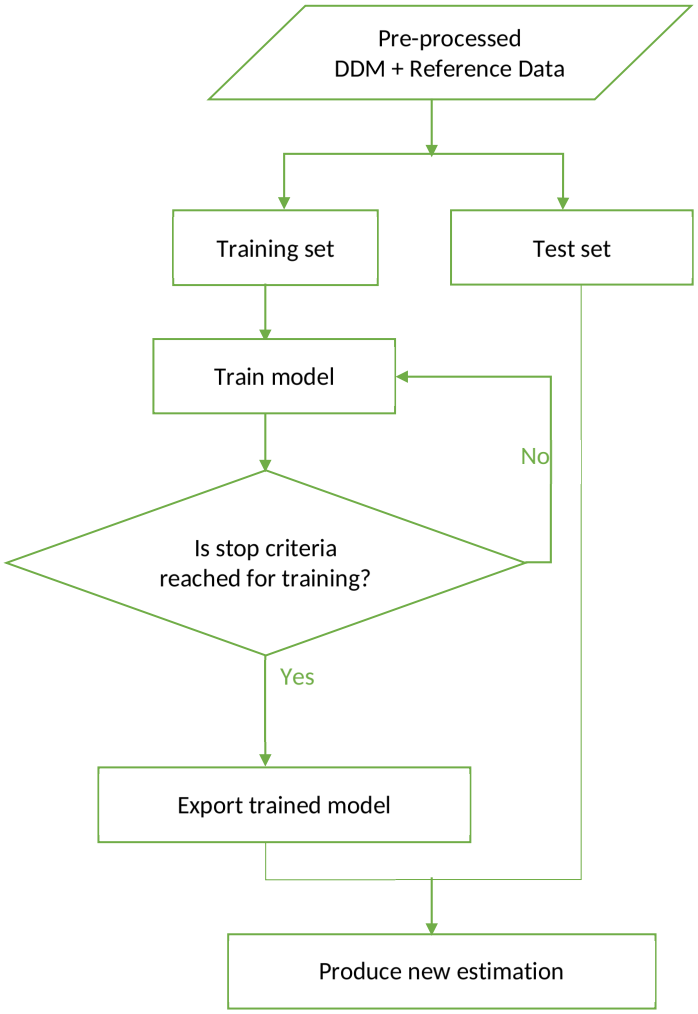

Figure 3.2: Flowchart of general processes for machine learning-based sea ice sensing techniques.

3.2 DDM Data Preprocessing

Each measured DDM is processed with 1) noise floor subtraction, 2) normalization, 3) signal box determination, and 4) data stretching. The first two steps follow the procedure in Section 2.2 and the remaining steps are described in the following section.

3.2.1 Signal Box Determination

The signal box is chosen based on the delay bin of the peak power point MAX_τ. Here, 40 bins along the delay axis (from MAX_τ - 4 to MAX_τ + 35) and all 20 bins along the Doppler axis are retained. Note that the original size of the TDS-1 DDM is 128 along the delay and 20 along the Doppler axis, respectively. It should be noted that the size of the signal box corresponds to a spatial coverage between 100 and 150 km (median value 125 km) depending on the elevation angle at the SP.

3.2.2 Data Stretching

The input layer of a neural network is in the form of a 1-D vector. Thus, the 2-D DDM needs to be reshaped. For each signal box, the DDM is sliced along the delay-axis, forming a 1-D vector with 800 elements. It is worth mentioning that the DDM can be sliced along either the delay- or the Doppler-axis. However, once one manner is chosen, all other DDMs should be treated in the same fashion so that all the DDM pixels can be presented to the network in the same form.

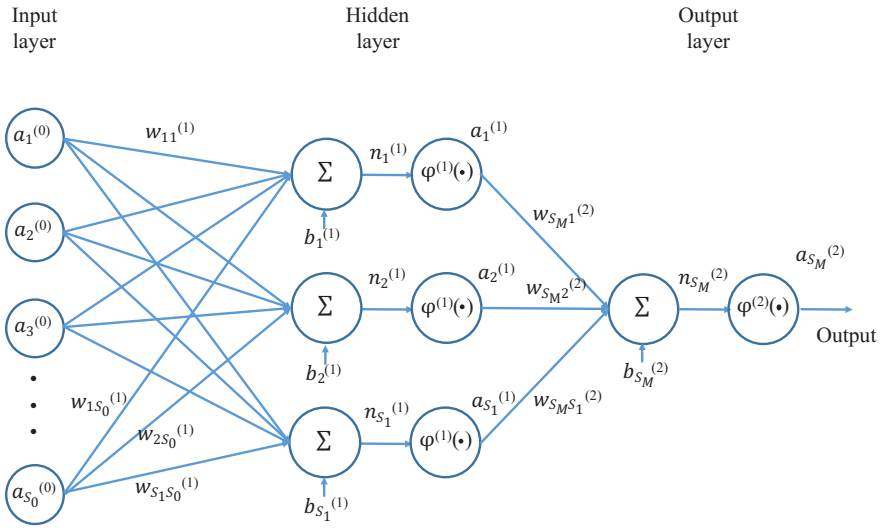

Figure 3.3: Diagram of a three-layer MLP.

3.3 NN Design

3.3.1 NN Structure

As pointed out in [93], a multilayer perceptron (MLP) NN with a single hidden layer is capable of approximating any continuous multivariate function to desired accuracy. Thus, an MLP was employed here (see Fig. 3.3) and was constructed with 800 inputs, 1 hidden layer consisting of 3 neurons, and 1 output. With reference to Fig. 3.3, $M = 2$ (the number of layers is $M+1$), the number of inputs $S_0 = 800 = 40\times20$, the number of hidden neurons $S_1 = 3$ and the number of output $S_M = S_2 = 1$. Through trial and error it was found that the accuracy was insensitive to the increase in S_1 while the computational time increased significantly. Hence, $S_1 = 3$ was selected by considering plausible performance in both accuracy and computational cost.

The DDM pixels from each DDM image will be presented to the input layer, as $a_l^{(0)}$, $l \in [1, 800]$ and the output will be SIC value (or, 0 or 1 for ice detection application), as $a_1^{(2)}$. More generally, the net input to neuron j in layer $k+1$ can be described by $n_j^{(k+1)}$ and the corresponding output will be $a_j^{(k+1)}$. In Fig. 3.3, S_k is the number of neurons in layer k, $w_{ji}^{(k+1)}$ represents the synaptic weights connecting neuron j in layer $k+1$ and neuron i in layer k, and $\varphi^{(k+1)}(\cdot)$ and $b_j^{(k+1)}$ denote the activation function and bias for neuron j in layer $k+1$, respectively. To be concise, not all weights are presented for the designed three-layer network in Fig. 3.3.

The relationship within the network can be given in the following concise matrix form:

$$\mathbf{a}^{(0)} = \mathbf{p}, \tag{3.1}$$

$$\mathbf{a}^{(k+1)} = \varphi^{(k+1)}(\mathbf{W}^{(k+1)}\mathbf{a}^{(k)} + \mathbf{b}^{(k+1)}), k \in [0, 1], \tag{3.2}$$

where $\mathbf{p}$ is the input DDM pixels vector and $\mathbf{a}^{(k+1)}$, $\mathbf{b}^{(k+1)}$ and $\mathbf{W}^{(k+1)}$ represent the input vector, the bias vector, and the weight matrix, respectively.

The activation function in the hidden was given by the widely used sigmoid function $\varphi^{(1)}(x) = 1/(1+e^{-x})$.

In the output layer, the activation function was assigned by the linear function $\varphi^{(2)}(x) = x$ for SIC estimation and by the $softmax$ function for sea ice detection (that calculates the probability of presence of sea ice).

3.3.2 Back-propagation Learning

The back-propagation learning [94] is a computationally efficient method for determining the synaptic weights [92]. This learning method consists of a forward pass

and a backward pass through the different layers of the network. The forward pass can be summarized by (3.1) and (3.2), during which the weights in the network are all fixed. During the backward pass, on the other hand, the weights are all adjusted based on the sum of the squared error, which is defined as

$$\varepsilon = \frac{1}{2}\sum_{q=1}^{Q}\mathbf{e}(q)^T\mathbf{e}(q), \tag{3.3}$$

where $\mathbf{e}(q) = \mathbf{t}(q) - \mathbf{a}^{(2)}(q)$ is the error for the qth input and Q is the number of input patterns, and $\mathbf{a}^{(2)}(q)$ and $\mathbf{t}(q)$ are respectively the actual and the desired output SIC values (or ice labelling values) when the qth input $\mathbf{p}(q)$ is presented. More details about the reference SIC and label data are described in Section 6.2. The aim of back-propagation learning is to minimize ε through adjusting weights. Among different algorithms for back-propagation learning, the Levenberg-Marquardt (LM) algorithm [95] is regarded as one of the most efficient, allowing for fast and stable convergence for networks with a few hundred weights [96]. The LM algorithm was employed to optimize ε by iteratively updating the weight vector $\mathbf{m}$ as

$$\text{new} \quad \mathbf{m} = \mathbf{m} - (\mathbf{J}^T\mathbf{J} + \mu\mathbf{I})^{-1}\mathbf{J}^T\mathbf{e}, \tag{3.4}$$

where $\mathbf{m} = [w_{11}^{(1)}w_{12}^{(1)}\cdots w_{S_1S_0}^{(1)}b_1^{(1)}\cdots b_{S_1}^{(1)}w_{11}^{(2)}\cdots b_{S_M}^{(M)}]^T$ (that consists of all the weights and biases in each layer), μ is the combination coefficient, $\mathbf{I}$ is the identity matrix. $\mathbf{e}$ contains the error for all Q input patterns, and $\mathbf{J} = \partial\mathbf{e}/\partial\mathbf{m}$ is the Jacobian matrix (see more details in [92], [96]).

In summary, the LM algorithm-based back-propagation learning is implemented as follows

1. Initialize $\mathbf{m}$ (or equivalently, $\mathbf{W}$ and $\mathbf{b}$) with random numbers, $\mu = 0.01$ and the

multiplication factor $\beta = 10$ (according to [96]) and present all input patterns to the network.

2. Proceed with the forward pass and compute the sum square error using (3.1)–(3.3).

3. Derive the Jacobian matrix $\mathbf{J}$.

4. Update $\mathbf{m}$ using (3.4). Recompute the sum square error with new $\mathbf{m}$. If the new ε is smaller than the previous one, retain the updated $\mathbf{m}$, decrease μ by β and go to step 2. Otherwise, keep the previous $\mathbf{m}$, increase μ by β and repeat this step.

5. This learning process stops when any of the following occurs (numbers in brackets were empirically employed for this work):

   - The preset maximum number (100) of epochs is reached.
   - μ exceeds the preset threshold (10^{10}).
   - The change in ε is below 0.001 among 10 adjacent epochs.

The training and testing are implemented in Chapter 6. In this chapter, the application of NN-based sea ice remote sensing (sea ice detection and SIC estimation) from spaceborne GNSS-R data is illustrated for the first time. In particular, it is the first application of SIC estimation from DDMs. This present chapter also opens a window for other machine learning methods for sea ice sensing, which are described in the following two chapters.

Chapter 4

Sea Ice Sensing Using Convolutional Neural Networks (CNNs)

Although good accuracy can be achieved for sea ice remote sensing from GNSS-R DDM using NNs (e.g. with an overall accuracy of 98.67% for sea ice detection; for more results see Chapter 6), it was hypothesized that CNNs might perform even better as they take advantage of the original data format (2-D) instead of the 1-D nature of the input to an NN. CNN has been successfully applied to sea ice remote sensing using, for example, synthetic aperture radar [14] and altimeter [97] data. However, to the author's best knowledge, the application of CNN in the area of GNSS-R has not yet been conducted. In this chapter, the CNN technique is applied to TDS-1 DDMs for the first time, dedicated to detecting sea ice and estimating SIC. Similar to the NN investigated in the previous chapter, the CNN for sea ice detection and

SIC estimation are designed with the classification and regression layers, respectively.

4.1 Design of CNN-based Sea Ice Remote Sensing

A CNN is able to establish the intrinsic connection between input-target pairs when they are well associated [98]. Typically, a CNN consists of a block of optional convolution layers, pooling layers, nonlinear layers, and fully connected layers, followed by an output layer. A convolution layer consists of a certain number of filters of specific sizes. Each filter is convolved with the input image and can be regarded as a feature extractor. The convolved images are then processed by an activation function (nonlinear layer) to produce feature maps which are the output of the convolution layer. A pooling layer subsamples the feature map to reduce its redundancy and the output of the last pooling layer is converted to a vector, which is followed by one or more fully connected layers (as in a traditional NN). The fully connected layer combines all of the features learned through previous layers to identify the desired patterns. Fig. 4.1 illustrates an example of a CNN. The filter parameters in the convolution layer and weights in the fully connected layer are learned through a training process.

As noted previously, a DDM describes the scattering strength of the GNSS-R signal off the observed surface. Each DDM pixel corresponds to its associated spatial clusters and this allows the fusion of a pixel with other data [99], e.g. SIC in this work. For this reason, a CNN is applied for sea ice detection and SIC estimation from DDM data. CNN applications generally include the following stages: 1) Data (DDM in this work) preprocessing, 2) training of the CNN, and 3) testing of the CNN using DDMs that are separate from training data.

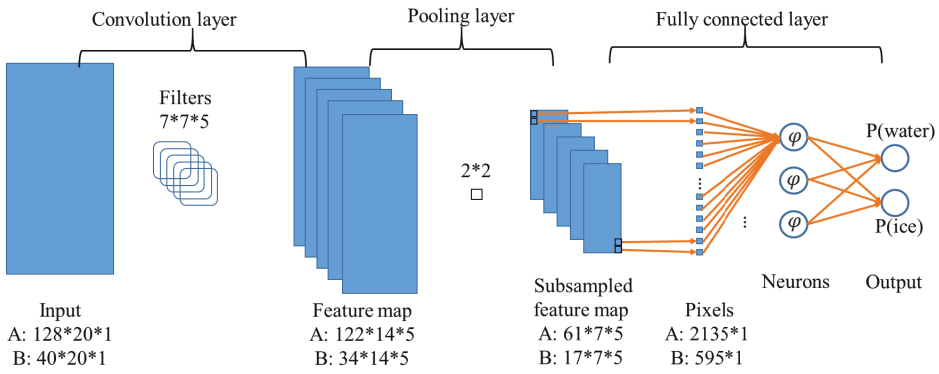

Figure 4.1: Employed CNN structure in this work. Set A parameters are associated with a full DDM input, set B for a cropped DDM input.

4.2 Preprocessing of DDM Images

The preprocessing of DDM data follows the procedures in Section 3.2. Specifically, it consists of noise floor subtraction, normalization, and (optional) signal box determination (see more details in subsection 3.2.1). It should be noted that the positions of DDM specular points are not aligned in all images (see Fig. 4.2 for illustration) due to variation in path length [24]. The last step is thus necessary for a NN so that the input is presented to the network in alignment. However, it is hypothesized that a CNN is able to extract the features independent of a DDM's position. Therefore, to demonstrate this, two different CNN structures, which employ full (128-by-20 pixels) and cropped (40-by-20 pixels, the adopted signal box in subsection 3.2.1) DDM images as input, respectively, were devised.

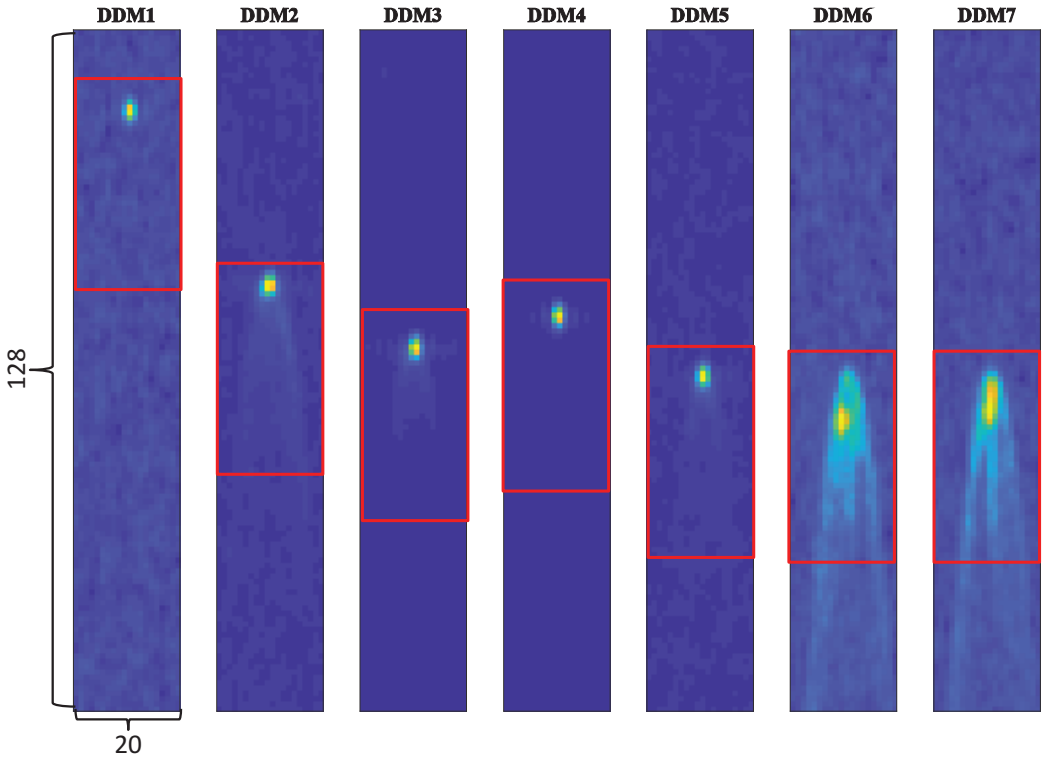

Figure 4.2: DDM samples in their original data format (128×20)- note that their specular points are not aligned. Red boxes indicate the cropped inputs (40×20) with box positions aligned frame to frame, and the box is selected following the fashion in subsection 3.2.1. Delay axes are vertical and Doppler axes horizontal.

4.3 Structure of CNN

The framework of the employed CNN for sea ice detection is presented in Fig. 4.1 (parameters of set A are for a full DDM and set B for cropped data). In order to reduce the size of network, only one convolution layer followed by one pooling layer and two fully connected layers are employed. The convolution layer is made of five 7×7 filters. Take the case of the CNN with full-size (128×20) input for example. Without padding along all edges, the convolved images are of size $(128-7+1, 20-7+1, 5)$, i.e., (122, 14, 5), the corresponding feature maps resulting from the kth ($k = 1, ..., 5$) filter, $\mathbf{W^k}$, can be described by

$$\begin{aligned} &\mathbf{h}_{ij}^k = \varphi((\mathbf{W}^k * \mathbf{X})_{ij} + b), \\ &i = 1, ..., 122,\ j = 1, ..., 14, \end{aligned} \tag{4.1}$$

where $\mathbf{X}$ and b are the input image and the bias. The convolution operation is denoted by $*$ and the activation function by φ. The widely adopted rectified linear unit (ReLU) is chosen for φ i.e.

$$\varphi(z) = \max(0, z). \tag{4.2}$$

The max pooling layer is of pooling size (2, 2) and stride (step size) 2 [14]. This layer preserves the maximum value of every non-overlapped 2×2 block in the feature map to generate a sub-sampled one of size (122/2, 14/2, 5), that is, (61, 7, 5). The first fully connected layer is thus of dimension 2315 (i.e. $61 \times 7 \times 5$). The second fully connected layer is equipped with 3 units, and this value is taken according to the previously designed NN (in Chapter 3) for later comparison of complexity between CNN and NN. The structure and functionality of fully connected layers are quite

similar to those of the hidden layers in NNs, and for conciseness, detailed formulations are in Section 3.3.

For sea ice detection (classification model), the output layer is designed with 2 units a_1 and a_2, and the activation function is the $softmax$ function, which gives the probability of occurrence of sea ice or seawater,

$$p_r = \frac{\exp(a_r)}{\sum_{s=1}^{2} \exp(a_s)}, \text{ where } r = 1, 2. \tag{4.3}$$

The detection result is based on the one with the higher value.

For SIC estimation purposes (regression model), the output layer shown in Fig. 4.1 is modified to have 1 unit (i.e., the concentration value), and a linear activation function,

$$f(z) = z, \tag{4.4}$$

is adopted.

It should also be noted that the overall layout of CNNs remains the same when a cropped DDM is used as input, only the size of each layer needs to be adjusted accordingly and this can be readily deduced following the procedure previously described as indicated in Fig. 4.1 by set B values.

4.4 CNN Training

Back-propagation learning [94] and mini-batch stochastic gradient descendant with momentum (SGDM) algorithm [100] are adopted for training. The learning method includes a forward propagation and a backward propagation. The forward propagation hereafter is denoted by F, during which the parameters are all fixed. During the

backward propagation, SGDM updates the parameters by slowly progressing in the direction of the negative gradient of the cost function to minimize the cost. The cost function over a mini-batch (whose size is arbitrarily chosen as 100 in this work) is given by

$$\varepsilon(F(\mathbf{X};\mathbf{W}),\mathbf{y}) = \frac{1}{100}\sum_{n=1}^{100}(F(\mathbf{X}_n;\mathbf{W})-\mathbf{y}_n)^2, \tag{4.5}$$

where the nth input and output within the mini-batch are denoted by $\mathbf{X}_n$ and $\mathbf{y}_n$. The parameters are updated over every mini-batch of the training data iteratively, through [100]

$$\begin{aligned}\mathbf{V}_{q+1} &= m\cdot\mathbf{V}_q - \eta\cdot\left\langle \tfrac{\partial\varepsilon}{\partial\mathbf{W}}\big|_{\mathbf{W}_q}\right\rangle \\ \mathbf{W}_{q+1} &= \mathbf{W}_q + \mathbf{V}_{q+1}\end{aligned}, \tag{4.6}$$

where q is the iteration index, $\mathbf{V}$ is the momentum variable, $\left\langle (\partial\varepsilon/\partial\mathbf{W})|_{\mathbf{W}_q}\right\rangle$ is the average over the qth batch of the derivative evaluated at $\mathbf{W}_q$, the learning rate η is set as 0.001 and the momentum m as 0.95. Here, a scheme of epoch training [100] is selected, where an epoch means a full pass over all mini-batches.

In summary, mini-batch SGDM-based back-propagation learning for filter parameters is conducted as follows.

1. Initialize $\mathbf{W}$ with random numbers (Gaussian distributed with mean 0 and standard deviation 0.01) and present all training data (input and target) to the network.

2. Proceed with forward propagation F and compute the cost function using (4.5).

3. Update $\mathbf{W}$ using (4.6).

4. This training process stops when:

- The preset maximum number (50) of epochs is reached; or,
- the changes in the cost function are less than 0.001 among 10 consecutive epochs.

Experimental results of CNN-based sea ice sensing as well as the performance comparison between CNN and NN are presented in Chapter 6.

Chapter 5

Sea Ice Sensing Using Support Vector Machines (SVMs)

First proposed by Cortes and Vapnik in 1995 [101], the support vector machine is now a widely-adopted machine learning algorithm that can solve classification problems and regression problems (with support vector regression, SVR). Among the machine learning approaches, SVMs are fast and effective algorithms with solid theoretical foundations that have exhibited good performance for various remote sensing applications (e.g. sea ice classification, land surface evapotranspiration estimation, and forest mapping) using different platforms [102]–[107]. It has been shown in [103] that SVMs are able to produce better accuracy than other widely used pattern recognition models (such as maximum likelihood and NN classifiers). In addition, SVMs are believed to be robust even when the number of training data is limited [102]. However, unlike deep learning algorithms, SVM cannot automatically learn what features are useful. Furthermore, there is a lack of information about how SVM algorithm can be

applied to sea ice detection using DDMs. Therefore, the objective of this chapter is to develop the methodology of detecting sea ice using SVM classification algorithms and for estimating SIC using SVR from the TDS-1 DDM data.

5.1 Feature Selection From DDMs

In spite of the effectiveness of SVMs at classification, they cannot extract features from data [102]. However, feature selection (FS) helps reduce data dimensions so that SVMs can focus on the variables of significance [108]. As such, FS is integrated into the application of SVM here.

Before implementing feature selection from DDMs, each DDM frame is subtracted by its noise floor and normalized with respect to its maximum (more detailed procedures can be found in Section 2.2). Subsequently, the sample mean value along the delay-axis at each Doppler bin (20 in total) is computed, for which each element indicates the scattering power received from its corresponding spatial cluster (see Fig. 5.1 for demonstration). Afterwards, any negative values (which are due to pixels below the noise floor) are regarded as noise, and for this reason, are set to 0. Next, this array is normalized by its maximum and is adopted as the feature of a DDM for this work. See Fig. 5.2 for the features for DDMs of sea ice (with non-zero SICs) and seawater (with SIC of zero). All extracted features show strong scattering around the 11th bin, which corresponds to the specular point reflection. However, the one for the DDM of seawater exhibits more spreading over all the Doppler bins than those for DDMs of sea ice. This is due to different roughness of sea ice and seawater surfaces [66], [73], [77]. Thereby, the selected feature of each DDM will be regarded as the

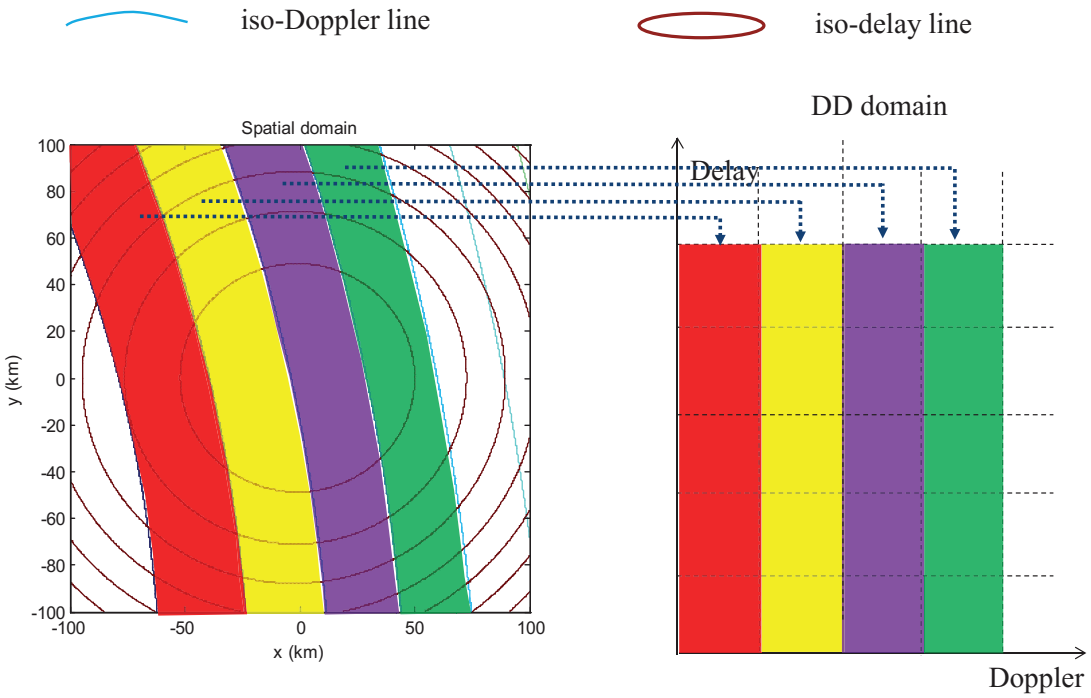

Figure 5.1: The association between the spatial coverage and the Doppler bin.

input to the SVM, and its associated category (seawater/sea ice) determined through ground-truth data will be retained as output.

5.2 SVM for Sea Ice Detection

As a powerful learning method, support vector machines are designed for classification tasks by finding the hyperplane that maximizes the margin (separation) between different classes. Since the selected features for DDMs of seawater differ from those for DDMs of sea ice, the SVM is thus applied here for classifying those two types of DDM data.

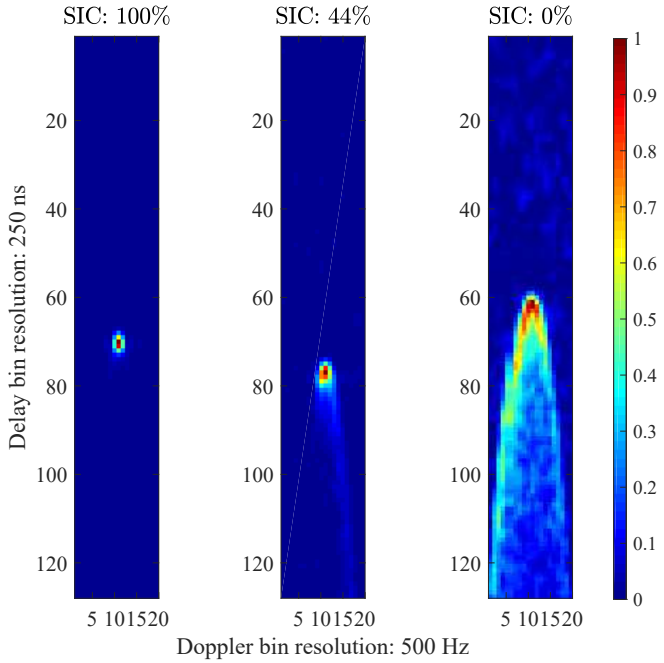

(a)

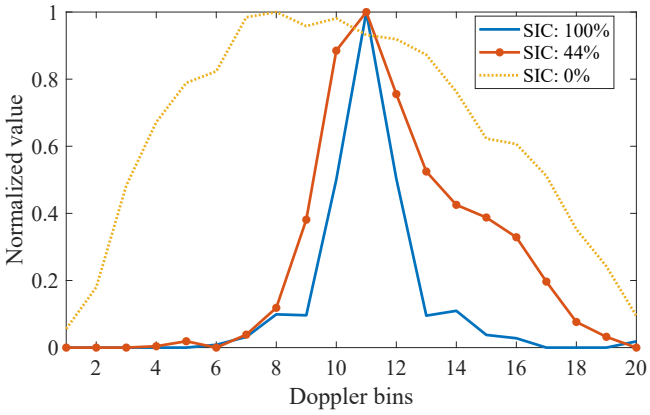

(b)

Figure 5.2: Examples of extracted features: (a) Normalized DDMs collected over regions of different SICs (100%, 44%, and 0%, respectively), and (b) the corresponding selected feature from DDMs as function of Doppler bin.

Given the training set $\{(\mathbf{x}_1, y_1), ..., (\mathbf{x}_n, y_n)\}$, where n is the number of DDM samples for training, $\mathbf{x}_j$ is input sample (selected features from DDMs), for $j = 1, ..., n$, and class labels (seawater/sea ice) for DDMs $y_j \in \{-1, 1\}$, the SVM method aims at solving the following optimization problem:

$$\min_{\mathbf{w},b,\xi} \left(\frac{1}{2}\|\mathbf{w}\|^2 + C \sum_j \xi_j \right) \tag{5.1}$$

subject to

$$\begin{cases} y_j \left[\mathbf{w}\varphi(\mathbf{x}_j) + b\right] \geq 1 - \xi_j \\ \xi_j \geq 0 \end{cases} \tag{5.2}$$

where φ is a mapping function, $\mathbf{w}$ is the weight of $\varphi(\mathbf{x}_j)$, C is the penalty parameter (that is determined by the user), ξ_j is the slack variable, which indicates the allowance for permitted errors, and b is the bias term. The aforementioned problem can be solved by considering its dual form and introducing Lagrange multipliers $\boldsymbol{\alpha} = \{\alpha_1, ..., \alpha_n\}$ [107]

$$\max_{\boldsymbol{\alpha}} \left(\sum_j \alpha_j - \frac{1}{2} \sum_j \sum_k \alpha_j \alpha_k y_j y_k \varphi(\mathbf{x}_j)^T \varphi(\mathbf{x}_k) \right) \tag{5.3}$$

s.t.

$$0 \leq \alpha_j \leq C, \text{ and } \sum_j \alpha_j y_j = 0. \tag{5.4}$$

The term $\varphi(\mathbf{x}_j)^T \varphi(\mathbf{x}_k)$ in Eq. (5.3) is the so-called kernel function K

$$K = \varphi(\mathbf{x}_j)^T \varphi(\mathbf{x}_k), \tag{5.5}$$

which has some optional forms [109] e.g. linear kernel, polynomial kernel, radial basis function (RBF), and sigmoid kernel. Through trial and error, the linear kernel

demonstrated excellent performance (with the best accuracy and the least complexity/tuning parameters), and thus is adopted here, which is given by

$$K(\mathbf{x}_j, \mathbf{x}_k) = \mathbf{x}_j^T \mathbf{x}_k. \tag{5.6}$$

After solving $\boldsymbol{\alpha}$ and b from Eq. (5.3), the classifier can be expressed as

$$f(\mathbf{x}) = \text{sgn}\left(\sum_j \alpha_j y_j \mathbf{x}^T \mathbf{x}_j + b\right). \tag{5.7}$$

5.3 SVR for SIC Estimation

Sticking to the structural risk minimization framework [110], SVR has excellent generalization capability. From Fig. 5.2, the features of DDMs vary corresponding to different SICs; the SVR is thus applied here to obtain a relationship between DDM features and the SIC ground-truth.

Similarly, given the training set $\{(\mathbf{x}_1, y_1), ..., (\mathbf{x}_n, y_n)\}$ with n DDM samples, with $\mathbf{x}_j$ as feature vectors, for $j = 1, ..., n$, and associated SIC values for DDMs $y_j \in [0, 1]$, the SVR method aims at solving the following optimization problem:

$$\min_{\mathbf{w},b,\xi} \left(\frac{1}{2}\|\mathbf{w}\|^2 + C\sum_j (\xi_j + \xi_j^*)\right) \tag{5.8}$$

subject to

$$\begin{cases} y_j - [\mathbf{w}\varphi(\mathbf{x}_j) + b] \leq \epsilon + \xi_j \\ [\mathbf{w}\varphi(\mathbf{x}_j) + b] - y_j \leq \epsilon + \xi_j^* \\ \xi_j, \xi_j^* \geq 0 \end{cases}, \tag{5.9}$$

where φ is a mapping function, $\mathbf{w}$ is the weight of $\varphi(\mathbf{x}_j)$, C is the regularization parameter, ξ_j and ξ_j^* represent the SIC estimation errors that exceed the value of ϵ

(allowance for errors), and b is the bias term. The aforementioned problem can be solved by introducing Lagrange multipliers $\boldsymbol{\alpha} = \{\alpha_1, ..., \alpha_n\}$ and $\boldsymbol{\alpha^*} = \{\alpha_1^*, ..., \alpha_n^*\}$ and considering its dual form [111]

$$\max_{\boldsymbol{\alpha}, b} \left(\begin{array}{l} -\frac{1}{2} \sum_j \sum_k (\alpha_j - \alpha_j^*)(\alpha_k - \alpha_k^*) \varphi(\mathbf{x}_j)^T \varphi(\mathbf{x}_k) \\ + \sum_j y_j (\alpha_j - \alpha_j^*) - \epsilon \sum_j (\alpha_j + \alpha_j^*) \end{array} \right) \tag{5.10}$$

$$\text{s.t. } 0 \leq \alpha_j, \alpha_j^* \leq C, \text{ and } \sum_j (\alpha_j - \alpha_j^*) = 0. \tag{5.11}$$

Through experiments, the RBF demonstrated excellent accuracy, and thus is adopted here, which is given by

$$K(\mathbf{x}_j, \mathbf{x}_k) = \exp(-\gamma ||\mathbf{x}_j - \mathbf{x}_k||^2), \tag{5.12}$$

where γ is the kernel width.

After solving $\boldsymbol{\alpha}$, $\boldsymbol{\alpha}^*$ and b from Eq. (5.10), the formulation for SIC estimation can be given as

$$f(\mathbf{x}) = \sum_j (\alpha_j - \alpha_j^*) K(\mathbf{x}_j, \mathbf{x}) + b. \tag{5.13}$$

The training and test results along with performance evaluation are presented in the following chapter, where the effectiveness of the proposed FS is also illustrated.

Chapter 6

Sea Ice Detection and Sea Ice Concentration (SIC) Estimation Results and Comparison

In this chapter, results of sea ice detection and SIC estimation obtained using the methods described in Chapters 2–5 are evaluated and compared.

6.1 Data Description

6.1.1 Spaceborne GNSS-R DDM Data

DDM data collected in five periods 03-05 (RD 17), 11-13 (RD 18) and 19-21 (RD 19) in February, 15-17 (RD 23) in March and 16-18 (RD 27) in April, 2015 around the Arctic regions by the UK TDS-1 (available on `www.merrbys.co.uk`) are employed in this study. The employed DDM data are listed in Table 6.1. Details of the TDS-1

DDM data can be found in [24] and [29]. The DDM metadata also provides the specular point position for each DDM. Here, the SP is regarded as the location of a DDM. Such information can be utilized to extract the collocated SIC from the reference data that is described in the next subsection. In addition, the SNR at the peak power point is also available and employed for data quality control.

Examples of the GNSS-R DDMs collected by TDS-1 over the regions with different SIC values (0%, 50% and 92%, respectively) are shown in Fig. 3.1. The SIC values were obtained from the reference data for the corresponding SP position of each DDM. From Fig. 3.1, the differences among DDMs over varying surface conditions are obvious. As the SIC values increase, the associated DDMs become less spread. It should be noted that the resolutions for delay and Doppler bins are 250 ns and 500 Hz, respectively. The process of noise floor subtraction mentioned in Section 2.2 is a typical technique to deal with thermal noise. Speckle noise can be mitigated through incoherent processing of GNSS-R signals. It is worth mentioning that TDS-1 DDMs have already been processed with 1-s (1000 looks) incoherent summation. The speckle noise can be further reduced by the proposed adaptive incoherent summation of the DDMs described in Section 2.2. However, the incoherent summation process will reduce the spatial resolution. In order to preserve the maximal achievable spatial resolution of TDS-1 DDM, no further incoherent summation is applied in this work.

6.1.2 Ground-truth Data

The reference sea ice concentration data employed in this thesis are derived from that collected by multiple sensors: the Scanning Multichannel Microwave Radiometer

Table 6.1: Data Employed in this Work.

	Training			Testing								
ID	RD 17			RD 18		RD 19		RD 23		RD 27		
Period (in 2015)	Feb. 03 to 05			Feb. 11 to 13		Feb. 19 to 21		Mar. 15 to 17		Apr. 16 to 18		
Track ID	0014	0021	0024	0000	0007	0021	0036	0020		0043	0053	
	0026	0027	0051	0008	0012	0096	0098	0025		0109	0193	
	0062	0064	0108	0016	0051	0135	0137	0074		0194	0198	
	0113	0119	0158	0060	0062	0142	0147	0076		0293	0294	
	0159	0163	0167	0128	0134	0179	0212	0118		0297	0300	
	0169	0194	0202	0164	0169	0217	0221	0119		0340	0343	
	0203	0213	0256	0170	0180	0263	0268	0153		0387	0397	
	0260	0261	0301	0245	0288	0269	0270	0156		0399	0440	
	0305	0341	0344	0290	0296	0302	0315	0162		0444	0445	
	0345	0370	0372	0297	0339	0316	0317	0237		0479	0484	
	0385	0389	0435	0346	0350	0353	0497	0241		0488	0543	
	0444	0478	0480	0355	0389	0571	0578	0244		0546	0576	
	0482	0517	0521	0395	0405	0584	0586	0285		0580	0581	
	0528	0603	0606	0406	0455	0622	0625	0293		0585	0619	
	0612	0615	0616	0457	0460	0659	0661	0326		0628	0630	
	0617	0618	0653	0505	0506	0666	0710	0337		0662	0666	
	0654	0655	0695	0551	0552	0745	0747	0338		0668	0731	
	0700	0725	0732	0555	0615	0750	0751	0339		0736	0741	
	0736	0766	0767	0646	0651	0754	0789	0378		0892	0940	
	0773	0830	0873	0652	0657	0793	0832	0423		0993	0996	
	0885	0931	0934	0659	0681	0839	0888	0427		0998	1001	
	0935	0966	0974	0682	0691	0891	0897	0428		1003	1040	
	0986	0988	1035	0692	0730	0932	0933	0457		1049	1086	
	1038	1039	1040	0770	0771	0945	0975	0462		1090	1092	
	1073	1077	1078	0774	0805	0981	0993	0463		1131	1226	
	1081	1116	1121	0806	0815	1044	1120	0467		1230	1269	
	1125	1126	1127	0863	0865	1129	1211	0547		1276	1314	
	1130	1168	1173	0869	0871	1240	1245	0548		1317	1320	
	1178	1179	1217	0873	0904	1246	1250	0555		1358	1361	
	1222			0911	0912	1252		0684		1364	1367	

(SMMR, carried aboard Nimbus-7), the Special Sensor Microwave/Imagers (SSM/Is) on the Defense Meteorological Satellite Program (DMSP) -F8, -F11 and -F13 satellites, and the Special Sensor Microwave Imager/Sounder (SSMIS) on the DMSP-F17 satellite [112]. The reference data provide daily and monthly averaged SIC for both the northern and southern hemispheres with different spatial coverage and have been valuable sources for global sea ice studies. The work here focuses on SIC analysis in the northern hemisphere. The corresponding data are stored as images each with a size of 448 rows $\times$ 304 columns. In addition, the resolution for each grid is about 25 $\times$ 25 km^2. The data values range from 0 to 255, in which [0, 250] represent valid SIC values and the rest indicates land information or missing data. For better illustrations, the SIC value is multiplied by 0.4 (which thus falls in [0, 100] in percentage) and the original data with value greater than 250 are set as -40. An example of the rescaled data on February 04, 2015 for the north hemisphere is shown in Fig. 6.1.

6.2 Data Quality Control and Modification

In this work, DDM samples with SNR (at the peak power point) lower than 0 dB (which means the peak power value is even below the noise level) were rejected. To minimize the effect of scattering off land, the DDMs with SPs over land and near coastal lines (within 50 km) were manually filtered out as well.

It should be noted that the coverage area corresponding to the DDM signal box is about 125 $\times$ 125 km^2 while the grid size is of 25 $\times$ 25 km^2 for the original SIC reference data. In order to match the coverage area of the DDM signal box, every SIC value in the original reference data was averaged by its surrounding 5 $\times$ 5 grid

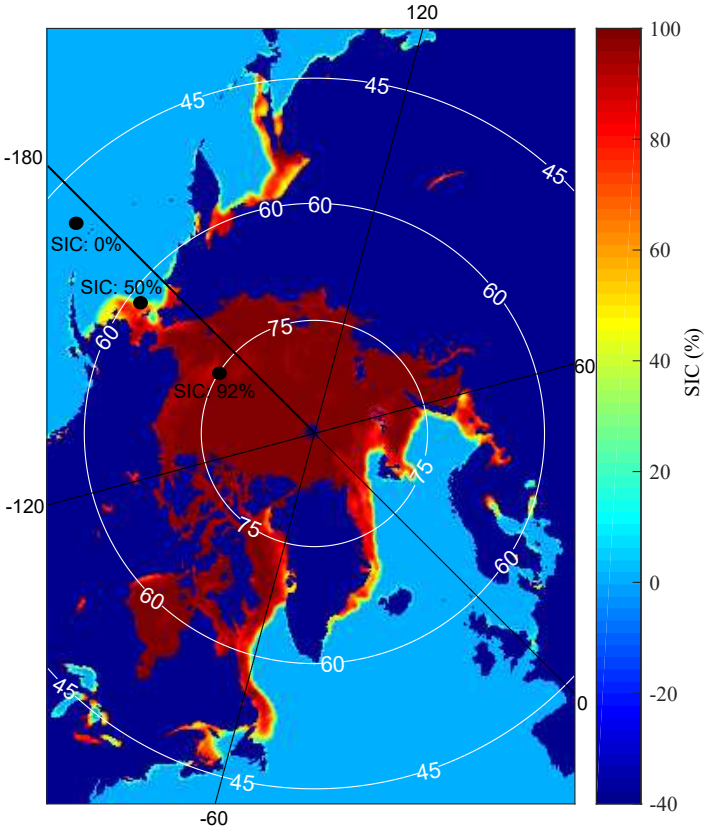

Figure 6.1: An example of the daily SIC on February 04, 2015 for the north hemisphere modified from [112]. The SIC value is from 0 to 100 (%). The land and the region without data is marked by dark blue (with a value of -40) for illustration purposes. White circles and black straight lines represent the latitudes and longitudes (in degree), respectively. The black circular areas (with a radius of about 100 km) indicate the approximate glistening zones of the DDMs.

values. Specifically, each grid with a valid SIC value (from 0 to 100) was averaged by those (also valid) within its surrounding 5×5 grids.

After the averaging, the associated SIC value was automatically extracted by matching the latitude and longitude of DDM SP with the coordinate grid of the reference data, and normalized to 1. For ice detection application, a threshold of 0.15 used in [113] is applied to the extracted SIC data. A data grid with a SIC value greater than 0.15 will be regarded as "ice-covered" and assigned with 1, otherwise, 0.

6.3 Training Data

The training for the proposed methods was implemented using the TDS-1 data collected from February 03 to 05, 2015, which were labeled as RD 17. The processed DDM data were regarded as inputs and associated ice data from SMMR and DMSP SSM/I-SSMIS Passive Microwave sensors were treated as desired output. The number of training patterns was 8377.

6.3.1 Observable-based Sea Ice Detection

The training data are employed to derive the thresholds for DDM observables to detect sea ice. For this dataset, DDMs associated with sea ice were sorted according to ground-truth ice distribution data. First, an empirical value of DDM_{thres} needs to be determined. It was found that a DDM_{thres} ranging from 0.19 to 0.57 produced similar accuracy [114]. Thus, the DDM_{thres} was arbitrarily selected within this scope, as 0.40. As discussed in Section 2.1, observables derived from the DDMs of sea ice are expected to be smaller than those for seawater, which is also demonstrated by the

differences between sample probability density functions (PDFs) of the observables for sea ice and seawater (see Fig. 6.2). For each observable, the threshold can be determined as the intersection of its corresponding PDF. Through experiments, it was found that the performance of the proposed observables are quite similar [66]. Without loss of generality, the Pixel Number Observable is hereafter employed as a representative for observable-based methods.

6.3.2 NN-based Sea Ice Sensing

Three input schemes, i.e., cropped DDM, full DDM, and FS, are tested. The training set containing the inputs and the corresponding target outputs of surface type and SIC value is presented in Fig. 6.3. It should be mentioned that each vertical slice (with 2560, 800, and 20 elements for full DDM, cropped DDM, and FS, respectively) in Fig. 6.3(a)–(c) is one input vector and the horizontal axis denotes the sample sequence. The corresponding target ice detection outcome and SIC value are presented as Fig. 6.3(d) and (e). As shown in Fig. 6.3(a)–(c), some of the vertical slices are more spread and they usually correspond to low values in reference SIC data. Typically, such slices are extracted from DDMs of seawater as these DDMs are usually more spread compared with the DDMs of sea ice (also see Fig. 3.1). A DDM collected over a fully (or almost fully) ice-covered region is usually associated with a mirror-like reflection from a nearly flat surface. As a result, only the region immediately around the SP is able to redirect the incoming signals towards the receiver. Correspondingly, the DDM (see Fig. 3.1(c)) appears similar to the clean Woodward Ambiguity Function (WAF). As has been found in [73], the more the DDM resembles a WAF, the more coherent

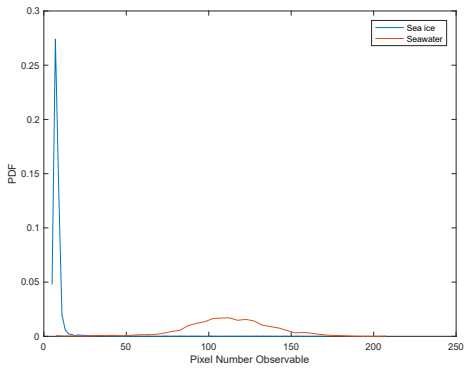

(a)

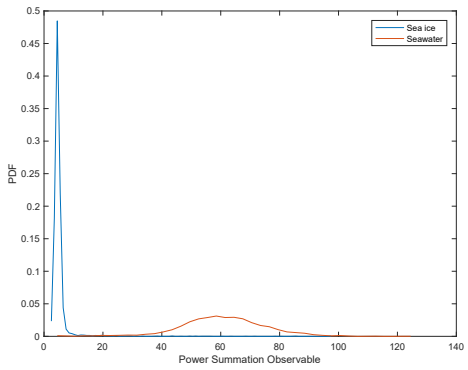

(b)

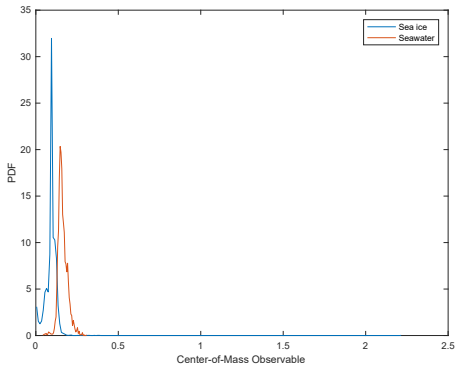

(c)

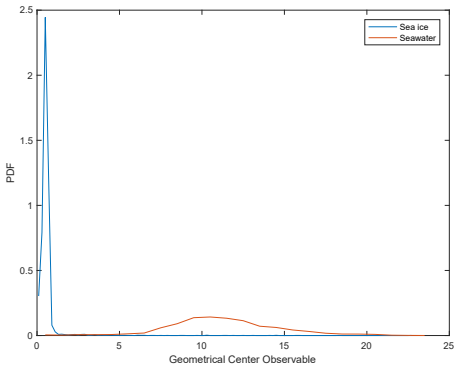

(d)

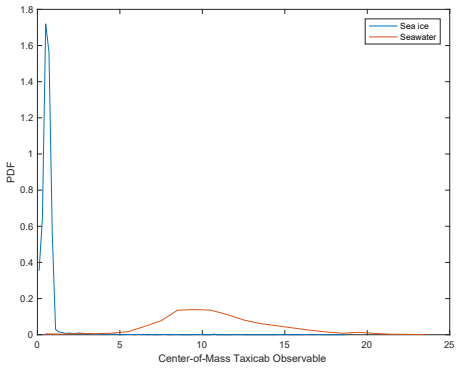

(e)

Figure 6.2: Sample PDF of observables: (a) Pixel Number, (b) Power Summation, (c) Center-of-Mass, (d) Geometrical Center, and (e) Center-of-Mass Taxicab for sea ice and seawater.

the scattering is, and the possibility of a flat ice surface being involved is higher. Instead, roughness of open oceans can vary considerably, but can still be assumed to be rougher than ice [66]. Therefore, non-specular regions of the ocean corresponding to delay-Doppler offsets are more likely to reflect a GNSS signal towards the receiver, causing a DDM of open ocean (refer to Fig. 3.1(a)) to be more spread than the DDM of sea ice. Furthermore, in the marginal ice zone air-sea interaction is suppressed compared with open ocean conditions [115]. Consequently, the ice-covered surface will still appear smoother than open oceans given the same wind condition. Thus, the DDM over a partially ice-covered area looks more spread than that of a fully ice-covered area but less spread than that of the open ocean. In summary, a spread DDM will be associated with low SIC, and vice versa. It is obvious that the proposed method relies on the extent of spread in DDMs, which mainly varies with surface roughness that is dependent on SIC. By presenting the input DDM data along with desired SIC output, the NN for SIC retrieval was developed accordingly.

The impact of the number of neurons on the detection accuracy is evaluated with a range of [1, 10]. As noted in subsection 3.3.1, the number of neurons was set as 3 in the hidden layer, which generated satisfactory results. This is illustrated by the accuracy presented in Fig. 6.4 resulting from full DDM inputs.

6.3.3 CNN-based Sea Ice Sensing

Two input schemes that employ a full DDM and a cropped DDM, respectively, are investigated for CNNs. Instead of reshaping a DDM into an 1-D vector format used as input to an NN, the original 2-D format is retained. Some examples of input DDMs

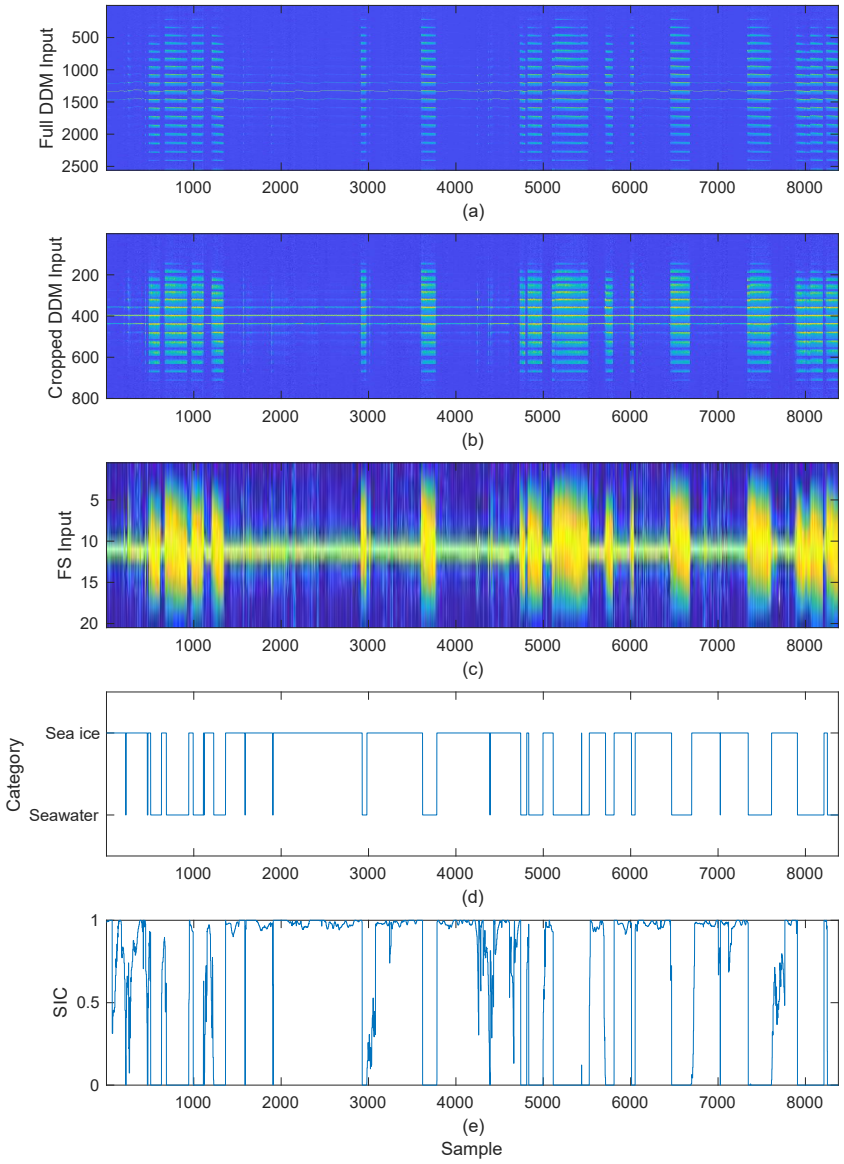

Figure 6.3: Training set for NNs: (a) Full DDM input, (b) cropped input, (c) FS input, (d) target labels, and (e) target SICs.

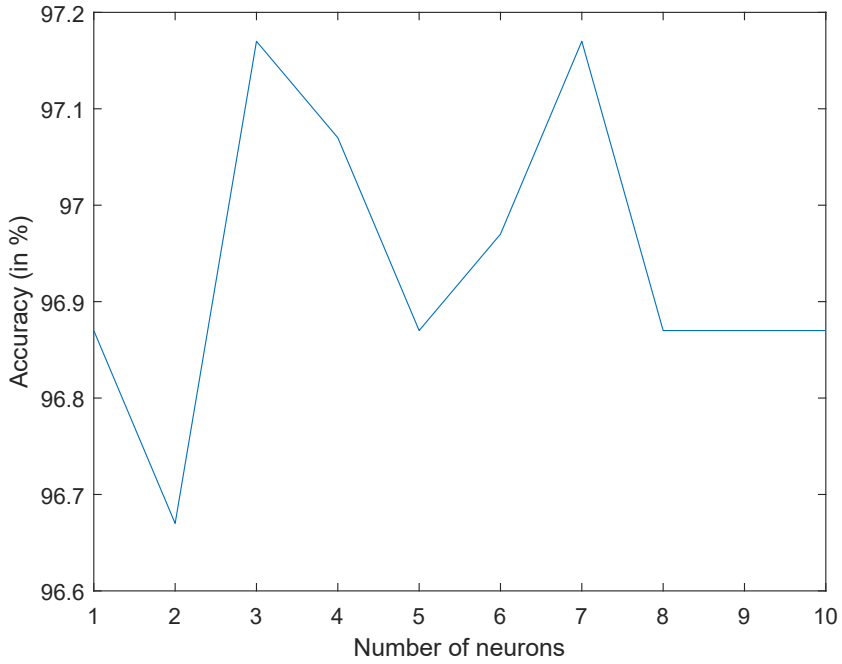

Figure 6.4: Detection accuracy of NN in terms of different numbers of neurons.

can be found in Fig. 4.2, and the sizes of each input are 128-by-20 and 40-by-20 pixels for full and cropped DDMs, respectively. A complete set of target data for training are displayed in Fig. 6.3(d)–(e).

The impact of selection of structural parameters, specifically, the size and number of filters in the convolutional layer and the mini-batch size, for the devised CNN architecture is assessed. The search range for both the size and number of filters is from 1 to 9 with a step size of 1, and that of mini-batch size is set by $\{32, 64, 96, 128\}$. The sea ice detection accuracy of the training set with different combinations of structural parameters is shown in Fig. 6.5. It is evident that the selection of structural parameters has negligible effect on the accuracy (the difference is less than 0.002), and thus it can be arbitrary.

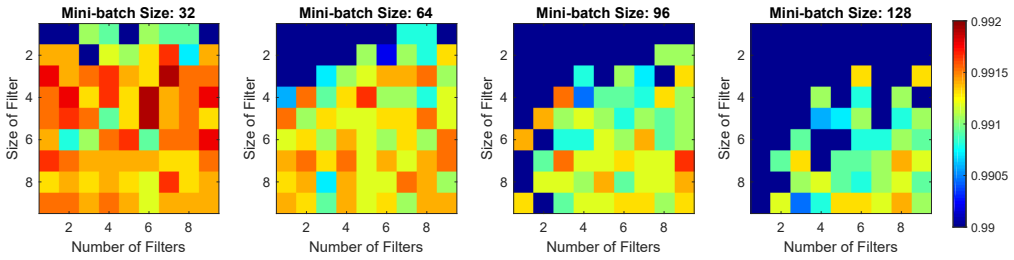

Figure 6.5: The accuracy of CNN-based sea ice detection using scanning parameters.

6.3.4 SVM-based Sea Ice Sensing

The FS is adopted as input for the SVM application. The training samples are presented in Fig. 6.3(c)–(e). Note that the size of FS input is 20.

The penalty parameter C of a SVM model (see Eqs. 5.1 and 5.2) determines the generalization capability of the classifier [109], and it needs to be properly tuned (the only parameter that needs specification in the sea ice detection task). Accordingly, the search for C was conducted at an incremental factor of 10 for $C \in \left[10^{-5}, 10^{2}\right]$. The accuracy (number of correct results over total sample length) of this proposed method using varying C for each data set is displayed in Fig. 6.6. The improvement of average accuracy became negligible when $C \geq 10^{-3}$, hence C was arbitrarily selected within this range, as 1.

Similarly, SVR also requires a tuning of parameters, specifically, the regularization parameter C, error allowance ϵ, and the kernel width γ, whose searching ranges were set as $C \in \{10^{-5}, 10^{-4}, ..., 10^{2}\}$, $\epsilon \in \{10^{-5}, 10^{-4}, ..., 10^{0}\}$, and $\gamma \in \{1, 2, ..., 5\}$, respectively. The correlation coefficients (r) obtained between the estimated and ground-truth SICs with scanning parameters are shown in Fig. 6.7. With $C = 1$, $\epsilon = 0.01$, and $\gamma = 3$, r reached its maximum, and thus, this set was retained for SIC

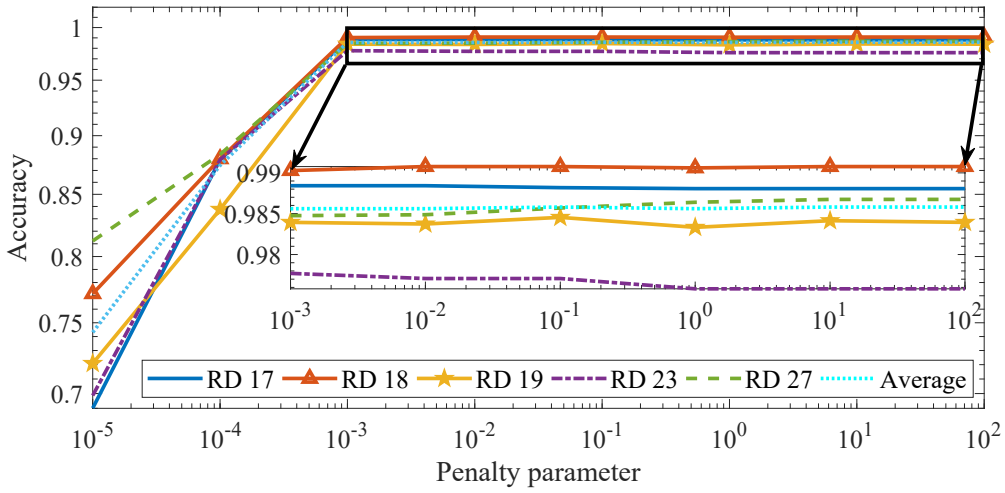

Figure 6.6: Accuracy of the proposed SVM using various C. The zoomed in picture (i.e. black box) is for the range of $C \in \left[10^{-3}, 10^{2}\right]$. RD 17 is the training set and RDs 18, 19, 23, and 27 are test sets.

estimation. It is evident that when the allowed error ϵ reached 1 (the same as the highest SIC value), the SVR could not provide any reliable prediction because the values of r were around 0.

6.4 Test Results and Comparison

The proposed methods for ice detection and concentration estimation are assessed with data during another four collection periods (February 11-13 and 19-21, March 15-17 and April 16-18, 2015 and they were denoted as RD 18, RD 19, RD 23, and RD 27, respectively). Specifically, for sea ice detection application, results of the observable-based, the NN-based with FS, full, and cropped DDMs, the CNN-based with full and cropped inputs, and the SVM-based with FS are evaluated and compared

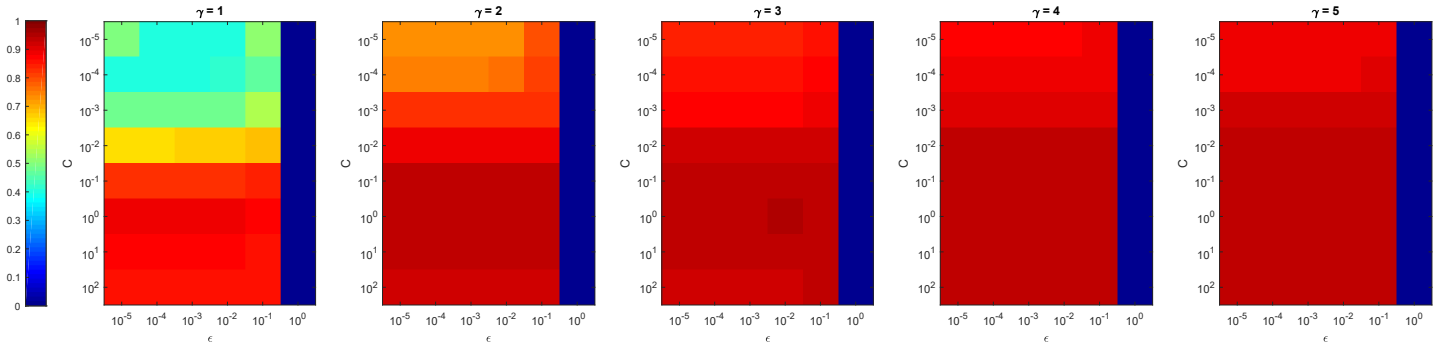

Figure 6.7: Training SVR with various combinations of C, ϵ and γ for r between ground-truth and prediction. The maximum of r was found when $C = 1$, $\epsilon = 0.01$ and $\gamma = 3$.

Table 6.2: Accuracy of Ice Detection

ID	Observable	Full-size input		Cropped input		FS	
		CNN	NN	CNN	NN	NN	SVM
RD 17 (training)	97.96%	99.15%	99.60%	99.03%	99.13%	98.95%	98.81%
RD 18 (test)	98.17%	98.12%	97.94%	98.94%	99.01%	98.63%	99.06%
RD 19 (test)	96.58%	97.97%	97.29%	98.77%	98.54%	98.21%	98.33%
RD 23 (test)	97.67%	96.42%	93.98%	98.41%	98.04%	97.00%	97.58%
RD 27 (test)	98.10%	97.04%	95.97%	98.43%	98.41%	97.78%	98.64%
Average	97.78%	97.83%	97.17%	98.73%	98.67%	98.18%	98.56%

using the same datasets. Except for the observable-based approach, the other methods are also employed for SIC estimation.

The sea ice detection accuracy results are tabulated in Table 6.2. The overall prediction of surface type along with the ground truth are presented in Fig. 6.8. Good accuracy ranging from 97.17% to 98.73% is obtained for sea ice detection using the proposed methods.

To assess the SIC estimation, taking NN-based SIC results (SIC_{nn}) as an example, SIC_{nn} is compared with the same-day reference SIC data (SIC_{ref}). The standard deviation error E_{std} and the correlation coefficient r between SIC_{nn} and SIC_{ref} are employed for evaluation purposes and are defined as

$$\begin{aligned} E_{std} &= \mathrm{std}(SIC_{nn} - SIC_{ref}) \\ r &= \frac{cov(SIC_{nn}, SIC_{ref})}{\mathrm{std}(SIC_{nn})\mathrm{std}(SIC_{ref})} \end{aligned} . \tag{6.1}$$

The (normalized) error statistics for SIC estimation are also shown in Table 6.3, from which low discrepancy between estimated SIC and SIC_{ref} may be observed for these

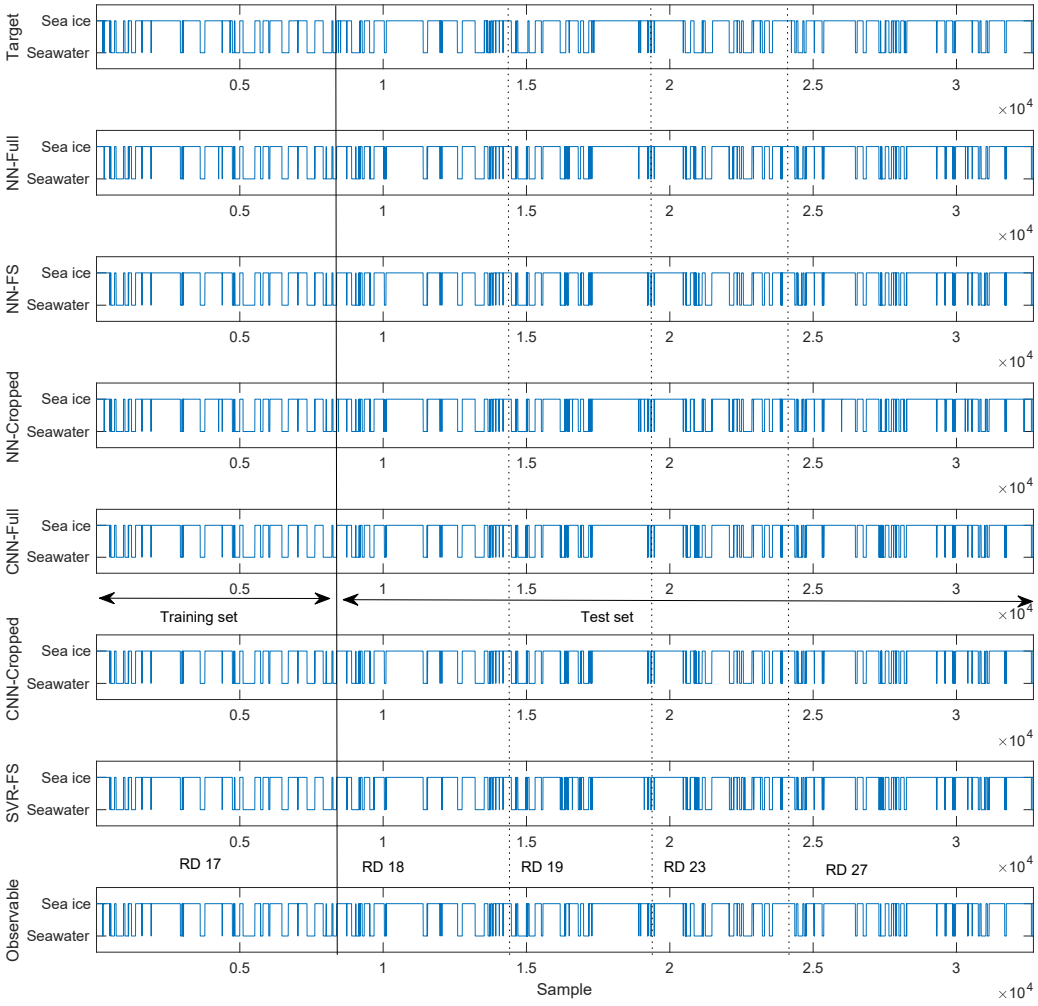

Figure 6.8: Outcomes of sea ice detection using proposed methods. Training and test sets are separated by a solid line. The target data represents the ground-truth data.

Table 6.3: Error Statistics for SIC Estimation Using Different Input Sizes

ID	Full-size input				Cropped input				FS			
	E_{std}		r		E_{std}		r		E_{std}		r	
	CNN	NN	CNN	NN	CNN	NN	CNN	NN	NN	SVR	NN	SVR
RD 17 (training)	0.15	0.11	0.95	0.97	0.15	0.11	0.95	0.97	0.13	0.12	0.96	0.97
RD 18 (test)	0.17	0.20	0.91	0.88	0.16	0.17	0.92	0.91	0.17	0.16	0.91	0.92
RD 19 (test)	0.15	0.17	0.93	0.92	0.15	0.16	0.94	0.93	0.16	0.15	0.93	0.94
RD 23 (test)	0.16	0.19	0.93	0.91	0.15	0.13	0.94	0.95	0.15	0.15	0.94	0.95
RD 27 (test)	0.18	0.20	0.89	0.86	0.17	0.18	0.89	0.90	0.17	0.16	0.90	0.90
Average	0.16	0.17	0.92	0.91	0.16	0.15	0.93	0.93	0.1535	0.1467	0.93	0.94

methods. Negligible degradation in test accuracy relative to the training set proves the generalizability of these proposed methods. Furthermore, the estimated SIC is generally in accordance with the reference SIC. The SIC predicted by the proposed methods along with the reference are presented in Fig. 6.9. For illustration, the averaged SIC estimates from the proposed NNs-, CNNs-, and SVMs-based methods are shown in a geographic frame for regions with latitudes higher than 45°N as Fig. 6.10. In addition, the locations without DDM estimates are in white and land areas are in gray.

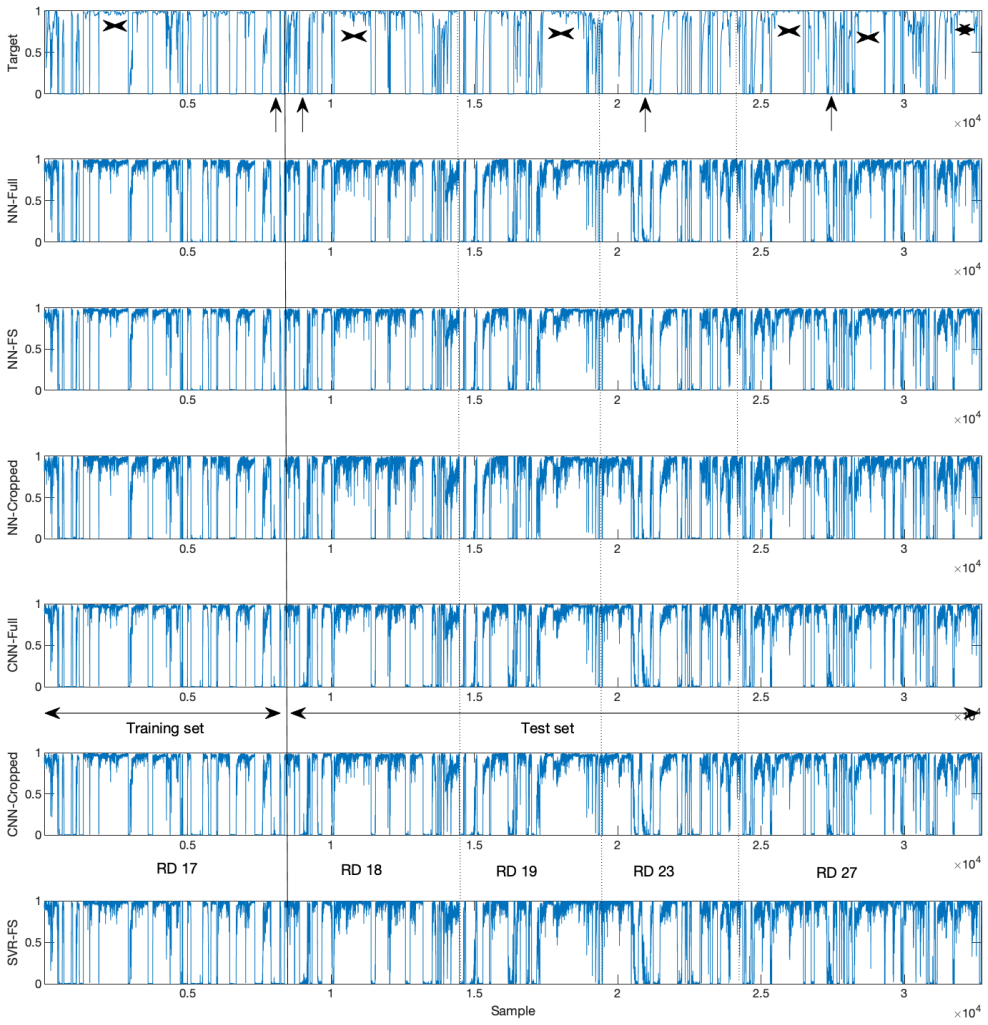

Figure 6.9: SIC estimation using proposed methods. In target (ground-truth) data, DDMs associated with patterns marked by arrows and tagged by cross symbols result in overestimation and underestimation, respectively.

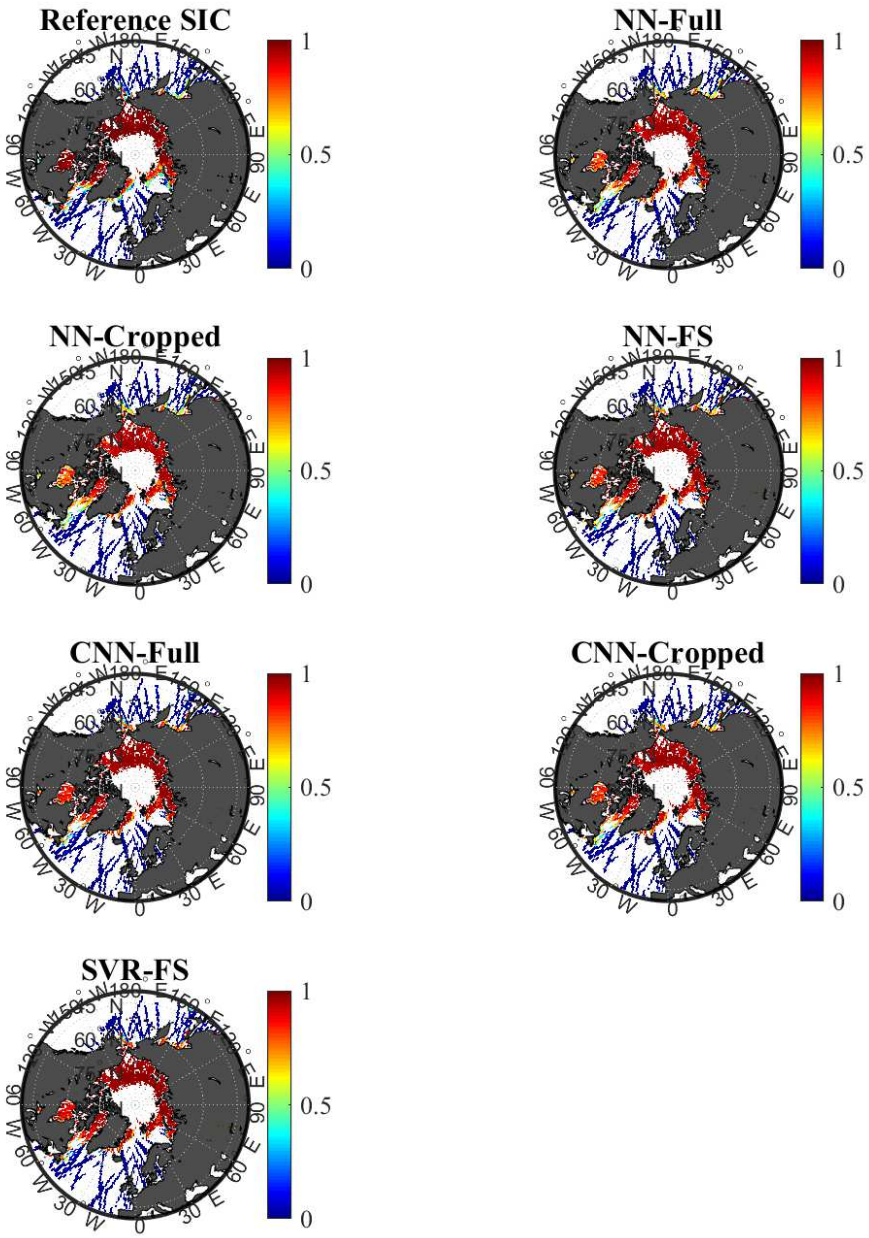

Figure 6.10: Averaged SIC estimation. The locations without DDM estimates are in white and land areas are in gray.

6.4.1 Effect of Low Sea State

Overall good agreement can be observed between the DDM-based SIC estimates and the ground-truth data (see Fig. 6.10). Despite this, some discrepancy can be noted around e.g., (70°N,160°W) and (75°N,30°E), where both sea ice and seawater exist. Such ice-like reflections may be due to very calm water with low wind [66]. In order to further investigate this, the *in situ* measurement data of significant wave height (SWH) and wind speed (WS) from the National Data Buoy Center (NDBC) [116] were used for reference. Due to limited sea state data in the region under investigation, the DDMs collected on July 22, 2015 near (within the distance of 200 km) the NDBC Stations 48012 (70.025°N,166.071°W), 48214 (70.872°N,165.248°W), 48213 (71.502°N,164.133°W) and 48216 (71.502°N, 164.133°W) within the same period were analyzed. The SWH and WS data from the buoy station closest to each selected DDM and at the most immediate instant to the DDM collection time were used. The locations of the buoy stations and the selected DDMs are shown in Fig. 6.11. Furthermore, the SPs with overestimated SIC (15% higher than the reference SIC of value about 0) are indicated by black dots, and those with precise results are depicted by magenta triangles. For concision, this analysis is based on the NN-cropped results. Even so, this effect is observed for all methods. It can be noticed that overestimates mainly appear near the ice edge and this may account for the above-mentioned discrepancy in Fig. 6.10. The estimated and reference SICs as well as the corresponding SWH and WS are shown in Fig. 6.12 in terms of the distance from the associated DDM location to the closest ice edge. A slight sea state can be noticed for all the data analyzed in Fig. 6.12. Moreover, an average overestimation of

66% mainly occurred at the SP locations within 150 km from the ice edge. Otherwise, accurate results with an overall discrepancy of 1% can be obtained. Therefore, it may be inferred that the SIC tend to be overestimated at the regions near ice edges or in partially ice-covered regions when the sea state and wind speed are low (even if it is not low, air-sea interaction is still suppressed). The corresponding overestimated patterns are marked by arrows in Fig. 6.9.

On the other hand, underestimation also existed when the actual SIC was 100%. This might be caused by sea surfaces with ice of thickness exceeding the penetration depth. In this case, the scattering would be dominated by the uppermost sea ice, which could be rougher than the ice-water interface. In addition, if a DDM is contaminated by speckle noise at the non-specular delay-Doppler bins, the SIC could also be underestimated. The cases of underestimation can be observed in Fig. 6.9 as patterns tagged by cross symbols.

6.4.2 NN v.s. CNN

As can be seen from Tables 6.3 and 6.2, the proposed CNN-based sea ice remote sensing shows overall improved accuracy over the proposed NN-based one, especially when using the original input size. It can be noticed that the differences between the results of these methods are quite small. Thus, the standard error (which is the ratio between the standard derivation and the square root of sample size) in the estimates of the statistics is calculated. The standard errors of E_{std} were found to be from 0.0016 to 0.0022 and those for r were of the order of 10^{-4}. Thus the CNN-based method outperforms the NN-based.

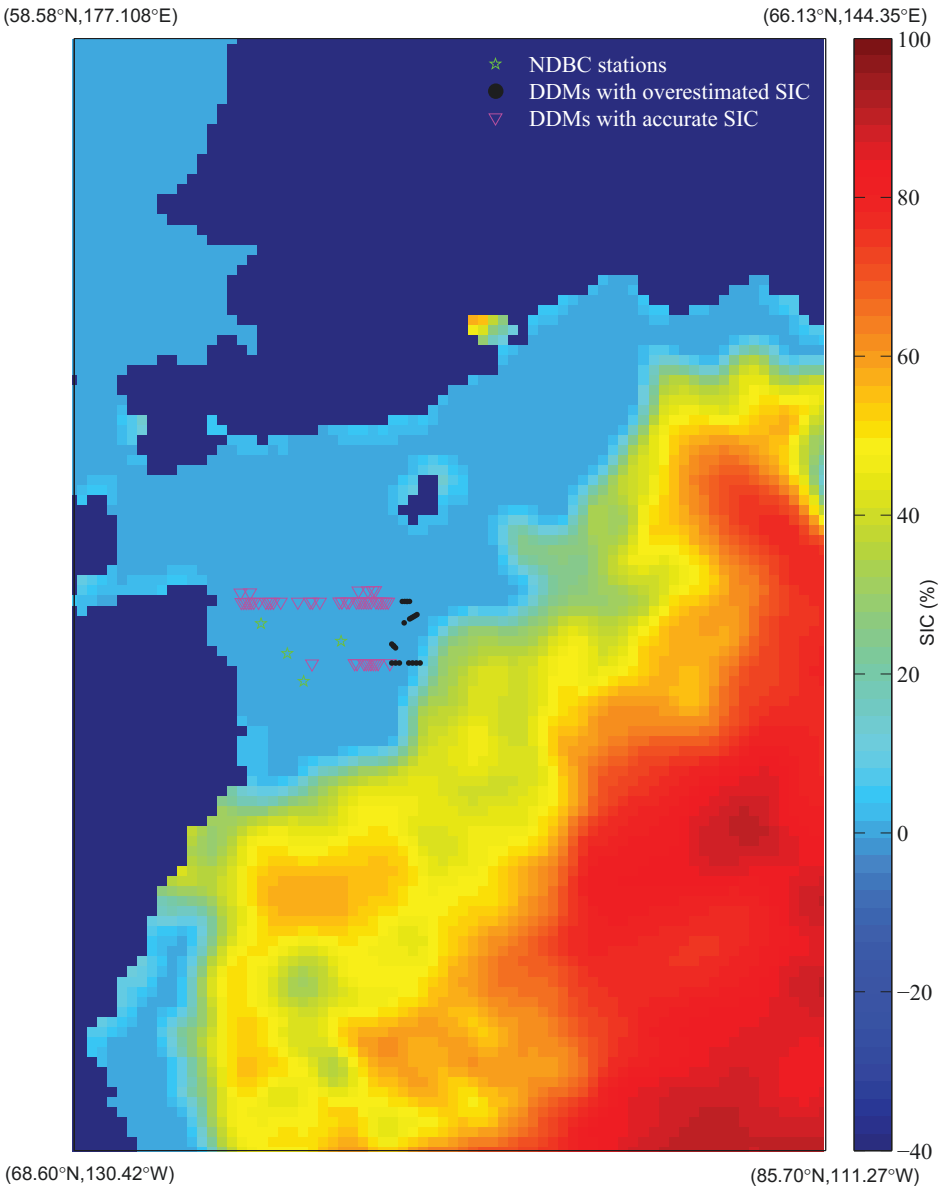

Figure 6.11: Locations of NDBC stations and the SPs of the DDMs used for analyzing the effect of low sea state on SIC estimation. Land areas are indicated by negative values.

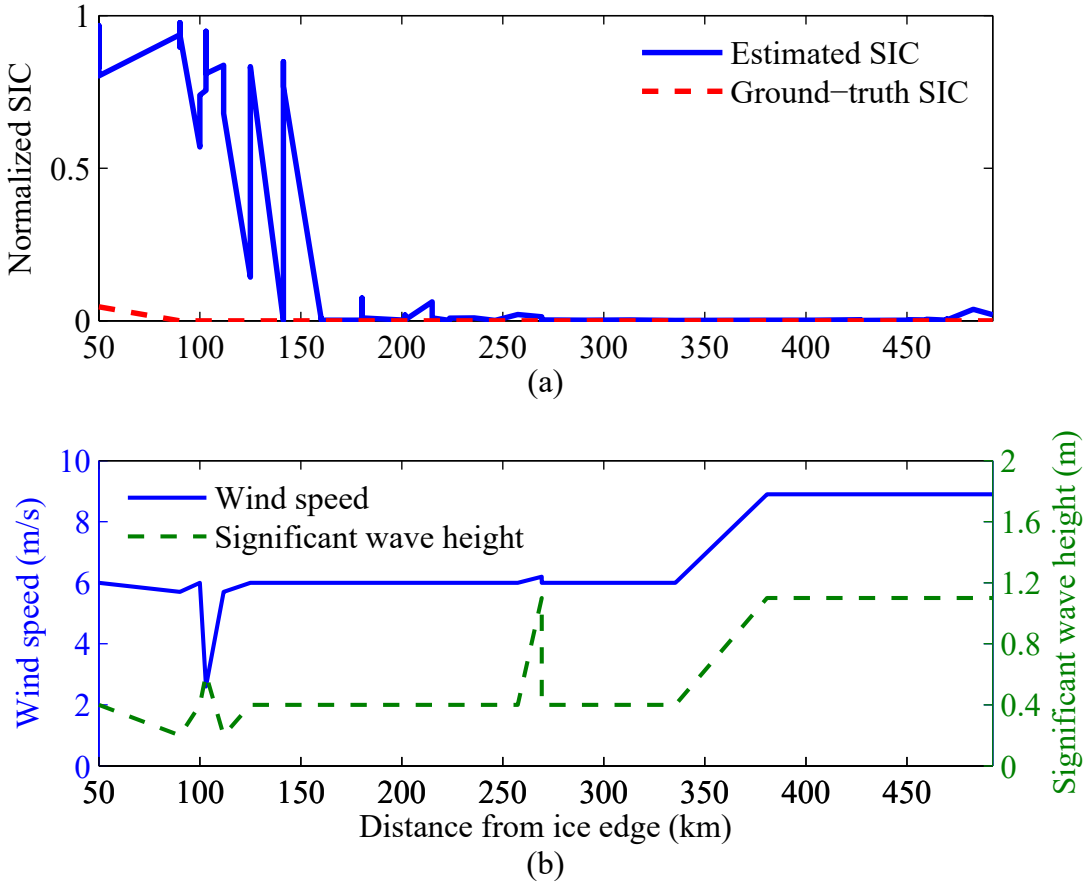

Figure 6.12: Results under low sea state: (a) estimated and reference SICs and (b) significant wave height and wind speed data.

An advantage of the CNN lies in the usage of filters in the convolution layer, which appear to be able to reduce the noise in the DDM. The deployment of the convolution and pooling layers makes a CNN less sensitive to misalignment of DDM specular point within a frame. Note that a pooling layer of size (2, 2) and stride 2 is able to resolve a 1-pixel fluctuation in DDM frames. The resistance to the misalignment of a signal box relies on the depth and size of the convolution and pooling layers. Since only one layer of each was adopted in this work, the ability of the designed CNN to be completely independent from the data locations is quite limited. This also accounts for the varied precision among different datasets since the degree of fluctuation differs (see Fig. 6.13 for the sample probability density distribution of the delay pixel index of DDM SPs in the datasets). In Fig. 6.13, obvious discrepancies can be found between the training set RD 17 and test sets RDs 23 and 27, and this could result in the drop of sea ice sensing accuracy from using cropped data to full-size ones (for both CNN and NN). However, the CNN still outperforms the NN with original DDM format as discussed above and its performance may be further enhanced with more layers. When the data are adequately processed by cropping the DDM for alignment, both CNN and NN can produce good results.

In addition to the advancement in accuracy, the designed CNNs have fewer parameters than NNs for the same task, which makes the training easier [14]. For illustration, the sea ice detection-orientated CNN has 6666 $(= (7\times7+1)\times5+(2315+1)\times 3+(3+1)\times2)$ parameters, while the NN has 7691 $(= (128\times20+1)\times3+(3+1)\times2)$ for full-size input; and those for cropped images are 2046 and 2411, respectively.

In summary, the devised CNN scheme manifests the following advantages over NN: 1) overall improved accuracy, 2) fewer parameters in the network (easier to

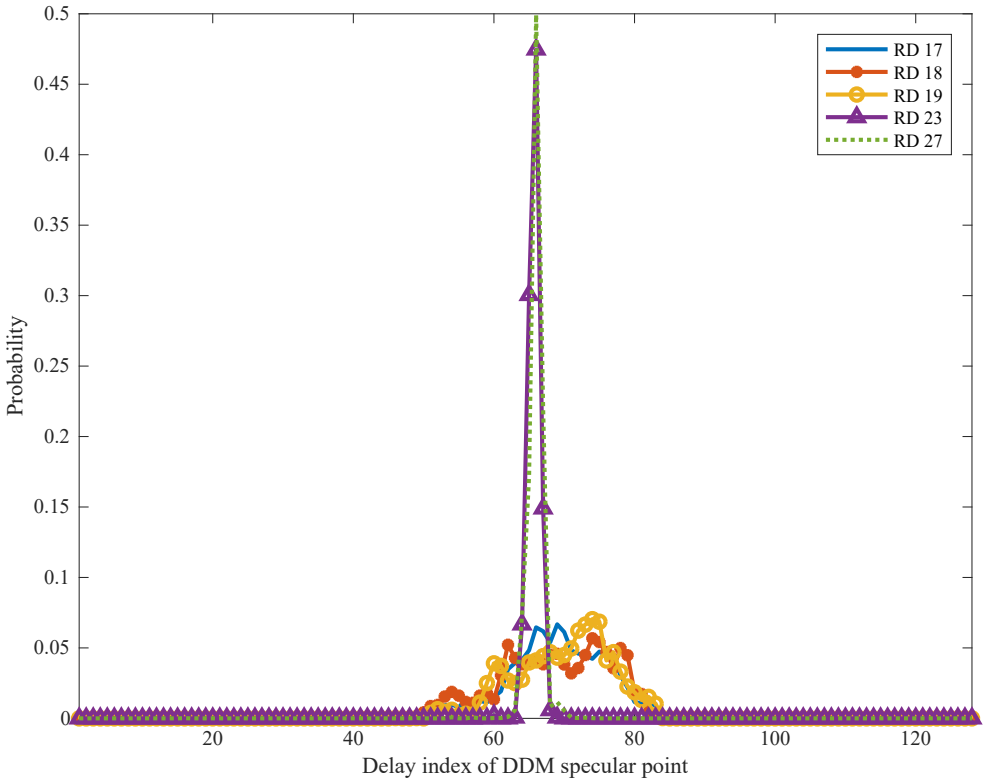

Figure 6.13: Sample probability density distribution of the delay pixel index for DDM specular point for each dataset.

train), and 3) increased tolerance to changes in input data structure (requires less data preprocessing, without need for registering the delay coordinate of the specular point).

6.4.3 NN v.s. SVM

The proposed SVM-FS-based sea ice detection scheme shows better accuracy than the NN- and CNN-based (with full DDM frame as input) methods. Note that the FS is derived from full DDMs rather than cropped ones. By applying the devised FS,

the input size is notably decreased compared with previous methods (from 128×20 to 20). In addition to that, the selected features are less sensitive to noise (owing to an averaging process) than directly inputting DD pixels. As the use of the designed FS seems to be advantageous, it is mandatory to further test FS with the NN-based method for the purposes of 1) verifying the utility and superiority of FS and 2) making an impartial performance comparison between SVM and NN (note that the CNN employs 2-dimensional input, and therefore, it was not examined). The accuracy of the NN-FS method is also given in Table 6.2. The achieved outcome indeed proved both the advantage of FS, since NN-FS outperformed NN, and the improvement of SVM-FS against NN-FS. In addition, the SVM-FS results show that the probabilities of detection and false alarm for sea ice are higher than those for seawater in general (see Table 6.4).

Among NN-full, CNN-full, and NN-FS, NN-FS showed the best performance and it is the closest to that of SVM-FS. Thus, further comparison in terms of false detection was made only between NN-FS and SVM-FS. The analysis of false detection of ice under different sea conditions in terms of wind speed was performed (see Figs. 6.14-6.15). Here, the wind speed data from ERA-Interim [117] were employed as the reference. From Fig. 6.14, it can be seen that the number of false detections using SVM-FS was lower than NN-FS under all sea conditions. Through trial and error, it was found that SVM-FS produced fewer false alarms (25, 22, 47, 44, and 71 for RDs 17, 18, 19, 23, and 27, respectively) than NN-FS (43, 56, 68, 99, and 142 for RDs 17, 18, 19, 23, and 27, respectively). In addition, it should be noted that no false alarms appeared in the SVM-FS method when wind speed was above 10 m/s. From Fig. 6.15, it can be observed that the false alarm rate decreased with increasing wind

Table 6.4: Probabilities of Detection and False Alarm for SVM-FS

	Ice		Seawater	
	Probability Of Detection	Probability Of False Alarm	Probability Of Detection	Probability Of False Alarm
RD 17	98.70%	0.96%	99.04%	1.30%
RD 18	99.25%	1.59%	98.41%	0.75%
RD 19	99.01%	3.43%	96.57%	0.99%
RD 23	97.85%	3.04%	96.96%	2.15%
RD 27	99.35%	4.44%	95.56%	0.65%
Overall	98.95%	2.66%	97.34%	1.05%

speed in general. Although the false alarm rate is the highest under calm seas, its value is only around 1.6%.

The SVM-FS approach shows improved sea ice detection performance with respect to the NN-based algorithms in terms of 1) enhanced accuracy and improved robustness with respect to false alarm, 2) reduced DDM data storage requirements, and 3) fewer tuning parameters (which allows achieving the optimal performance). Generally, the false alarm rate of this method decreases with increasing wind speed. The designed FS reduces the input size, minimizes the noise effect, and helps improve the accuracy of machine learning-based methods, which may open a new window for more FS-based applications. With the use of FS, the processing on GNSS-R raw data may also be simplified for certain real practices in the future, since the data only need to be directly processed into the Doppler-axis instead of into the 2-D delay-Doppler domain (as DDMs).

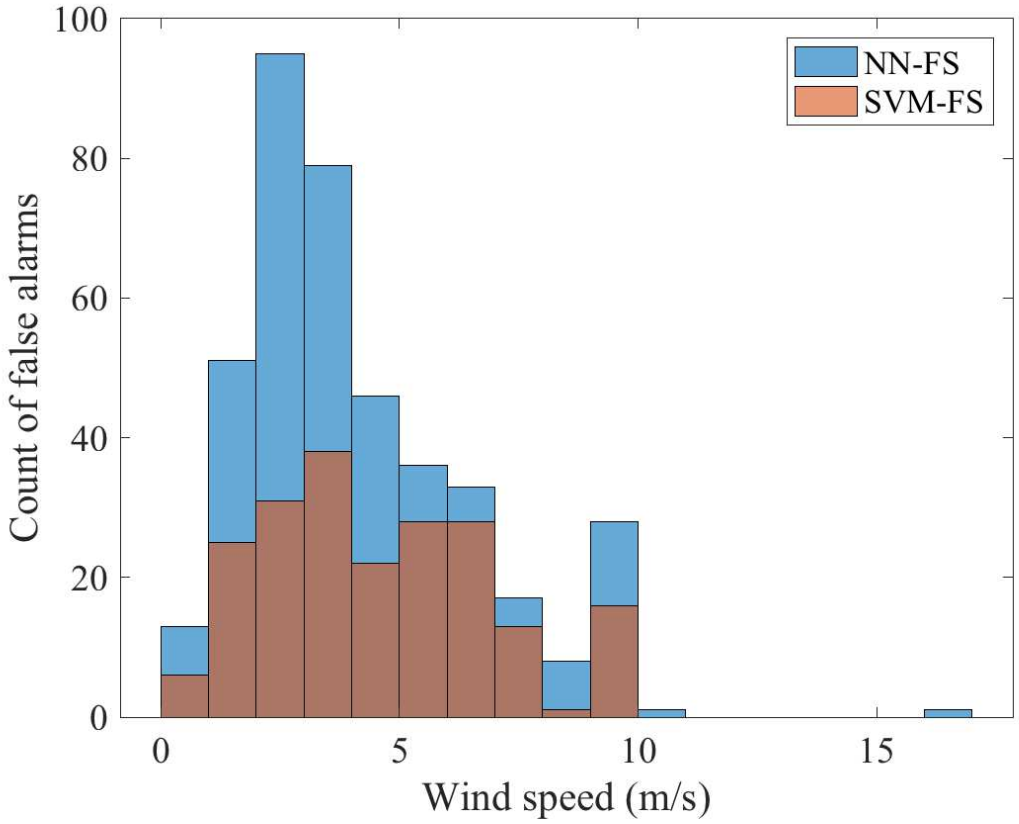

Figure 6.14: Number of false alarms for ice detection under different wind speeds: SVM-FS vs. NN-FS.

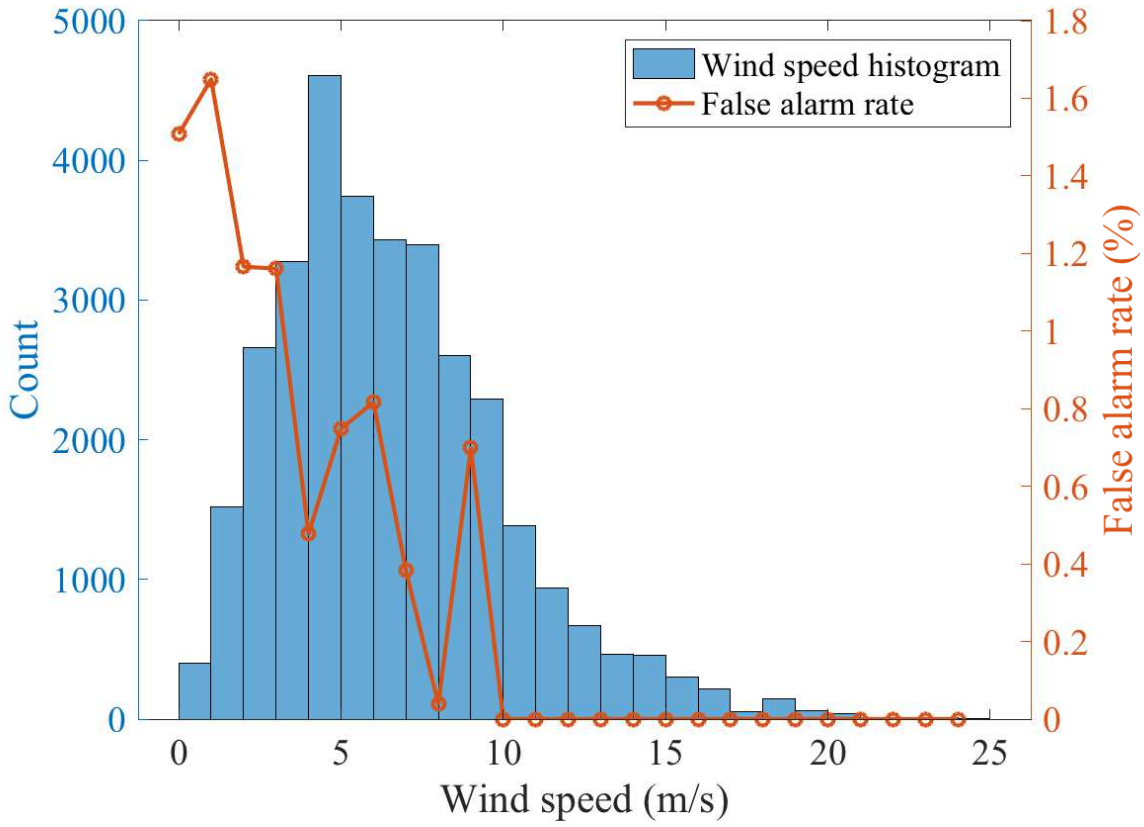

Figure 6.15: Wind speed histogram and false alarm rate for ice detection at different wind speeds.

Chapter 7

Sea Ice Thickness (SIT) Retrieval

Chapters 2–5 mainly deal with sea ice detection and SIC estimation. The goal of this chapter is to estimate sea ice thickness, which is another important sea ice parameter. A preliminary experiment in [83] found that the main reflection was from the ice-seawater interface (see Fig. 7.1 for illustration) and showed the potential of TDS-1 GNSS-R signals for estimating SIT based on the fact that the difference between the retrieved surface elevation and the mean sea surface is highly correlated with collocated SIT (with a correlation coefficient of 0.71). However, that method relies on an *ad hoc* orbit discrepancy correction and employs limited satellite raw data, which reduces its general applicability. The achieved altimetric accuracy with a root-mean-square difference (RMSD) of 4.7 cm compared with the mean sea surface should be highlighted.

At present, large-scale SIT data can be derived from 1) sea ice elevation above seawater surfaces (freeboard) measurement by satellite altimeters, e.g., European Remote Sensing (ERS) [12], ENVISAT [118], and CryoSat-2 [3], based on the conversion

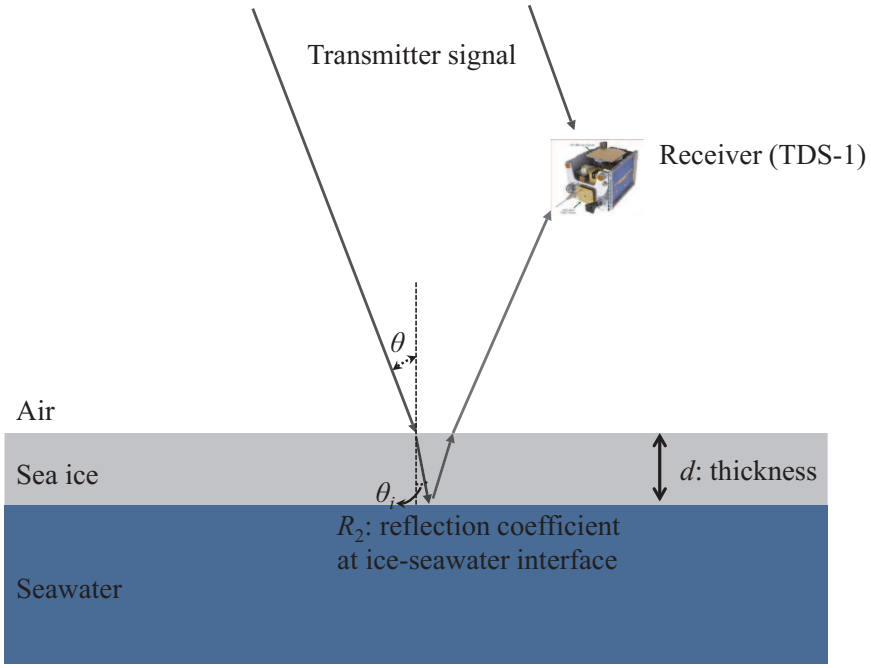

Figure 7.1: Schematic of GNSS-R signal reflected from a three-layer model of air, sea ice, and seawater.

between SIT and freeboard; or 2) microwave radiometry, e.g., Soil Moisture Ocean Salinity (SMOS) [119] and Soil Moisture Active Passive (SMAP) [120], according to the model of brightness temperature measurement and SIT [10]. For GNSS-R, the altimetry technique can be applied for SIT estimates, but the error obtained in previous research is severe with a RMSD of 4.4 m [82], which will lead to a high discrepancy in SIT estimation. In addition, Mayers and Ruf [121] confirmed the possibility of measuring SIT with GNSS-R based on simulated data. This method, however, cannot be implemented currently due to lack of raw data. Therefore, a new scheme for estimating SIT needs to be devised for GNSS-R. As such, in this study, a model is developed for retrieving sea ice thickness from a TDS-1 reflectivity (Γ). The SIT estimates are validated with good consistency with two different reference data: 1) the Soil Moisture Ocean Salinity (SMOS) results from University of Hamburg and 2) the combined SMOS/Soil Moisture Active Passive (SMAP) measurements from University of Bremen. The remainder of the chapter is organized as follows. Section 7.1 introduces the experimental and reference data. The proposed Γ-based SIT estimation scheme is described in Section 7.2. Results and discussions are presented in Section 7.3.

7.1 Data Description

7.1.1 TDS-1 Remote Sensing Data

In this subsection, the remote sensing data used for SIT retrieval are from the TDS-1 satellite, which provides a good coverage over northern high-latitude ice-covered

regions in seas above 80°N. The dataset used in this work spans a period from December 2016 to December 2018. The data employed for deriving Γ at SP include 1) the DDM files (depicting scattering power over surfaces), 2) the metadata files (providing locations of the transmitter and receiver, the incidence angle, the antenna gain, and the acquisition time), and 3) the direct signal power files (measuring the direct signal power from transmitter). The total amount of data for TDS-1 measurements examined in this work is more than 4.8 million samples, which are collected from 42714 separate tracks.

7.1.2 Reference Data

7.1.2.1 Γ Reference–Cyclone GNSS (CYGNSS)

CYGNSS was launched in 2016, and has provided measurements since March 2017. The achievable average revisit time is 4 hours [55] and the spatial resolution can be about 10 km for cases of incoherent scattering and about 500 m for coherent cases [56]. It only covers low-latitude regions between 40°S and 40°N, thus it is of limited application for sea ice sensing. However, it allows reflectivity estimation, which is employed here to validate the derived TDS-1 Γ for subsequent SIT estimation. Data with an SNR over 3 dB at SP and with an incidence angle less than 30° at SP are retained here to match with the data quality control strategy adopted for TDS-1 (see subsection 7.3.1).

7.1.2.2 SIT Reference–SMOS and Combined SMOS/SMAP

SMOS [119] produced daily sea ice thickness data in the northern hemisphere during intervals from October 15 to April 15 of 2010–2019. An example of SMOS SIT data is shown in Fig. 7.2. The uncertainty in such SIT data is available and is necessary for quality control purposes according to the data product manual (available on `https://icdc.cen.uni-hamburg.de/1/daten/cryosphere/l3c-smos-sit.html`). In this work, SIT data with uncertainties over 0.5 m are discarded. Consequently, the maximum sea ice thickness of selected reference data is about 0.8 m since uncertainties for thicker sea ice are higher. Because of the low uncertainty of the data, the SMOS SIT is regarded as ground-truth in this study. In addition, the dataset also includes sea ice salinity and temperature information, which will be treated as *a priori* information here. Since these two parameters can be dependent on the associated SIT, another sea ice thickness product that combines SMOS and SMAP measurements [120] is also employed for validation.

7.2 Retrieval of Sea Ice Thickness From Reflectivity

7.2.1 Derivation of Reflectivity

It has been demonstrated that the GNSS-R received signal over sea ice is usually a coherent reflection due to its smooth surface [66], [73]. For coherent reflection, Γ at

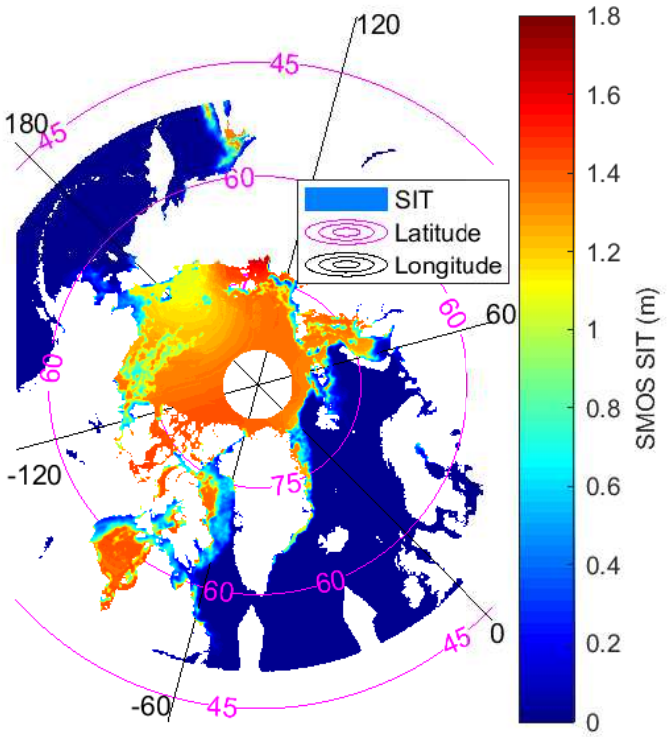

Figure 7.2: An example of reference SMOS SIT data for 3 February, 2018. Regions without data are colored in white.

SP can be obtained with the corresponding received power [122], [123] through

$$\Gamma = \frac{16\pi^2}{\lambda^2}\frac{P_r}{P_t}\frac{(R_t + R_r)^2}{G_t G_r}, \tag{7.1}$$

where $\lambda = 19$ cm is the GNSS-R signal wavelength, and P_t and P_r denote the transmitted and received power, respectively. G_t and G_r represent the antenna gains of the transmitter and receiver, and R_t and R_r are the distances from the transmitter and receiver to the specular point.

G_r at SP can be obtained from the metadata file. R_t and R_r can be easily derived given the positions of the transmitter, receiver and SP, which are also provided in the metadata. For each DDM, the column with zero-Doppler shift (also known as the delay waveform) is extracted. P_r at SP is determined as the power value of the bin with the maximum first-order derivative of the waveform (with respect to delay), as described in [124]. The availability of direct signal power files (that record the direct signal from the transmitter at zenith) improves the estimate of the transmitted signal power, which can be derived through

$$P_t G_t = 4\pi R_d^2 G_d P_d, \tag{7.2}$$

where R_d is the distance from transmitter to receiver, P_d is the direct power, and G_d is the zenith antenna gain. Lacking precise knowledge of G_d, it is set as 3 in this study, using the gain at 90° provided in [125].

As P_r is taken from a region immediately surrounding the SP, the value of Γ and above-mentioned parameters are assumed to be constant over this region [45]. In the case of coherent reflection, the area of this region can be determined as the size of the first Fresnel zone, which is about several hundred meters depending on the geometry [43], and it is regarded as the spatial resolution of this method.

7.2.2 Relationship Between SIT and Γ

For coherent reflection, Γ can be modeled as [126],

$$\Gamma = |R|^2 \cdot \exp\left[-\left(\frac{4\pi}{\lambda}\sigma_{rms}\cos\theta\right)^2\right], \tag{7.3}$$

where R is the Fresnel reflection coefficient, σ_{rms} is the surface RMS height, and θ is the incidence angle. The second term in this equation depicts the roughness; it is clear that this term is approximately 1 for smooth surfaces with a very small σ_{rms}, and thus, the following approximation can be made,

$$\Gamma = |R|^2. \tag{7.4}$$

Henceforth, in this chapter only the TDS-1 measurement of coherent reflection will be considered for SIT retrieval based on Eq. (7.4).

Considering a three-layer air-ice-seawater model (see Fig. 7.1 for illustration), R can be expressed as [127],

$$R = \frac{R_1 + R_2 e^{-2ik_{zi}d}}{1 + R_1 R_2 e^{-2ik_{zi}d}}, \tag{7.5}$$

where R_1 and R_2 denote the reflection coefficients at the upper (air-sea ice) and lower (sea ice-seawater) interfaces, respectively, d is sea ice thickness, and k_{zi} is the z-component of the signal propagation vector in the sea ice. The formula of k_{zi} contains a real part, which is referred to as the phase constant β, and an imaginary part, which is called the attenuation coefficient, α; and is given as

$$k_{zi} = \beta - i\alpha. \tag{7.6}$$

As pointed out in [83], due to a lower dielectric difference between the air and sea ice layer than that between the sea ice and water layer, R_1 is less than R_2, and

accordingly, the signals are mainly reflected by the ice-water interface for the case of first-year sea ice with a thickness of 20 to 60 cm. This is supported by the finding in [83] that the gap between the estimated surface elevation and the mean sea surface is highly correlated with local SIT. A similar phenomenon of strong reflection from the ice-water layer is also noted in [128], [129]. For this reason, the factor R_1 in Eq. (7.5) can be neglected here, which gives

$$R \approx R_2 e^{-2ik_{zi}d}, \tag{7.7}$$

and by combining Eqs. (7.4), (7.6) and (7.7), we have

$$\Gamma = |R_2|^2 e^{-4\alpha d}. \tag{7.8}$$

The expression for α is (see e.g. [10]),

$$\alpha = \frac{2\pi}{\lambda} \cos\theta \left|\mathrm{Im}\left\{\sqrt{\varepsilon_i}\right\}\right|, \tag{7.9}$$

with ε_i, λ, and θ being the relative permittivity of sea ice (relative to air), the GNSS-R signal wavelength, and the incidence angle, respectively.

In summary, in this study the reflectivity Γ of an ice-covered sea surface is modeled as the product of the propagation loss within the ice layer and the reflection coefficient at the ice-seawater interface. Thus, sea ice thickness d can be estimated as

$$d = \frac{-1}{4\alpha} \ln \frac{\Gamma}{|R_2|^2}, \tag{7.10}$$

with Γ and the values of R_2 and α. For R_2 and α, their derivations will be described in the following subsection.

7.2.3 Dielectric Models

From Eq. (7.9), it can be seen that α is dependent on ε_i. The model of [130] is adopted here for obtaining ε_i based on the relative brine volume (V_b, in ‰, or per thousand),

$$\varepsilon_i = 3.1 + 0.0084V_b + i(a_1 + a_2V_b), \tag{7.11}$$

with $a_1 = 0.037, a_2 = 0.00445$ for first-year ice, or $a_1 = 0.003, a_2 = 0.00435$ for multi-year ice. To derive V_b, the following empirical formula is presented in [131]

$$V_b = 10^{-3}S\left(-\frac{49.185}{T} + 0.532\right), \tag{7.12}$$

where S and T are sea ice salinity (in ‰) and temperature (in degrees Celsius), respectively.

R_2 can be expressed by the combination of horizontally and vertically polarized reflection coefficients (i.e., R_{hh} and R_{vv}) [132], as

$$R_2 = \frac{1}{2}\left(R_{vv} - R_{hh}\right), \tag{7.13}$$

and

$$R_{vv} = \frac{\varepsilon_r \cos\theta_i - \sqrt{\varepsilon_r - \sin^2\theta_i}}{\varepsilon_r \cos\theta_i + \sqrt{\varepsilon_r - \sin^2\theta_i}}, \tag{7.14}$$

$$R_{hh} = \frac{\cos\theta_i - \sqrt{\varepsilon_r - \sin^2\theta_i}}{\cos\theta_i + \sqrt{\varepsilon_r - \sin^2\theta_i}}, \tag{7.15}$$

$$\theta_i = \arcsin\frac{\sin\theta}{\sqrt{\varepsilon_i}}, \tag{7.16}$$

$$\varepsilon_r = \varepsilon_w/\varepsilon_i, \tag{7.17}$$

and θ_i is the incidence angle within the sea ice, and ε_w is the relative permittivity of seawater, which can be calculated using the model in [133].

Therefore, the estimated SIT from the TDS-1 Γ can be obtained based on Eq. (7.10) and Eqs. (7.1)-(7.2) for Γ, Eqs. (7.12)-(7.16) for R_2 and Eqs (7.8), (7.10)-(7.11) for α.

7.3 Results

7.3.1 Data Quality Control

In this work, only DDMs of coherent reflection are employed. This data selection process is based on the Pixel Number observable proposed in Chapter 2. It is worth mentioning that a spreading of the DDM has also been observed in some cases over sea ice, suggesting that the scattering might contain a relevant incoherent component superimposed on the coherent one [73]. However, we attempt to omit such data by discarding them according to the Pixel Number observable. In addition, following [134], data with high incidence angles are also excluded to avoid antenna side lobes. In addition, noisy data are rejected according to the SNR at SP. In summary the TDS-1 dataset used here meets the following specific empirical requirements [135]:

- The incidence angle at SP is less than 30°;
- The SNR at SP is greater than 3 dB; and
- The number of pixels with over 10% peak power is less than 20.

After applying this data quality control strategy, 18511 measurements are retained for SIT estimation, and 11401 for Γ verification. The difference in the amount of data used for these two applications lies in the spatial and temporal variations.

7.3.2 Γ: CYGNSS and TDS-1

In this study, Γ is generated from TDS-1 data. Firstly, the TDS-1 data are calibrated based on gain measurement following the steps described in [136]. The same calibration process was also used in [80]. After calibration, the unit of received power has been changed from counts to watts, and the gain and range variables are used to determine Γ as stated by Eqs. (7.1 and 7.2) in subsection 7.2.1.

In order to verify the produced TDS-1 Γ result, it is compared with the collocated Γ provided by another available GNSS-R system (i.e., CYGNSS), since these two systems had some overlapping of their operation periods from March 2017 to December 2018. Comparison is made between these two results only over ocean surfaces, with a distance less than 10 km and a time gap of less than 30 min. Despite small temporal and spatial discrepancies, both sets of results agree very well with each other, offering a correlation coefficient (r) of 0.83 and a RMSD of 0.01. These results are plotted in a $2^\circ \times 2^\circ$ (latitude/longitude) grid over the region from 40°S to 40°N, as shown in Fig. 7.3.

7.3.3 SIT estimate: SMOS and TDS-1

This subsection demonstrates the validation of TDS-1 sea ice thickness against the SMOS and SMOS/SMAP references. In order to ensure the quality of the reference data, only those with low uncertainties (less than 0.5 m) are retained. For the data studied, it turned out that the SIT under investigation is generally below 1 m, which falls in the category of first-year ice. Thus, the parameters for first-year ice are applied to Eq. (7.11). The associated SMOS sea ice temperature and salinity data are treated

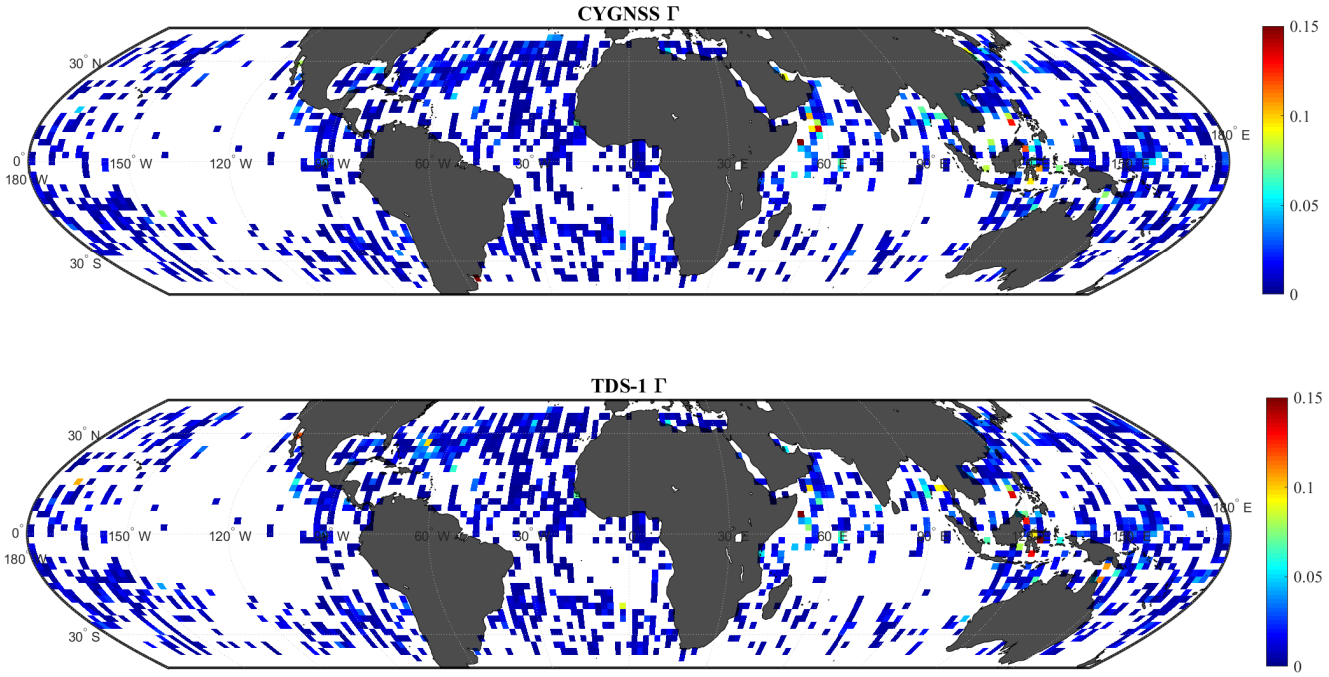

Figure 7.3: Comparison between the CYGNSS and TDS-1 Γ. A correlation coefficient of $r = 0.83$ and a RMSD of 0.01 are obtained.

as known factors in this work, and as such, SIT is estimated based on the proposed method.

The available results are grouped by month and displayed in Fig. 7.4. Note that monthly data absences are observed in both the TDS-1 and SMOS data, and the amount of qualified TDS-1 data varies among months. Nonetheless, the proposed method still shows its generality and effectiveness over different periods since no obvious discrepancy is seen in the monthly results. The overall results are plotted in the form of a density plot (Fig. 7.5), which indicates a good agreement (specifically, an r of 0.84 and a RMSD of 9.39 cm) between the TDS-1 and SMOS results, especially for the most dense data. The data densities are calculated relative to the maximum of their distribution. Due to the constraint of the SMOS data in spatial coverage, comparison is only performed for the northern hemisphere. Here, the region with a latitude above 45°N is divided into $1° \times 1°$ grids. The overall TDS-1 and SMOS SIT results are separately plotted into these grids based on their latitudes and longitudes, and averaged (see Fig. 7.6). Over this region, the difference between the averages is found to be trivial. This further validated the robustness of the developed method for different locations. Good performance in terms of both spatial and temporal variability suggests the feasibility of the proposed model with TDS-1 data for SIT estimation. The histograms of Γ, α, and $|R_2|^2$ are displayed in Fig. 7.7.

It is worth mentioning that the GNSS-R measuring geometry and power configurations of different operational tracks can vary significantly. Accordingly, the error level of the Γ retrieval and the subsequent SIT results can change notably. However, it is found here that the variation of system configurations within the same track is negligible. Thus, it is meaningful to inspect the changing trends of both TDS-1 and

SMOS SITs within each track. Taking the results of January 2017 as an example (see Fig. 7.4), regardless of offset between these two SITs, they generally follow the same tendency within each track (that is divided by vertical lines).

It should be pointed out that the retrieved SIT result is also sensitive to sea ice concentration. The absolute value of the relative difference between the retrieved SIT and SMOS reference for varying SICs has been depicted in Fig. 7.8. It can be found in general that the higher the SIC is, the more accurate the retrieved result will be. On the other hand, the reference SMOS data requires assumptions of 100% SIC, which may lead to errors when the actual SIC is low. This may account for the high discrepancy between the TDS-1 and SMOS SITs when SIC is low due to the limitation of SMOS data for low SIC scenarios.

The SMOS sea ice thickness data used above were provided by the University of Hamburg. Their corresponding S and T data are employed for sea ice thickness estimation in this study to compare with the SMOS results. It may be better to use the SMOS S and T and compare the sea ice thickness estimation result with a different data source. In order to further validate the retrieval results, comparison with the combined SMOS/SMAP data from the University of Bremen [120] is also conducted, and the corresponding RMSD and correlation coefficient are 9.49 cm and 0.67, respectively. Similarly, the monthly comparison, density plot and spatial distribution results are displayed in Figs. 7.9–7.11, respectively.

It should be noted that both GNSS-R and SMOS/SMAS adopt L-band signals, and their frequencies, specifically, 1.57 GHz for GNSS-R and 1.41 GHz for SMOS/SMAP, are close to each other. Thus, their sensitivity to SIT with respect to signal frequencies is similar.

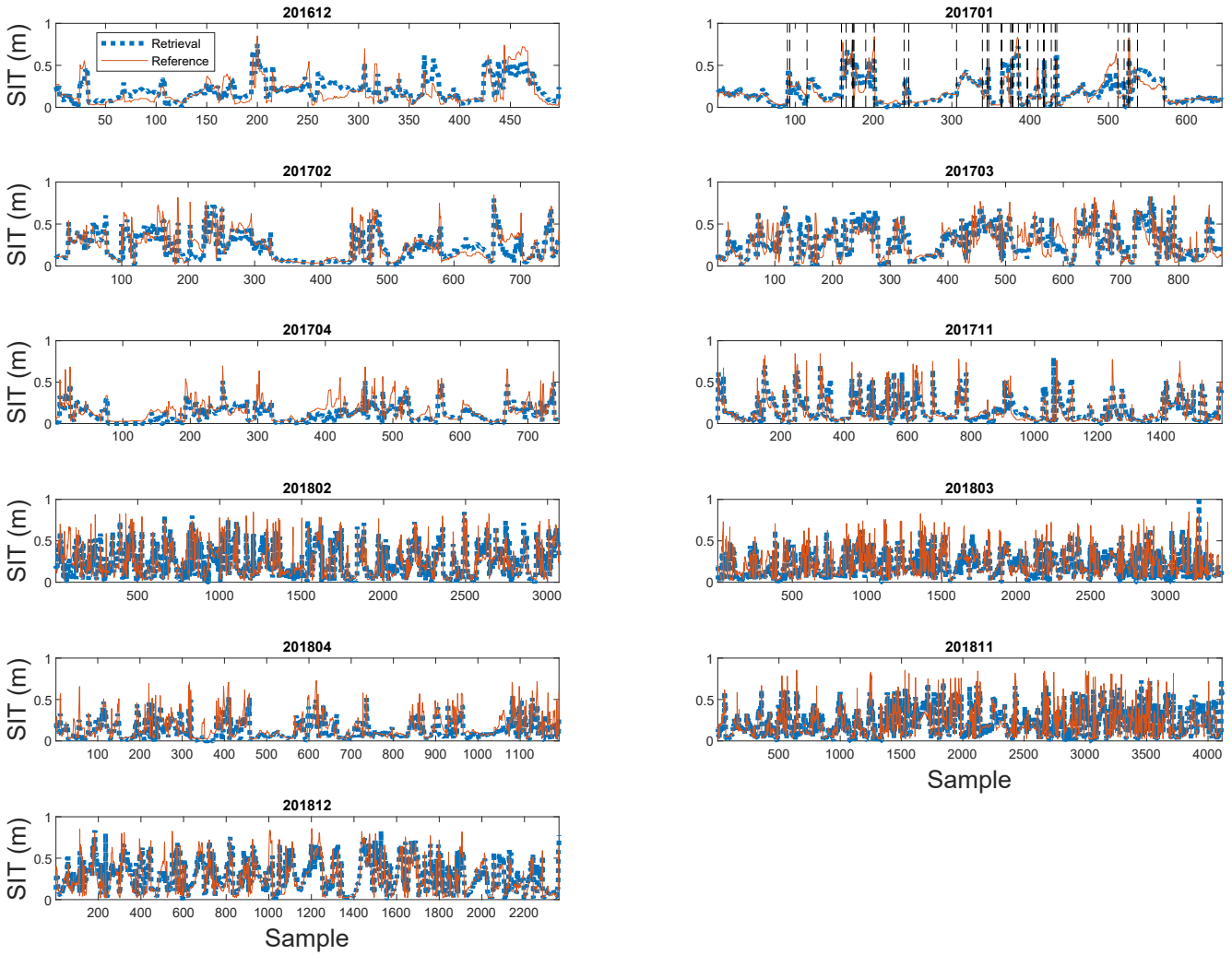

Figure 7.4: Comparison of SIT estimation results by month: TDS-1 and SMOS. As an example (January 2017), the results obtained within the same track are grouped together by blocks separated by vertical dashed lines.

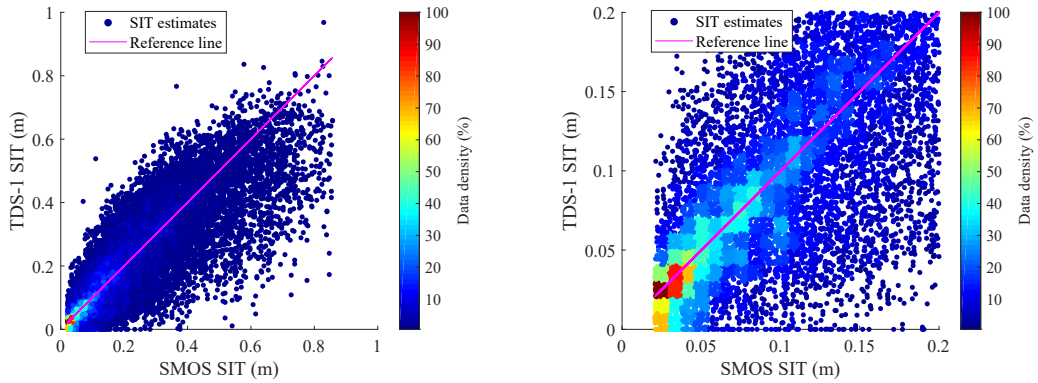

(a) (b)

Figure 7.5: Density plot comparing SIT from TDS-1 retrieval and collocated SMOS data with the 1:1 reference line (magenta): (a) All results and (b) SMOS SIT below 0.2 m.

7.3.4 Case Study

It should be noted that the results associated with the data whose ratio between Γ and $|R_2|^2$ (or equivalently, $e^{-4\alpha d}$) is greater than 1 are assigned a SIT estimate of 0; there are 180 such measurements (out of 18511) found in the data examined in the thesis. A ratio greater than 1 indicates there is no attenuation caused by sea ice. This offers a new perspective of the proposed scheme for improving existing sea ice detection methods, in which false alarms may be made for the cases of coherent reflection from calm ocean surfaces [66], [137], and the power strength is not taken into account. Here, the following cases are studied as a proof of concept.

The specific region under investigation is illustrated in Fig. 7.12, and the date is 14 April, 2018. TDS-1 measurements from two different tracks (no. 37 that is in cyan dots and no. 42 in red) are employed. The absence of sea ice is further confirmed based on SIC reference data (from [112]) of 0 over these tracks. Moreover, the sea

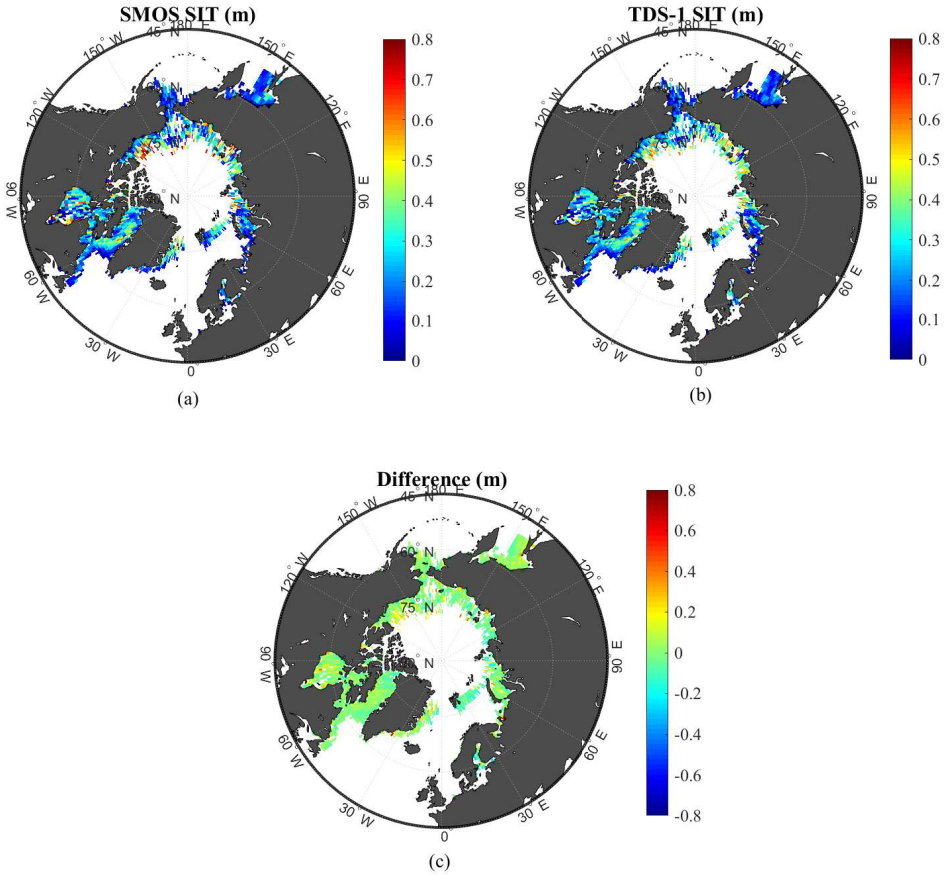

Figure 7.6: SIT values: (a) SMOS data, (b) TDS-1 results, and (c) the difference between the SMOS and TDS-1 SIT. Regions without data are in white.

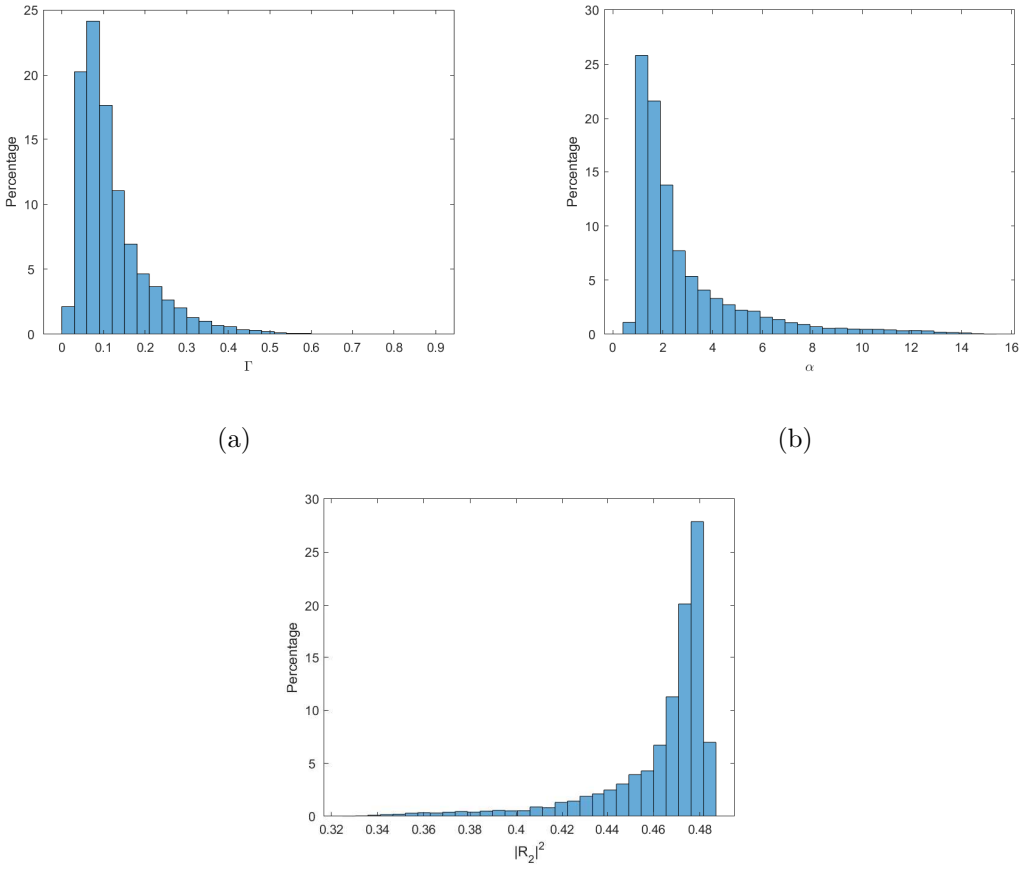

Figure 7.7: Histograms of: (a) Γ, (b) α, and (c) $|R_2|^2$.

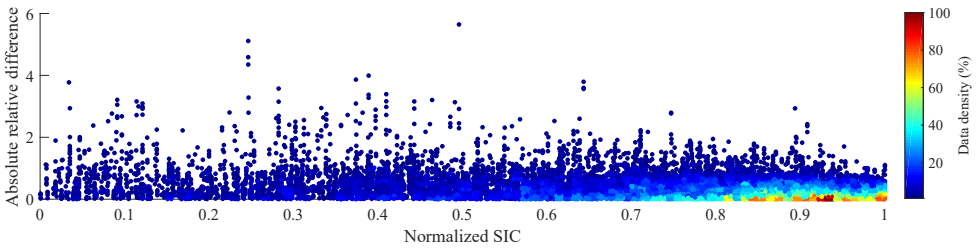

Figure 7.8: The impact of SIC on the accuracy of SIT retrieval. Higher SIC generally results in less discrepancy.

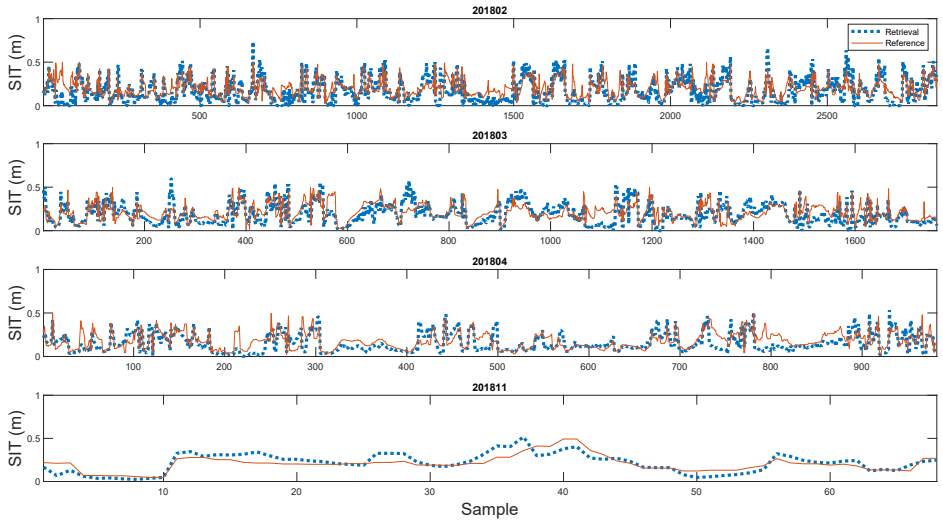

Figure 7.9: Monthly SIT result comparison between: TDS-1 and the combined SMOS/SMAP.

state is found to be low, with a WS of about 4 m/s during this period, according to the ERA-Interim data [117]. In the ice-free scenario, $|R_2|^2$ is calculated by setting ε_i as 1 (the relative permittivity of air). In general, the derived Γ is higher than $|R_2|^2$ (see Fig. 7.13), which demonstrates the absence of sea ice. However, by using existing sea ice detection methods (in which the value of signal power at SP is ignored), these measurements would produce false alarms of sea ice.

7.3.5 Error Source Analysis

This subsection lists several sources that can be responsible for the difference between the TDS-1 and SMOS SITs. These include from 1) the reference data uncertainty, 2) the error introduced by using a simplified model, and 3) drawbacks of TDS-1 in measuring Γ.

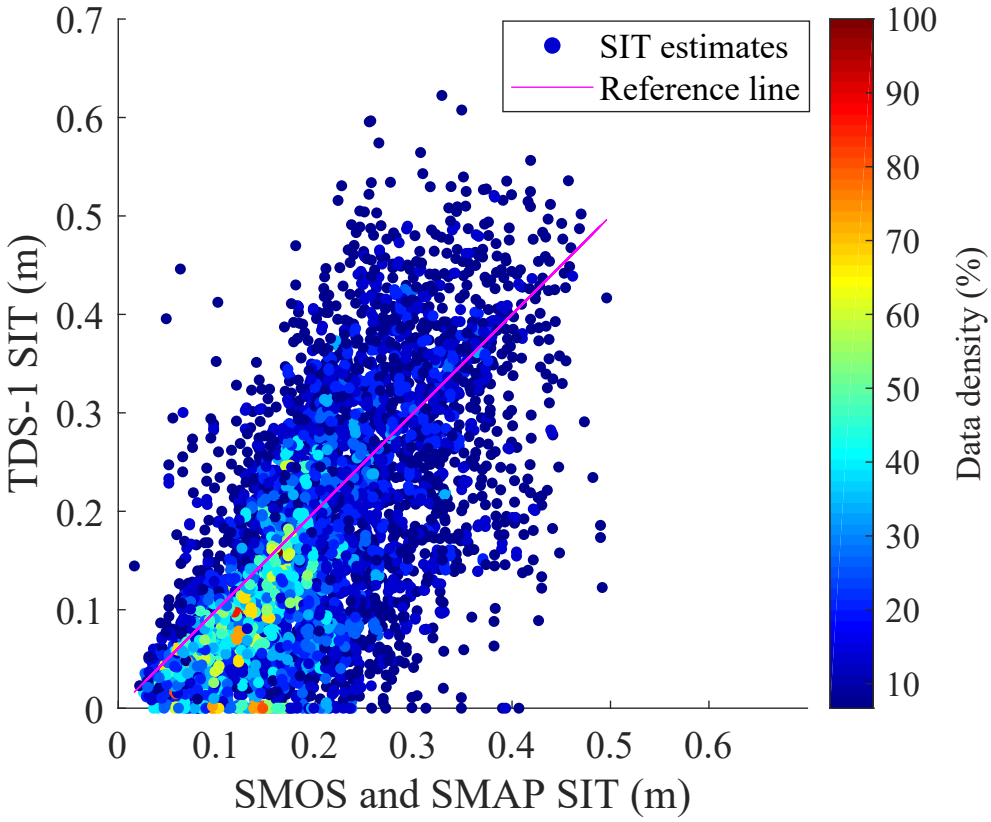

Figure 7.10: Density plot comparing SIT from TDS-1 retrieval and collocated combined SMOS/SMAP data with the 1:1 reference line (magenta).

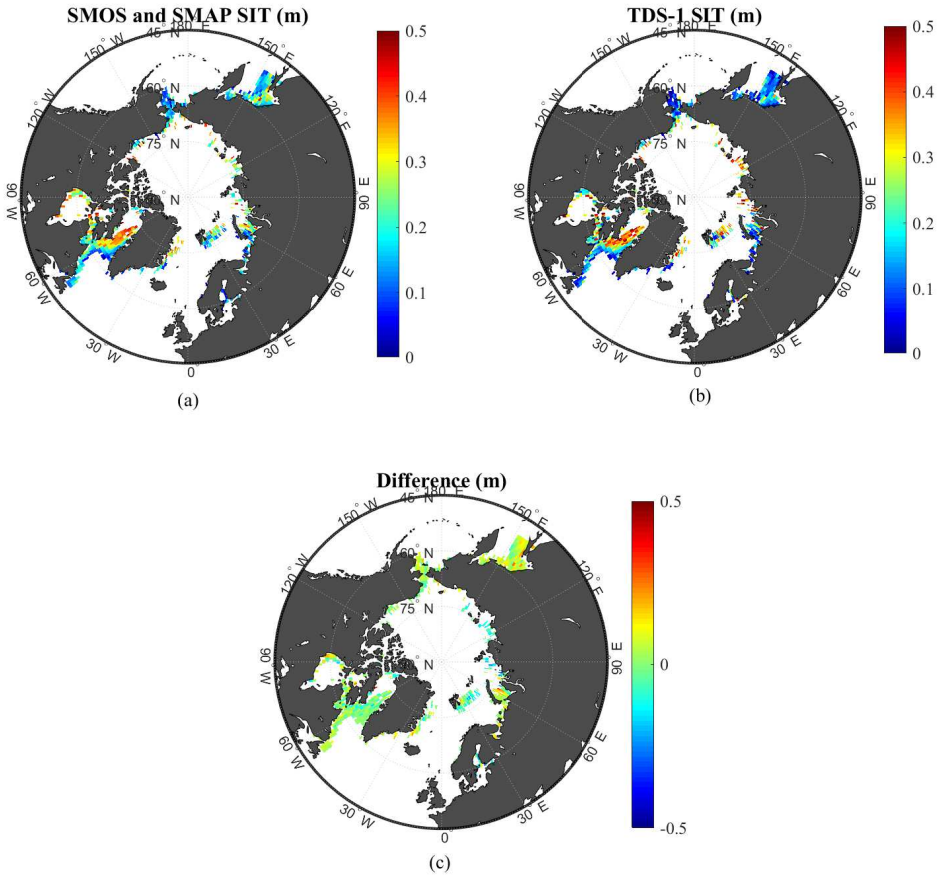

Figure 7.11: SIT values: (a) combined SMOS/SMAP data, (b) TDS-1 results, and (c) difference between the combined SMOS/SMAP and TDS-1 SIT. Regions without data are in white.

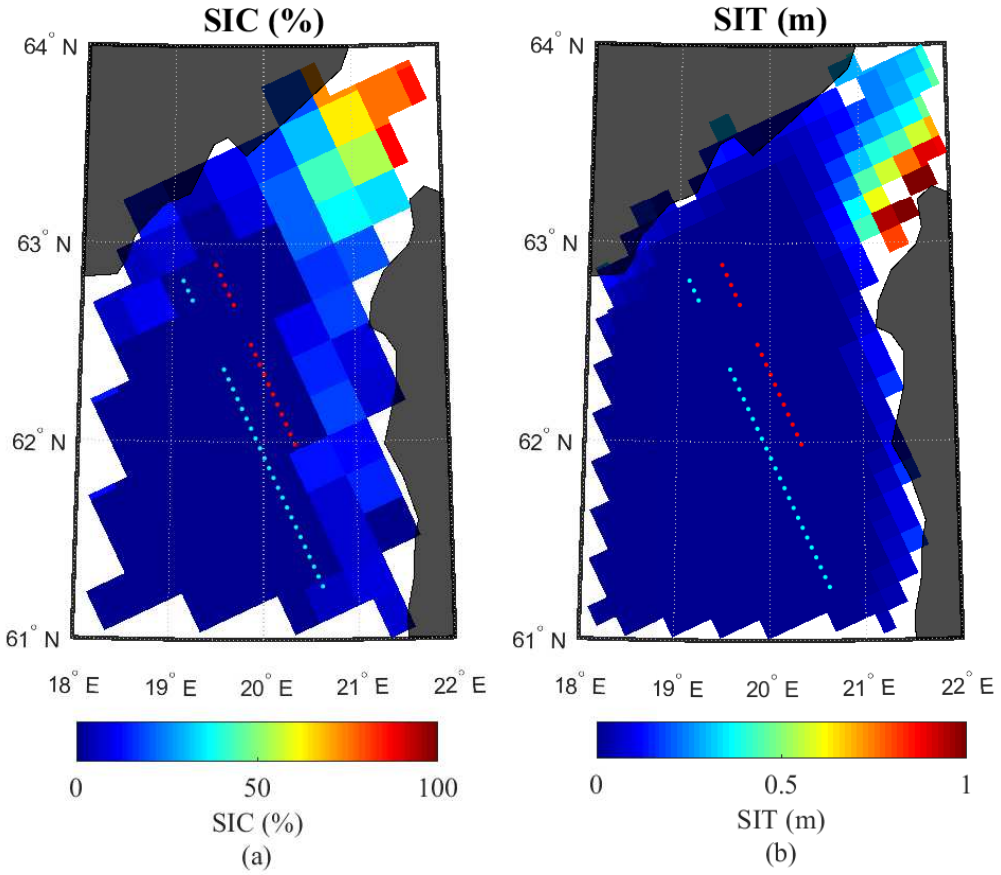

Figure 7.12: The collocated reference: (a) SIT and (b) SIC data. They confirm the absence of sea ice during the TDS-1 measurement over tracks of no. 37 (cyan dots) and no. 42 (red dots).

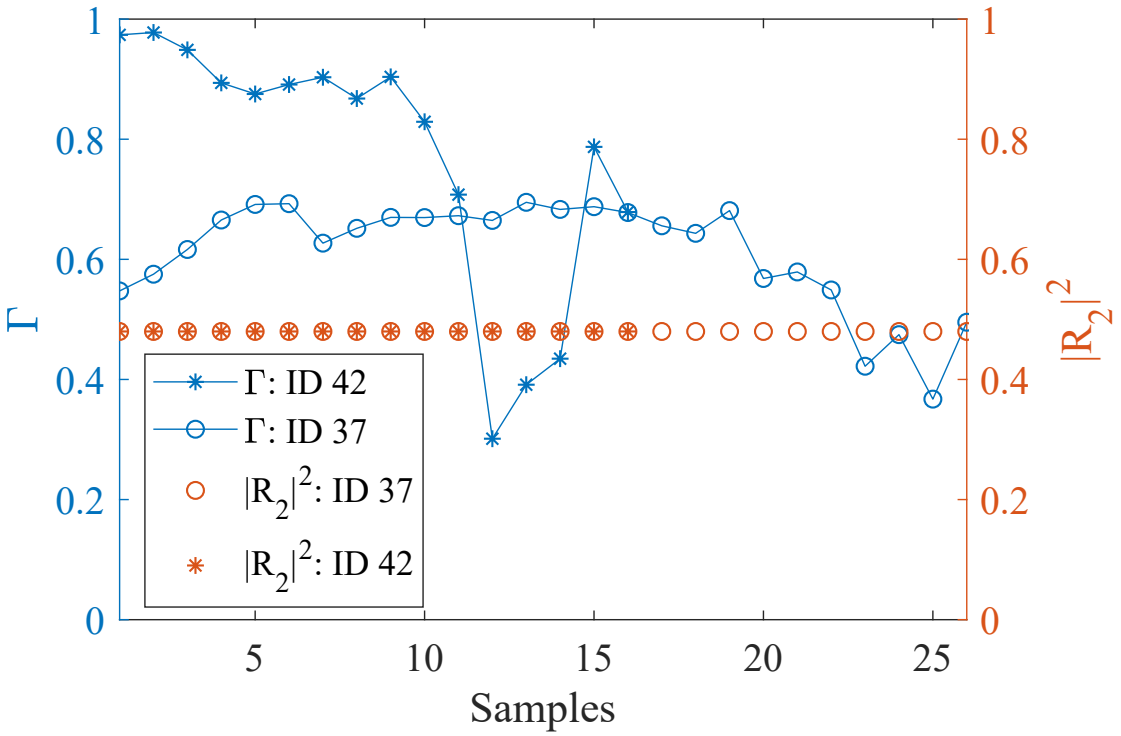

Figure 7.13: The values of Γ and $|R_2|^2$ for calm sea conditions. Data are from tracks no. 37 and no. 42 that were measured on 14 April, 2018.

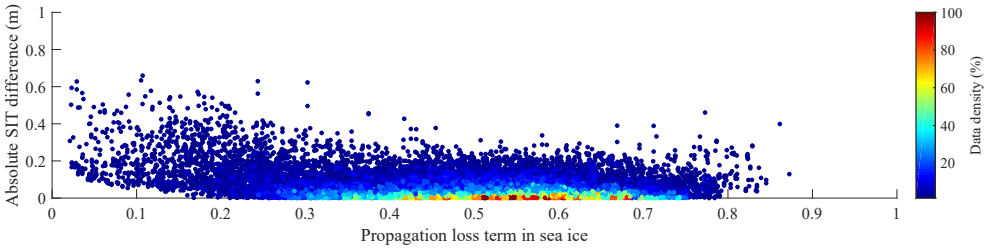

Figure 7.14: The impact of the value for loss term on the accuracy of the proposed model. Low loss term (below 0.2) introduced noticeable differences.

Firstly, the uncertainty of the SMOS SIT data employed can be up to 0.5 m. In addition, the SMOS sea ice temperature and salinity data are used as inputs, whose accuracy is also critical for the SIT estimation. It is found that R_2 ranges from 0.57 to 0.70 based on all the T and S values considered. Taking this result as the maximum uncertainty, the maximum bias of SIT estimation is only 0.04 m.

Secondly, it should be noted that Eq. (7.7) was developed from ignoring R_1 in Eq. (7.5). In fact, this process can introduce errors for the cases of high sea ice attenuation or thick ice (resulting in a low-valued propagation loss term), in which R_1 and $R_2 e^{-2ik_{zi}d}$ are comparable. In such cases, an interference between the signal components from two interfaces can be expected, and the power of overall echo should be properly evaluated. The absolute SIT difference between the TDS-1 and SMOS results (that are calculated as |SMOS SIT - TDS-1 SIT|/ SMOS SIT) was found to be noticeable with low values (below 0.2) of loss term in sea ice, as presented in Fig. 7.14. This demonstrates the limitation of the proposed model when attenuation in the ice layer is high and the contribution of R_1 is significant.

Thirdly, according to Eq. (7.10), SIT is dependent on Γ, and therefore, the accuracy of Γ is critical. The estimation of Γ may be affected by the following factors:

- Transmitted signal estimation: Although efforts have been made to approximate the actual transmitted signal by using Eq. (7.2), a constant value of G_d is employed here. This simplification may have caused errors.

- Receiver antenna gain: The uncertainty of TDS-1 attitude and orbit was noted in e.g. [134], which consequently resulted in the uncertainty in G_r.

- Atmospheric effects: As shown in [24], such effects may introduce variations in P_r; however, they are neglected in this work.

The error for G_d can be up to 0.8 dB [125]. The median values of the errors in G_r are found to be 0.7 dB through processing TDS-1 data. By only considering such error in the antenna gains, the uncertainty of SIT retrieval can be up to about 30%.

7.4 Conclusions

An effective scheme is developed for estimating sea ice thickness from the reflectivity produced with TDS-1 data. Good consistency between the derived TDS-1 SIT and the reference SIT demonstrates the applicability of the developed model and the utility of TDS-1 data for SIT estimation.

Chapter 8

Conclusions

8.1 Summary

The objectives of this thesis have been to propose new methods to promote sea ice remote sensing applications, specifically, 1) sea ice detection, 2) SIC estimation, and 3) SIT retrieval using spaceborne GNSS-R data acquired by the TDS-1 satellite. To fulfill this goal, several different methods have been proposed. For the sea ice detection task, four methods i.e. the observable-, NN-, CNN- and SVM-based approaches are developed. For SIC estimation, the algorithms of NN, CNN and SVR are investigated, respectively. For SIT retrieval, a model based on reflectivity Γ is proposed. Comparisons with ground-truth data confirm the good performance of the proposed schemes. Experimental evaluation shows high accuracy has been obtained in these applications. For sea ice detection and SIC estimation, different methods using various input designs are also tested and compared, with the overall detection accuracy and the correlation coefficient between predicted and reference SICs being above 97%

and 0.91, respectively. For SIT retrieval, the reflectivity Γ is modelled as a function of the propagation loss in the sea ice layer and the reflection coefficient of the underneath seawater. By comparing the TDS-1 SIT with the reference data, a good consistency was obtained with an r of 0.84 and an RMSD of 9.39 cm for SMOS and an r of 0.67 and an RMSD of 9.49 cm for SMOS/SMAP. Furthermore, another aspect of this method for improving sea ice detection was studied by comparing Γ with local reflection coefficient. In particular, the scheme for retrieving SIT is helpful in reducing false alarms of sea ice for low sea state. The proposed methods can provide measurement for high-latitude regions, which may be difficult to obtain using *in situ* techniques.

Hence, the feasibility of spaceborne GNSS-R DDM for sea ice remote sensing is illustrated for the first time using the TDS-1 data.

8.2 Discussion and Future Work

While these methods hold great potential, further testing with more DDM data is necessary, and this may increase the robustness for real-world applications. In addition, it was found that the performance of sea ice detection and SIC estimation dropped for partially ice-covered areas, for which DDMs also depends on sea surface wind conditions. Therefore, it is worth investigating the scattering properties of GNSS-R signals for such regions. In particular, the DDMs collected near ice edges with calm seas and low wind speeds appear to give rise to overestimates of the SIC and increased false alarms. However, a further quantification analysis of the effect of low sea state on SIC estimation should be conducted in the future using more *in situ*

sea state data and DDM data. Although the adopted resolution matching scheme can provide reasonable comparisons between DDMs and SIC data, it cannot provide the details about spatial coverage and its distribution of a DDM. The dry/wet ice conditions may affect the performance of SIC estimation. It has been reported in [138] that melt water can lead to multiple contrast reversals on sea ice microwave signatures for different ice stages and seasons. However, due to lack of the dry/wet ice condition data, its effect on the detection performance could not be evaluated in this work. This problem should be investigated once such data become available. Dependence of SIC estimation on ice thickness will also be studied. This work may open a window for more DDM-based remote sensing applications with machine learning methods in the future. In order to maintain good spatial resolution of TDS-1 DDM, no extra non-coherent summation over DDM is applied in this work, but this process could be investigated further to mitigate speckle noise and enhance performance. The devised FS scheme has also been shown to be useful in this thesis, which may lead to more FS-based applications. In addition, with the use of FS the processing of GNSS-R raw data may also be simplified for certain real practices.

Although the results obtained show the applicability of the proposed method, the performance of this method for sea ice thicker than 1 m is not examined due to a lack of reliable SIT reference data. Further validation of this method for thick sea ice should be conducted when accurate SIT reference data are available. In addition, as the SMOS/SMAP SIT estimation is also derived with the L-band microwave signal and based on similar methodology (propagation attenuation of sea ice), so they can be expected to be correlated with the GNSS-R SIT measurements. It is worth comparing the GNSS-R results with measurements from other sources, such as CryoSat-2

and airborne SIT data once more appropriate data are available. Moreover, when the attenuation in sea ice is significant the proposed model produces noticeable errors. This can be corrected in the future by considering a more comprehensive model. It should be mentioned that the data containing incoherent components due to incoherent reflection from sea ice covered area are not considered in this work. However, their effect on SIT estimation accuracy should be studied. It also should be noted that the input of sea ice temperature and salinity are from SMOS data, the accuracy of which is unknown, and this may be responsible, to some degree, for errors. The accuracy of SIT estimation using GNSS-R can be enhanced in the future when GNSS-R instruments can provide better data or when the effect of error sources (described in subsection 7.3.5) can be mitigated. Furthermore, although an empirical geophysical model function method needs a calibration procedure which is not required in the proposed method, it is worth investigating SIT estimation using an empirical GMF method in the future. More importantly, an enhanced SIT estimation scheme that does not rely on S and T from other sources should be developed in the future so that GNSS-R can produce SIT data independently.

A comprehensive comparison between our proposed sea ice detection, SIC and SIT estimation methods and those newly developed by other researchers is also necessary in the future. A machine learning based algorithm for sea ice classification can also be designed and compared with that in [80].

Bibliography

[1] D. A. Rothrock, Y. Yu, and G. A. Maykut, "Thinning of the Arctic sea-ice cover," *Geophys. Res. Lett.*, vol. 26, no. 23, pp. 3469–3472, Dec. 1999.

[2] J. C. Comiso, C. L. Parkinson, R. Gersten, and L. Stock, "Accelerated decline in the Arctic sea ice cover," *Geophys. Res. Lett.*, vol. 35, no. 1, p. L01703, Jan. 2008.

[3] S. W. Laxon, K. A. Giles, A. L. Ridout, D. J. Wingham, R. Willatt, R. Cullen, R. Kwok, A. Schweiger, J. Zhang, C. Haas, S. Hendricks, R. Krishfield, N. Kurtz, S. Farrell, and M. Davidson, "CryoSat-2 estimates of Arctic sea ice thickness and volume," *Geophys. Res. Lett.*, vol. 40, no. 4, pp. 732–737, Feb. 2013.

[4] D. Hartman, A. Klein Tank, M. Rusicucci, L. Alexander, B. Broenniman, Y. Charabi, F. Dentener, E. Dlugokencky, E. Easterling, A. Kaplan, B. Soden, P. Thorne, M. Wild, P. Zhai, and E. Kent, *Observations: Atmosphere and Surface*. Cambridge University Press, 2013.

[5] R. G. Barry, M. C. Serreze, J. A. Maslanik, and R. H. Preller, "The Arctic Sea Ice-Climate System: Observations and modeling," *Rev. Geophys.*, vol. 31, no. 4, p. 397, Nov. 1993.

[6] M. G. McPhee, A. Proshutinsky, J. H. Morison, M. Steele, and M. B. Alkire, "Rapid change in freshwater content of the Arctic Ocean," *Geophys. Res. Lett.*, vol. 36, no. 10, p. L10602, May 2009.

[7] R. J. Galley, B. Else, S. Prinsenberg, D. Babb, and D. Barber, "Summer Sea Ice Concentration, Motion, and Thickness Near Areas of Proposed Offshore Oil and Gas Development in the Canadian Beaufort Sea – 2009," *ARCTIC*, vol. 66, no. 1, pp. 105–116, Mar. 2013.

[8] S. Sandven, O. M. Johannessen, and K. Kloster, *Sea Ice Monitoring by Remote Sensing*. Chichester, UK: John Wiley & Sons, Ltd, Sep. 2006.

[9] T. Martin and E. Augstein, "Large-scale drift of Arctic Sea ice retrieved from passive microwave satellite data," *J. Geophys. Res. Ocean.*, vol. 105, no. C4, pp. 8775–8788, Apr. 2000.

[10] L. Kaleschke, N. Maaß, C. Haas, S. Hendricks, G. Heygster, and R. T. Tonboe, "A sea-ice thickness retrieval model for 1.4 GHz radiometry and application to airborne measurements over low salinity sea-ice," *Cryosph.*, vol. 4, no. 4, pp. 583–592, Dec. 2010.

[11] Y. Zhao, A. Liu, and D. Long, "Validation of sea ice motion from QuikSCAT with those from SSM/I and buoy," *IEEE Trans. Geosci. Remote Sens.*, vol. 40, no. 6, pp. 1241–1246, Jun. 2002.

[12] S. W. Laxon, N. Peacock, and D. Smith, "High interannual variability of sea ice thickness in the Arctic region," *Nature*, vol. 425, no. 6961, pp. 947–950, Oct. 2003.

[13] R. Kwok and G. F. Cunningham, "Seasonal ice area and volume production of the Arctic Ocean: November 1996 through April 1997," *J. Geophys. Res.*, vol. 107, no. C10, p. 8038, Oct. 2002.

[14] L. Wang, K. A. Scott, L. Xu, and D. A. Clausi, "Sea ice concentration estimation during melt from dual-pol SAR scenes using deep convolutional neural networks: A case study," *IEEE Trans. Geosci. Remote Sens.*, vol. 54, no. 8, pp. 4524–4533, Aug. 2016.

[15] F. Gao, X. Wang, Y. Gao, J. Dong, and S. Wang, "Sea Ice Change Detection in SAR Images Based on Convolutional-Wavelet Neural Networks," *IEEE Geosci. Remote Sens. Lett.*, vol. 16, no. 8, pp. 1240–1244, Aug. 2019.

[16] N. Longepe, P. Thibaut, R. Vadaine, J.-C. Poisson, A. Guillot, F. Boy, N. Picot, and F. Borde, "Comparative Evaluation of Sea Ice Lead Detection Based on SAR Imagery and Altimeter Data," *IEEE Trans. Geosci. Remote Sens.*, vol. 57, no. 6, pp. 4050–4061, Jun. 2019.

[17] C. Hall and R. Cordey, "Multistatic Scatterometry," in *Int. Geosci. Remote Sens. Symp.*, IEEE, 1988, pp. 561–562.

[18] J. Garrison, A. Komjathy, V. Zavorotny, and S. Katzberg, "Wind speed measurement using forward scattered GPS signals," *IEEE Trans. Geosci. Remote Sens.*, vol. 40, no. 1, pp. 50–65, 2002.

[19] S. J. Katzberg, O. Torres, and G. Ganoe, "Calibration of reflected GPS for tropical storm wind speed retrievals," *Geophys. Res. Lett.*, vol. 33, no. 18, n/a–n/a, Sep. 2006.

[20] J. F. Marchan-Hernandez, N. Rodriguez-Alvarez, A. Camps, X. Bosch-Lluis, I. Ramos-Perez, and E. Valencia, "Correction of the sea state impact in the L-Band brightness temperature by means of delay-Doppler maps of global navigation satellite signals reflected over the sea surface," *IEEE Trans. Geosci. Remote Sens.*, vol. 46, no. 10, pp. 2914–2923, Oct. 2008.

[21] N. Rodriguez-Alvarez, D. M. Akos, V. U. Zavorotny, J. A. Smith, A. Camps, and C. W. Fairall, "Airborne GNSS-R wind retrievals using delay–Doppler maps," *IEEE Trans. Geosci. Remote Sens.*, vol. 51, no. 1, pp. 626–641, Jan. 2013.

[22] M. P. Clarizia, C. S. Ruf, P. Jales, and C. Gommenginger, "Spaceborne GNSS-R minimum variance wind speed estimator," *IEEE Trans. Geosci. Remote Sens.*, vol. 52, no. 11, pp. 6829–6843, Nov. 2014.

[23] C. Li and W. Huang, "An algorithm for sea-surface wind field retrieval from GNSS-R delay-doppler map," *IEEE Geosci. Remote Sens. Lett.*, vol. 11, no. 12, pp. 2110–2114, Dec. 2014.

[24] G. Foti, C. Gommenginger, P. Jales, M. Unwin, A. Shaw, C. Robertson, and J. Roselló, "Spaceborne GNSS reflectometry for ocean winds: First results from the UK TechDemoSat-1 mission," *Geophys. Res. Lett.*, vol. 42, no. 13, pp. 5435–5441, Jul. 2015.

[25] Q. Yan, W. Huang, and G. Foti, "Quantification of the relationship between sea surface roughness and the size of the glistening zone for GNSS-R," *IEEE Geosci. Remote Sens. Lett.*, vol. 15, no. 2, pp. 237–241, Feb. 2018.

[26] S. T. Lowe, C. Zuffada, Y. Chao, P. Kroger, L. E. Young, and J. L. LaBrecque, "5-cm-Precision aircraft ocean altimetry using GPS reflections," *Geophys. Res. Lett.*, vol. 29, no. 10, pp. 13–1–13–4, May 2002.

[27] A. Rius, E. Cardellach, and M. Martin-Neira, "Altimetric analysis of the sea-surface GPS-reflected signals," *IEEE Trans. Geosci. Remote Sens.*, vol. 48, no. 4, pp. 2119–2127, Apr. 2010.

[28] E. Cardellach, A. Rius, M. Martin-Neira, F. Fabra, O. Nogues-Correig, S. Ribo, J. Kainulainen, A. Camps, and S. D'Addio, "Consolidating the precision of interferometric GNSS-R ocean altimetry using airborne experimental data," *IEEE Trans. Geosci. Remote Sens.*, vol. 52, no. 8, pp. 4992–5004, Aug. 2014.

[29] M. P. Clarizia, C. Ruf, P. Cipollini, and C. Zuffada, "First spaceborne observation of sea surface height using GPS-Reflectometry," *Geophys. Res. Lett.*, vol. 43, no. 2, pp. 767–774, Jan. 2016.

[30] K. M. Larson, E. D. Gutmann, V. U. Zavorotny, J. J. Braun, M. W. Williams, and F. G. Nievinski, "Can we measure snow depth with GPS receivers?" *Geophys. Res. Lett.*, vol. 36, no. 17, p. L17502, Sep. 2009.

[31] N. Najibi, S. Jin, N. Najibi, and S. Jin, "Physical reflectivity and polarization characteristics for snow and ice-covered surfaces interacting with GPS signals," *Remote Sens.*, vol. 5, no. 8, pp. 4006–4030, Aug. 2013.

[32] J. L. McCreight, E. E. Small, and K. M. Larson, "Snow depth, density, and SWE estimates derived from GPS reflection data: Validation in the western U. S.," *Water Resour. Res.*, vol. 50, no. 8, pp. 6892–6909, Aug. 2014.

[33] S. Jin and N. Najibi, "Sensing snow height and surface temperature variations in Greenland from GPS reflected signals," *Adv. Sp. Res.*, vol. 53, no. 11, pp. 1623–1633, Jun. 2014.

[34] N. Najibi, S. Jin, and X. Wu, "Validating the Variability of Snow Accumulation and Melting From GPS-Reflected Signals: Forward Modeling," *IEEE Trans. Antennas Propag.*, vol. 63, no. 6, pp. 2646–2654, Jun. 2015.

[35] S. Jin, X. Qian, and H. Kutoglu, "Snow Depth Variations Estimated from GPS-Reflectometry: A Case Study in Alaska from L2P SNR Data," *Remote Sens.*, vol. 8, no. 1, p. 63, Jan. 2016.

[36] S. J. Katzberg, O. Torres, M. S. Grant, and D. Masters, "Utilizing calibrated GPS reflected signals to estimate soil reflectivity and dielectric constant: Results from SMEX02," *Remote Sens. Environ.*, vol. 100, no. 1, pp. 17–28, Jan. 2006.

[37] A. Alonso-Arroyo, A. Camps, A. Aguasca, G. F. Forte, A. Monerris, C. Rudiger, J. P. Walker, H. Park, D. Pascual, and R. Onrubia, "Dual-Polarization GNSS-R Interference Pattern Technique for Soil Moisture Mapping," *IEEE J. Sel. Top. Appl. Earth Obs. Remote Sens.*, vol. 7, no. 5, pp. 1533–1544, May 2014.

[38] A. Egido, S. Paloscia, E. Motte, L. Guerriero, N. Pierdicca, M. Caparrini, E. Santi, G. Fontanelli, and N. Floury, "Airborne GNSS-R Polarimetric Mea-

surements for Soil Moisture and Above-Ground Biomass Estimation," *IEEE J. Sel. Top. Appl. Earth Obs. Remote Sens.*, vol. 7, no. 5, pp. 1522–1532, May 2014.

[39] A. Camps, H. Park, M. Pablos, G. Foti, C. P. Gommenginger, P.-W. Liu, and J. Judge, "Sensitivity of GNSS-R Spaceborne Observations to Soil Moisture and Vegetation," *IEEE J. Sel. Top. Appl. Earth Obs. Remote Sens.*, vol. 9, no. 10, pp. 4730–4742, Oct. 2016.

[40] Y. Jia, P. Savi, D. Canone, and R. Notarpietro, "Estimation of surface characteristics using GNSS LH-reflected signals: Land versus water," *IEEE J. Sel. Top. Appl. Earth Obs. Remote Sens.*, vol. 9, no. 10, pp. 4752–4758, Oct. 2016.

[41] S. Jin and A. Komjathy, "GNSS reflectometry and remote sensing: New objectives and results," *Adv. Sp. Res.*, vol. 46, no. 2, pp. 111–117, Jul. 2010.

[42] S. Jin *et al.*, "Remote sensing using GNSS signals: Current status and future directions," *Adv. Sp. Res.*, vol. 47, no. 10, pp. 1645–1653, May 2011.

[43] V. U. Zavorotny, S. Gleason, E. Cardellach, and A. Camps, "Tutorial on Remote Sensing Using GNSS Bistatic Radar of Opportunity," *IEEE Geosci. Remote Sens. Mag.*, vol. 2, no. 4, pp. 8–45, Dec. 2014.

[44] Q. Yan and W. Huang, "Sea ice remote sensing using GNSS-R: A review," *Remote Sens.*, vol. 11, no. 21, p. 2565, Nov. 2019.

[45] S. Gleason, "Space-Based GNSS Scatterometry: Ocean Wind Sensing Using an Empirically Calibrated Model," *IEEE Trans. Geosci. Remote Sens.*, vol. 51, no. 9, pp. 4853–4863, Sep. 2013.

[46] Q. Yan and W. Huang, "GNSS-R Delay-Doppler Map Simulation Based on the 2004 Sumatra-Andaman Tsunami Event," *J. Sensors*, vol. 2016, pp. 1–14, Dec. 2016.

[47] ——, "Tsunami Detection and Parameter Estimation From GNSS-R Delay-Doppler Map," *IEEE J. Sel. Top. Appl. Earth Obs. Remote Sens.*, vol. 9, no. 10, pp. 4650–4659, Oct. 2016.

[48] M. Unwin, P. Jales, J. Tye, C. Gommenginger, G. Foti, and J. Rosello, "Spaceborne GNSS-Reflectometry on TechDemoSat-1: Early Mission Operations and Exploitation," *IEEE J. Sel. Top. Appl. Earth Obs. Remote Sens.*, vol. 9, no. 10, pp. 4525–4539, Oct. 2016.

[49] N. Pierdicca, A. Mollfulleda, F. Costantini, L. Guerriero, L. Dente, S. Paloscia, E. Santi, and M. Zribi, "Spaceborne GNSS Reflectometry Data for Land Applications: An Analysis of Techdemosat Data," in *IGARSS 2018 - 2018 IEEE Int. Geosci. Remote Sens. Symp.*, IEEE, Jul. 2018, pp. 3343–3346.

[50] E. Cardellach, F. Fabra, O. Nogués-Correig, S. Oliveras, S. Ribó, and A. Rius, "GNSS-R ground-based and airborne campaigns for ocean, land, ice, and snow techniques: Application to the GOLD-RTR data sets," *Radio Sci.*, vol. 46, no. 6, Dec. 2011.

[51] F. Fabra, E. Cardellach, O. Nogues-Correig, S. Oliveras, S. Ribo, A. Rius, M. Belmonte-Rivas, M. Semmling, G. Macelloni, S. Pettinato, R. Zasso, and S. D'Addio, "Monitoring sea-ice and dry snow with GNSS reflections," in *2010 IEEE Int. Geosci. Remote Sens. Symp.*, IEEE, Jul. 2010, pp. 3837–3840.

[52] A. M. Semmling, G. Beyerle, R. Stosius, G. Dick, J. Wickert, F. Fabra, E. Cardellach, S. Ribó, A. Rius, A. Helm, S. B. Yudanov, and S. D'Addio, "Detection of Arctic Ocean tides using interferometric GNSS-R signals," *Geophys. Res. Lett.*, vol. 38, no. 4, n/a–n/a, Feb. 2011.

[53] F. Fabra, E. Cardellach, A. Rius, S. Ribo, S. Oliveras, O. Nogues-Correig, M. Belmonte Rivas, M. Semmling, and S. D'Addio, "Phase Altimetry With Dual Polarization GNSS-R Over Sea Ice," *IEEE Trans. Geosci. Remote Sens.*, vol. 50, no. 6, pp. 2112–2121, Jun. 2012.

[54] Y. Zhang, W. Meng, Q. Gu, Y. Han, Z. Hong, Y. Cao, Q. Xia, and W. Wang, "Detection of bohai bay sea ice using GPS-reflected signals," *IEEE J. Sel. Top. Appl. Earth Obs. Remote Sens.*, vol. 8, no. 1, pp. 39–46, Jan. 2015.

[55] C. Ruf, M. Unwin, J. Dickinson, R. Rose, D. Rose, M. Vincent, and A. Lyons, "CYGNSS: Enabling the Future of Hurricane Prediction [Remote Sensing Satellites]," *IEEE Geosci. Remote Sens. Mag.*, vol. 1, no. 2, pp. 52–67, Jun. 2013.

[56] C. Ruf, "Cyclone Global Navigation Satellite System (CYGNSS) and Soil Moisture Product Prospects," in *SMAP CalVal Work.*, Fairfax, 2018.

[57] S. K. Rose, O. B. Andersen, M. Passaro, C. A. Ludwigsen, and C. Schwatke, "Arctic Ocean Sea Level Record from the Complete Radar Altimetry Era: 1991–2018," *Remote Sens.*, vol. 11, no. 14, p. 1672, Jul. 2019.

[58] A. Komjathy, J. Maslanik, V. Zavorotny, P. Axelrad, and S. Katzberg, "Sea ice remote sensing using surface reflected GPS signals," in *IGARSS 2000. IEEE 2000 Int. Geosci. Remote Sens. Symp.*, vol. 7, IEEE, 2000, pp. 2855–2857.

[59] M. Rivas, J. Maslanik, and P. Axelrad, "Bistatic Scattering of GPS Signals Off Arctic Sea Ice," *IEEE Trans. Geosci. Remote Sens.*, vol. 48, no. 3, pp. 1548–1553, Mar. 2010.

[60] H. Gao, D. Yang, B. Zhang, Q. Wang, and F. Wang, "Remote Sensing of Sea Ice Thickness with GNSS Reflected Signal," *J. Electron. Inf. Technol.*, vol. 39, no. 5, pp. 1096–1100, May 2017.

[61] J. Strandberg, T. Hobiger, and R. Haas, "Coastal Sea Ice Detection Using Ground-Based GNSS-R," *IEEE Geosci. Remote Sens. Lett.*, vol. 14, no. 9, pp. 1552–1556, Sep. 2017.

[62] S. Gleason, M. Adjrad, and M. Unwin, "Sensing Ocean, Ice and Land Reflected Signals from Space: Results from the UK-DMC GPS Reflectometry Experiment," in *Proc. 18th Int. Tech. Meet. Satell. Div. Inst. Navig. (ION GNSS 2005)*, Long Beach, CA, Sep. 2005, pp. 1679–1685.

[63] S. Gleason, "Remote sensing of ocean, ice and land surfaces using bistatically scattered GNSS signals from low earth orbit," PhD thesis, 2006.

[64] S. Gleason, "Towards Sea Ice Remote Sensing with Space Detected GPS Signals: Demonstration of Technical Feasibility and Initial Consistency Check Using Low Resolution Sea Ice Information," *Remote Sens.*, vol. 2, no. 8, pp. 2017–2039, Aug. 2010.

[65] Q. Yan and W. Huang, "Sea ice detection from GNSS-R Delay-Doppler Map," in *2016 17th Int. Symp. Antenna Technol. Appl. Electromagn.*, IEEE, Jul. 2016, pp. 1–2.

[66] ——, "Spaceborne GNSS-R sea ice detection using delay-Doppler maps: First results from the U.K. TechDemoSat-1 mission," *IEEE J. Sel. Top. Appl. Earth Obs. Remote Sens.*, vol. 9, no. 10, pp. 4795–4801, Oct. 2016.

[67] Q. Yan, W. Huang, and C. Moloney, "Neural networks based sea ice detection and concentration retrieval from GNSS-R delay-Doppler maps," *IEEE J. Sel. Top. Appl. Earth Obs. Remote Sens.*, vol. 10, no. 8, pp. 3789–3798, Aug. 2017.

[68] Q. Yan and W. Huang, "Sea Ice Sensing From GNSS-R Data Using Convolutional Neural Networks," *IEEE Geosci. Remote Sens. Lett.*, vol. 15, no. 10, pp. 1510–1514, Oct. 2018.

[69] ——, "Convolutional Neural Networks-Based Sea Ice Detection From TDS-1 Data," in *2018 18th Int. Symp. Antenna Technol. Appl. Electromagn.*, IEEE, Aug. 2018, pp. 1–2.

[70] ——, "Detecting Sea Ice From TechDemoSat-1 Data Using Support Vector Machines With Feature Selection," *IEEE J. Sel. Top. Appl. Earth Obs. Remote Sens.*, vol. 12, no. 5, pp. 1409–1416, May 2019.

[71] ——, "Sea Ice Concentration Estimation From TechDemoSat-1 Data Using Support Vector Regression," in *2019 IEEE Radar Conf.*, Boston, Massachusetts USA: IEEE, 2019, pp. 1–6.

[72] ——, "Sea Ice Thickness Estimation From TechDemoSat-1 Data," in *Ocean. 2019 - Marseille*, Marseille, France: IEEE, Jun. 2019, pp. 1–4.

[73] A. Alonso-Arroyo, V. U. Zavorotny, and A. Camps, "Sea Ice Detection Using U.K. TDS-1 GNSS-R Data," *IEEE Trans. Geosci. Remote Sens.*, vol. 55, no. 9, pp. 4989–5001, Sep. 2017.

[74] J. Cartwright, C. J. Banks, and M. Srokosz, "Sea ice detection using GNSS-R data from TechDemoSat-1," *J. Geophys. Res. Ocean.*, 2019JC015327, Jul. 2019.

[75] G. Zhang, J. Guo, D. Yang, F. Wang, and H. Gao, "Sea Ice Edge Detection Using Spaceborne GNSS-R Signal," *Geomatics Inf. Sci. Wuhan Univ.*, vol. 44, no. 5, pp. 668–674, 2019.

[76] Y. Zhu, K. Yu, J. Zou, and J. Wickert, "Sea Ice Detection Based on Differential Delay-Doppler Maps from UK TechDemoSat-1," *Sensors*, vol. 17, no. 7, p. 1614, Jul. 2017.

[77] D. Schiavulli, F. Frappart, G. Ramillien, J. Darrozes, F. Nunziata, and M. Migliaccio, "Observing Sea/Ice Transition Using Radar Images Generated From TechDemoSat-1 Delay Doppler Maps," *IEEE Geosci. Remote Sens. Lett.*, vol. 14, no. 5, pp. 734–738, May 2017.

[78] Q. Yan and W. Huang, "Sea Ice Detection Based on Unambiguous Retrieval of Scattering Coefficient from GNSS-R Delay-Doppler Maps," in *2018 Ocean. - MTS/IEEE Kobe Techno-Oceans*, IEEE, May 2018, pp. 1–5.

[79] E. Valencia, A. Camps, J. F. Marchan-Hernandez, H. Park, X. Bosch-Lluis, N. Rodriguez-Alvarez, and I. Ramos-Perez, "Ocean Surface's Scattering Coefficient Retrieval by Delay–Doppler Map Inversion," *IEEE Geosci. Remote Sens. Lett.*, vol. 8, no. 4, pp. 750–754, Jul. 2011.

[80] N. Rodriguez-Alvarez, B. Holt, S. Jaruwatanadilok, E. Podest, and K. C. Cavanaugh, "An Arctic sea ice multi-step classification based on GNSS-R data

from the TDS-1 mission," *Remote Sens. Environ.*, vol. 230, p. 111 202, Sep. 2019.

[81] L. Breiman, J. H. Friedman, R. A. Olshen, and C. J. Stone, *Classification And Regression Trees*. Routledge, Oct. 1984.

[82] C. Hu, C. Benson, C. Rizos, and L. Qiao, "Single-Pass Sub-Meter Space-Based GNSS-R Ice Altimetry: Results From TDS-1," *IEEE J. Sel. Top. Appl. Earth Obs. Remote Sens.*, vol. 10, no. 8, pp. 3782–3788, Aug. 2017.

[83] W. Li, E. Cardellach, F. Fabra, A. Rius, S. Ribó, and M. Martín-Neira, "First spaceborne phase altimetry over sea ice using TechDemoSat-1 GNSS-R signals," *Geophys. Res. Lett.*, vol. 44, no. 16, pp. 8369–8376, Aug. 2017.

[84] V. U. Zavorotny and A. G. Voronovich, "Scattering of GPS signals from the ocean with wind remote sensing application," *IEEE Trans. Geosci. Remote Sens.*, vol. 38, no. 2, pp. 951–964, Mar. 2000.

[85] T. Hobiger, J. Strandberg, and R. Haas, "Inverse modeling of ground-based GNSS-r — Results and new possibilities," in *2017 IEEE Int. Geosci. Remote Sens. Symp.*, IEEE, Jul. 2017, pp. 2671–2681.

[86] S. Laxon, "Sea ice altimeter processing scheme at the EODC," *Int. J. Remote Sens.*, vol. 15, no. 4, pp. 915–924, Mar. 1994.

[87] C. Li, W. Huang, and S. Gleason, "Dual Antenna Space-Based GNSS-R Ocean Surface Mapping: Oil Slick and Tropical Cyclone Sensing," *IEEE J. Sel. Top. Appl. Earth Obs. Remote Sens.*, vol. 8, no. 1, pp. 425–435, Jan. 2015.

[88] A. Rius, E. Cardellach, F. Fabra, W. Li, S. Ribó, M. Hernández-Pajares, A. Rius, E. Cardellach, F. Fabra, W. Li, S. Ribó, and M. Hernández-Pajares, "Feasibility of GNSS-R Ice Sheet Altimetry in Greenland Using TDS-1," *Remote Sens.*, vol. 9, no. 7, p. 742, Jul. 2017.

[89] G. I. Belchansky and D. C. Douglas, "Classification Methods for Monitoring Arctic Sea Ice Using OKEAN Passive/Active Two-Channel Microwave Data," *Remote Sens. Environ.*, vol. 73, no. 3, pp. 307–322, Sep. 2000.

[90] V. Kůrková, "Kolmogorov's theorem and multilayer neural networks," *Neural Networks*, vol. 5, no. 3, pp. 501–506, Jan. 1992.

[91] R. Ressel, A. Frost, and S. Lehner, "A Neural Network-Based Classification for Sea Ice Types on X-Band SAR Images," *IEEE J. Sel. Top. Appl. Earth Obs. Remote Sens.*, vol. 8, no. 7, pp. 3672–3680, Jul. 2015.

[92] S. S. Haykin, *Neural networks : a comprehensive foundation*. Prentice Hall, 1999, p. 842.

[93] K. Hornik, M. Stinchcombe, and H. White, "Multilayer feedforward networks are universal approximators," *Neural Networks*, vol. 2, no. 5, pp. 359–366, Jan. 1989.

[94] P. Werbos, "Beyond regression : new tools for prediction and analysis in the behavioral sciences," PhD thesis, Harvard University, 1974.

[95] D. W. Marquardt, "An algorithm for least-squares estimation of nonlinear parameters," *J. Soc. Ind. Appl. Math.*, vol. 11, no. 2, pp. 431–441, Jun. 1963.

[96] M. Hagan and M. Menhaj, "Training feedforward networks with the Marquardt algorithm," *IEEE Trans. Neural Networks*, vol. 5, no. 6, pp. 989–993, 1994.

[97] X. Shen, J. Zhang, X. Zhang, J. Meng, and C. Ke, "Sea Ice Classification Using Cryosat-2 Altimeter Data by Optimal Classifier–Feature Assembly," *IEEE Geosci. Remote Sens. Lett.*, vol. 14, no. 11, pp. 1948–1952, Nov. 2017.

[98] L. Zhang, L. Zhang, and B. Du, "Deep Learning for Remote Sensing Data: A Technical Tutorial on the State of the Art," *IEEE Geosci. Remote Sens. Mag.*, vol. 4, no. 2, pp. 22–40, Jun. 2016.

[99] X. X. Zhu, D. Tuia, L. Mou, G.-S. Xia, L. Zhang, F. Xu, and F. Fraundorfer, "Deep Learning in Remote Sensing: A Comprehensive Review and List of Resources," *IEEE Geosci. Remote Sens. Mag.*, vol. 5, no. 4, pp. 8–36, Dec. 2017.

[100] Y. A. LeCun, L. Bottou, G. B. Orr, and K.-R. Müller, *Efficient BackProp*. Springer, Berlin, Heidelberg, 2012, pp. 9–48.

[101] C. Cortes and V. Vapnik, "Support-vector networks," *Mach. Learn.*, vol. 20, no. 3, pp. 273–297, Sep. 1995.

[102] J. T. Atkinson, R. Ismail, and M. Robertson, "Mapping Bugweed (Solanum mauritianum) Infestations in Pinus patula Plantations Using Hyperspectral Imagery and Support Vector Machines," *IEEE J. Sel. Top. Appl. Earth Obs. Remote Sens.*, vol. 7, no. 1, pp. 17–28, Jan. 2014.

[103] M. Pal and P. M. Mather, "Support vector machines for classification in remote sensing," *Int. J. Remote Sens.*, vol. 26, no. 5, pp. 1007–1011, Mar. 2005.

[104] H. Liu, H. Guo, and L. Zhang, "SVM-Based Sea Ice Classification Using Textural Features and Concentration From RADARSAT-2 Dual-Pol ScanSAR Data," *IEEE J. Sel. Top. Appl. Earth Obs. Remote Sens.*, vol. 8, no. 4, pp. 1601–1613, Apr. 2015.

[105] S. Leigh, Zhijie Wang, and D. A. Clausi, "Automated Ice–Water Classification Using Dual Polarization SAR Satellite Imagery," *IEEE Trans. Geosci. Remote Sens.*, vol. 52, no. 9, pp. 5529–5539, Sep. 2014.

[106] M. Liu, R. Tang, Z.-L. Li, Y. Yao, and G. Yan, "Global Land Surface Evapotranspiration Estimation From Meteorological and Satellite Data Using the Support Vector Machine and Semiempirical Algorithm," *IEEE J. Sel. Top. Appl. Earth Obs. Remote Sens.*, vol. 11, no. 2, pp. 513–521, Feb. 2018.

[107] L. Liu, W. Huang, and C. Wang, "Hyperspectral Image Classification With Kernel-Based Least-Squares Support Vector Machines in Sum Space," *IEEE J. Sel. Top. Appl. Earth Obs. Remote Sens.*, vol. 11, no. 4, pp. 1144–1157, Apr. 2018.

[108] G. Camps-Valls and L. Bruzzone, "Kernel-based methods for hyperspectral image classification," *IEEE Trans. Geosci. Remote Sens.*, vol. 43, no. 6, pp. 1351–1362, Jun. 2005.

[109] K.-R. Muller, S. Mika, G. Ratsch, K. Tsuda, and B. Scholkopf, "An introduction to kernel-based learning algorithms," *IEEE Trans. Neural Networks*, vol. 12, no. 2, pp. 181–201, Mar. 2001.

[110] J. Shawe-Taylor, P. Bartlett, R. Williamson, and M. Anthony, "Structural risk minimization over data-dependent hierarchies," *IEEE Trans. Inf. Theory*, vol. 44, no. 5, pp. 1926–1940, 1998.

[111] X. Chen, W. Huang, and G. Yao, "Wind Speed Estimation From X-Band Marine Radar Images Using Support Vector Regression Method," *IEEE Geosci. Remote Sens. Lett.*, vol. 15, no. 9, pp. 1312–1316, Sep. 2018.

[112] C. Parkinson, P. Gloersen, H. Zwally, D. Cavalieri, W. Meier, F. Fetterer, K. Knowles, M. Savoie, and M. Brodzik, *Sea Ice Concentrations from Nimbus-7 SMMR and DMSP SSM/I-SSMIS Passive Microwave Data, Version 1*, Boulder, Colorado USA, 1996.

[113] *Data: Terminology — National Snow and Ice Data Center*.

[114] Q. Yan and W. Huang, "A process to simulate GNSS-R delay-Doppler map of tsunami-dominant sea surface," in *Ocean. 2015 - MTS/IEEE Washingt.*, IEEE, Oct. 2015, pp. 1–5.

[115] S. Zippel and J. Thomson, "Air-sea interactions in the marginal ice zone," *Elem. Sci. Anthr.*, vol. 4, no. 0, p. 000 095, Mar. 2016.

[116] N. O. US Department of Commerce and N. D. B. C. Atmospheric Administration National Weather Service, "National Data Buoy Center,"

[117] D. P. Dee, S. M. Uppala, A. J. Simmons, P. Berrisford, P. Poli, S. Kobayashi, U. Andrae, M. A. Balmaseda, G. Balsamo, P. Bauer, P. Bechtold, A. C. M. Beljaars, L. van de Berg, J. Bidlot, N. Bormann, C. Delsol, R. Dragani, M. Fuentes, A. J. Geer, L. Haimberger, S. B. Healy, H. Hersbach, E. V. Hólm, L.

Isaksen, P. Kållberg, M. Köhler, M. Matricardi, A. P. McNally, B. M. Monge-Sanz, J.-J. Morcrette, B.-K. Park, C. Peubey, P. de Rosnay, C. Tavolato, J.-N. Thépaut, and F. Vitart, "The ERA-Interim reanalysis: configuration and performance of the data assimilation system," *Q. J. R. Meteorol. Soc.*, vol. 137, no. 656, pp. 553–597, 2011.

[118] K. A. Giles, S. W. Laxon, and A. L. Ridout, "Circumpolar thinning of Arctic sea ice following the 2007 record ice extent minimum," *Geophys. Res. Lett.*, vol. 35, no. 22, p. L22502, Nov. 2008.

[119] X. Tian-Kunze, L. Kaleschke, and N. Maass, *SMOS Daily sea ice thickness version 3*, 2016.

[120] M. Huntemann, G. Heygster, L. Kaleschke, T. Krumpen, M. Mäkynen, and M. Drusch, "Empirical sea ice thickness retrieval during the freeze-up period from SMOS high incident angle observations," *Cryosph.*, vol. 8, no. 2, pp. 439–451, Mar. 2014.

[121] D. Mayers and C. Ruf, "Measuring Ice Thickness with Cygnss Altimetry," in *IGARSS 2018 - 2018 IEEE Int. Geosci. Remote Sens. Symp.*, IEEE, Jul. 2018, pp. 8535–8538.

[122] H. Carreno-Luengo, G. Luzi, and M. Crosetto, "Sensitivity of CyGNSS bistatic reflectivity and SMAP microwave radiometry brightness temperature to geophysical parameters over land surfaces," *IEEE J. Sel. Top. Appl. Earth Obs. Remote Sens.*, vol. 12, no. 1, pp. 107–122, Jan. 2019.

[123] ——, "Impact of the elevation angle on CYGNSS GNSS-R bistatic reflectivity as a function of effective surface roughness over land surfaces," *Remote Sens.*, vol. 10, no. 11, p. 1749, Nov. 2018.

[124] G. A. Hajj and C. Zuffada, "Theoretical description of a bistatic system for ocean altimetry using the GPS signal," *Radio Sci.*, vol. 38, no. 5, n/a–n/a, Oct. 2003.

[125] P. Jales and M. Unwin, "Mission Description GNSS Reflectometry on TDS-1 with the SGR-ReSI," Surrey Satellite Technology Limited, Surrey, UK, Tech. Rep., 2015.

[126] L. Tsang and R. W. Newton, "Microwave emissions from soils with rough surfaces," *J. Geophys. Res.*, vol. 87, no. C11, p. 9017, Oct. 1982.

[127] F. T. Ulaby, R. K. Moore, and A. K. Fung, *Microwave remote sensing : active and passive*. Addison-Wesley Pub. Co., Advanced Book Program/World Science Division, 1982, vol. 1, p. 2162.

[128] R. M. Morey, "Airborne Sea Ice Thickness Profiling Using an Impulse Radar," Department of Transportation, United States Coastal Guard, Tech. Rep., 1975.

[129] D. K. Atwood, G. E. Gunn, C. Roussi, J. Wu, C. Duguay, and K. Sarabandi, "Microwave Backscatter From Arctic Lake Ice and Polarimetric Implications," *IEEE Trans. Geosci. Remote Sens.*, vol. 53, no. 11, pp. 5972–5982, Nov. 2015.

[130] M. R. Vant, R. O. Ramseier, and V. Makios, "The complex-dielectric constant of sea ice at frequencies in the range 0.1–40 GHz," *J. Appl. Phys.*, vol. 49, no. 3, pp. 1264–1280, Mar. 1978.

[131] F. T. Ulaby, R. K. Moore, and A. K. Fung, *Microwave remote sensing : active and passive*. Addison-Wesley Pub. Co., Advanced Book Program/World Science Division, 1986, vol. 2, p. 2162.

[132] W. L. Stutzman, *Polarization in electromagnetic systems*. Artech House, London,UK, 1993.

[133] L. Klein and C. Swift, "An improved model for the dielectric constant of sea water at microwave frequencies," *IEEE Trans. Antennas Propag.*, vol. 25, no. 1, pp. 104–111, Jan. 1977.

[134] J. Cartwright, M. P. Clarizia, P. Cipollini, C. Banks, and M. Srokosz, "Independent DEM of Antarctica using GNSS-R data from TechDemoSat-1," *Geophys. Res. Lett.*, vol. 45, no. 12, pp. 6117–6123, Jun. 2018.

[135] Q. Yan and W. Huang, "Sea ice thickness measurement using spaceborne GNSS-R: First results with TechDemoSat-1 data," *IEEE J. Sel. Top. Appl. Earth Obs. Remote Sens.*, vol. 13, pp. 577–587, 2020.

[136] P. Jales, "MERRByS Product Manual - GNSS Reflectometry on TDS-1 with the SGR-ReSI," Tech. Rep., 2017.

[137] A. G. Voronovich and V. U. Zavorotny, "Bistatic Radar Equation for Signals of Opportunity Revisited," *IEEE Trans. Geosci. Remote Sens.*, vol. 56, no. 4, pp. 1959–1968, Apr. 2018.

[138] R. G. Onstott, T. C. Grenfell, C. Matzler, C. A. Luther, and E. A. Svendsen, "Evolution of microwave sea ice signatures during early summer and midsummer in the marginal ice zone," *J. Geophys. Res.*, vol. 92, no. C7, p. 6825, Jun. 1987.